# Characterization of pi-Conjugated Polymers for Transistor and Photovoltaic Applications

A DISSERTATION
SUBMITTED TO THE FACULTY OF THE GRADUATE SCHOOL
OF THE UNIVERSITY OF MINNESOTA
BY

Bryan D. Paulsen

IN PARTIAL FULFILLMENT OF THE REQUIREMENTS
FOR THE DEGREE OF
DOCTOR OF PHILOSOPHY

C. Daniel Frisbie, Advisor

December 2012

**Acknowledgements**

I would like to expressly thank my advisor, Prof. C. Daniel Frisbie. His guidance, support, and scrutiny have been enormously helpful these past years in my development, both inside and outside the laboratory. Additionally, I would be remiss not to thank Profs. Russell J. Holmes, Marc A. Hillmyer, and William H. Smyrl for their crucial insights. Many thanks to Prof. Matthew J. Panzer and Dr. Derek M. Stevens for ushering me into the world of electrochemically gated transistors and polymer photovoltaics, respectively. I owe a debt of gratitude to the exceptional classroom instruction of Profs. P. Paul Ruden, Chris Leighton, and Alex Kamenev. I am much obliged to my collaborators, coworkers, and coauthors especially Josh C. Speros, Dr. Yu Xia, Dr. Loren G. Kaake, Scott P. White, Megan Claflin, Prof. JeongHo Cho, Yanfei Wu, Elizabeth A. Jackson, Dr. Danielle Braga, Prof. Moon Sung Kang, Dr. Jiyoul Lee, Dr. Shun Wang, Wei Xie, Dr. Keun Hyung Lee, Dr. Richa Pandey, Dr. Sipei Zhang, Dr. Mingjing Ha, Dr. David Ellison, Johannes Schock, and Dr. Yan Liang. I am also grateful to my undergraduate advisor Prof. A. Allen Hersel, without his guidance I would not have pursued graduate studies. Many thanks to Prof. Frank W. Snowden, Phillip Engen, and Sharon Emde from the MRSEC. My infinite gratitude to Julie Prince, Teresa Bredahl, and Mary Nissen, with out whom the Department of Chemical Engineering and Materials Science could not function. Finally, thanks and all credit to my parents and stepparents Kevin Paulsen, Debra Supinski, Debbie Paulsen, and Leo Supiniski, and to my grandmother Esther Paulsen.

**Abstract**

π-Conjugated polymers represent a unique class of optoelectronic materials. Being polymers, they are solution processable and inherently "soft" materials. This makes them attractive candidates for the production of roll-to-roll printed electronic devices on flexible substrates. The optical and electronic properties of π-conjugated polymers are synthetically tunable allowing material sets to be tailored to specific applications. Two of the most heavily researched applications are the thin film transistor, the building block of electronic circuits, and the bulk heterojunction solar cell, which holds great potential as a renewable energy source. Key to developing commercially feasible π-conjugated polymer devices is a thorough understanding of the electronic structure and charge transport behavior of these materials in relationship with polymer structure. Here this structure property relationship has been investigated through electrical and electrochemical means in concert with a variety of other characterization techniques and device test beds. The tunability of polymer optical band gap and frontier molecular orbital energy level was investigated in systems of vinyl incorporating statistical copolymers. Energy levels and band gaps are crucial parameters in developing efficient photovoltaic devices, with control of these parameters being highly desirable. Additionally, charge transport and density of electronic states were investigated in π-conjugated polymers at extremely high electrochemically induced charge density. Finally, the effects of molecular weight on π-conjugated polymer optical properties, energy levels, charge transport, morphology, and photovoltaic device performance was examined.

**Table of Contents**

## *List of Tables*

## *List of Figures*

# *1. Introduction*

With research of π-conjugated polymers now carrying on through a fourth decade, what was once the interest of a handful of researchers had become an established field of scientific research.[1] Due to their unique optical and electronic properties, π-conjugated polymers have been applied to a wide variety of applications that were previously the domain of inorganic semiconductors, such as silicon or germanium. While it is implausible that polymeric materials can replace silicon in high-density integrated circuits for computing applications, the unique properties of π-conjugated polymers open new applications not available to traditional inorganic semiconductors.

By their very nature, π-conjugated polymers are "soft" materials that are permeable, mechanically flexible, and solution processable. Thus they are seen a prime candidates for inexpensive, roll-to-roll printed, flexible optoelectronic devices.[2] Two devices that are of key interest are the transistor (electrical switch) and the photovoltaic cell. Despite the years of research, significant work remains to be done before π-conjugated polymer transistors and solar cells become a commercial technology. In the case of transistors based on polymeric materials, especially those to be incorporated into exotic flexible applications, there is a need for low voltage (~1 V) and high current operation. To accomplish this, a transistor device must be able to massively modulate the charge carrier density, and those charge carriers must be exceptionally mobile. One appealing avenue to accomplish this is the electrolyte gated polymer thin film transistor, which has recently been adapted to printing based fabrication techniques.[3] These electrolyte gated printed π-

conjugated transistors have been demonstrated in a variety of circuits including ring oscillators, logic circuits, delays, memory circuits, electrochromic displays, and light emitting diode drivers.[4,5,6] While electrolyte gating has produced a wide variety of low voltage printed circuits, the outer limits of device operation remain to be investigated, with studies at very high charge density and potential being especially pertinent.

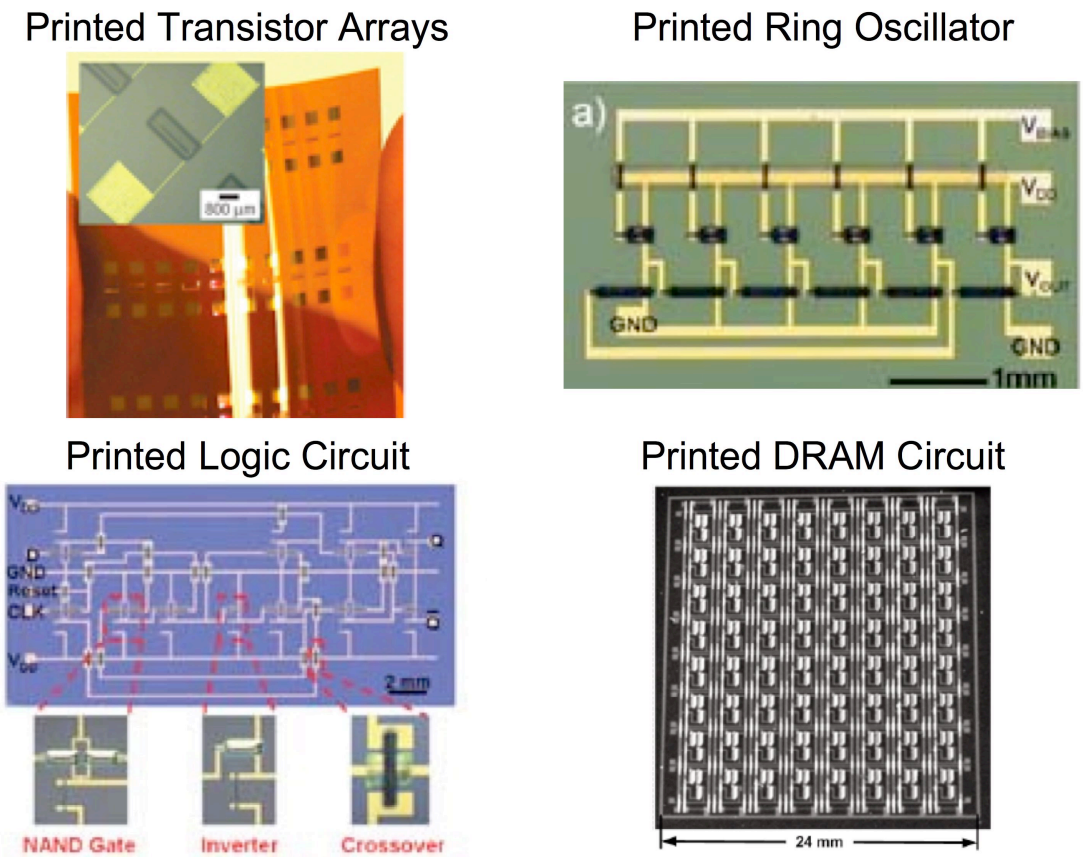


**Figure 1.1** Examples of electrolyte gated π-conjugated polymer printed circuits developed in the Frisbie research group at the University of Minnesota.

In the case of photovoltaic devices, due to the increasing demand for cheap renewable energy sources, much attention has been given to solar energy conversion devices incorporating π-conjugated polymers. This research attention has driven the

development of the bulk heterojunction thin film solar cells, employing π-conjugated polymers as light absorbing electron-donating materials in a blended heterojunction with soluble electron-accepting fullerene derivatives. These devices have undergone rapid advances in recent years with current power conversion efficiencies reported in peer reviewed scientific journals reaching 8.6%, and independently certified laboratory results reaching 10.6%.[7,8,9]

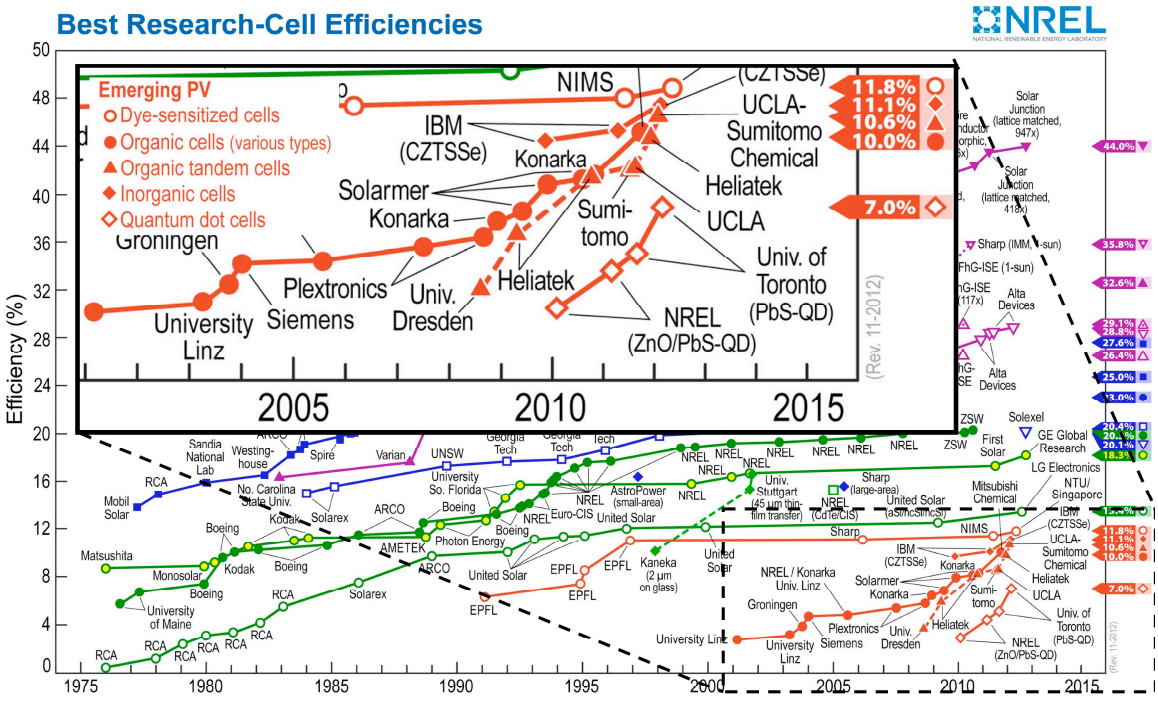


**Figure 1.2** Plot of best certified research photovoltaic cell efficiencies over time. The inset displays the progress of organic (including polymer-based) cells over the past decade. The π-conjugated polymer incorporating UCLA-Sumitomo Chemical cell is a current record holder [7].

As is often the case, the performance has outpaced the fundamental scientific understanding. For instance, work remains to thoroughly establish the role of polymer synthetic design and molecular weight on optoelectronic properties and device

performance. Additionally, their current voltage behavior and fundamental charge transport remain active areas of research, with a comprehensive model of π-conjugated bulk heterojunction devices remaining elusive.[10,11] However, these "gaps" in the field hold great promise, as thorough investigation will very likely drive further improvement in device performance, pushing π-conjugated polymer based bulk heterojunction solar cells ever closer to being a viable alternative to current energy production, and one of the many pieces necessary to solve the puzzle of sustainable global energy production.

## *1.1 Thesis Overview*

This thesis focuses on π-conjugated polymers in transistor and photovoltaic applications, with the unifying thread being the application of electrochemical methods to investigate polymer electronic structure and charge transport. Additionally a variety of techniques and experimental device test beds were brought to bear in the process, with the goal being the improved understanding of charge transport and electronic structure. This was specifically carried out in the systematic investigation of energy level tuning in vinyl containing polymers, the study of charge carrier mobility and electronic density of states in a variety of polymers at very high electrochemically induced charge density, and the exhaustive examination of poly(thienylene vinylene) molecular weight effects on polymer structure, optical properties, energy level position, charge transport, solar cell device performance, and bulk heterojunction morphology.

The following chapter puts forward a synopsis of π-conjugated polymers, covering their chemical and electronic structure. Additionally, methods by which to induce mobile

charge carriers in conjugated polymers are discussed, and manner in which those charge carriers are transported in described.

Chapter 3 provides an overview of π-conjugated polymer devices pertinent to this thesis. These include field effect transistors, electrochemical transistors, and photovoltaic devices. The basic device structure and operating principles are presented, device models are discussed, and key parameters are identified.

Chapter 4 presents the experimental methods used in the work covered in this thesis. The evaporative and solution-based deposition techniques used to fabricate thin film transistor and photovoltaic device structures are presented. The equipment and procedures used to electrically characterize transistor and photovoltaic devices are discussed. The potential sweep methods used to collect cyclic voltammograms, with an *in situ* measure of conductivity, are laid out. Finally, ancillary characterization techniques such as optical absorption spectroscopy, differential scanning calorimetry, and profilometry are summarized.

Chapter 5 is adapted from the previously published work "Band Gap and HOMO Level Control in Poly(thienylene vinylene)s Prepared by ADMET Polymerization" Joshua C. Speros, Bryan D. Paulsen, Bradley S. Slowinski, C. Daniel Frisbie, and Marc A. Hillmyer, *ACS Macro Lett., 2012, 1, pp 986–990*. This work, carried out in conjunction with Joshua Speros, established the ability to tune the molecular orbital levels and optical band gap of conjugated statistical copolymers through control of the ratio of incorporated monomers with distinct chemical and electronic structure. Optical and electrochemical techniques were employed to evaluate energy level positions of three

series of conjugated copolymers, revealing depth of copolymer HOMO levels, and the magnitude of the band gaps, were tuned over a range of 460 and 200 meV, respectively. These are critical properties for polymers incorporated in photovoltaic devices, and control of these properties is key in maximizing photovoltaic performance. In addition here, the work was expanded to include the study of a family of statistical copolymers with more idealized donor-acceptor character. This expanded the range of tunability of HOMO level position and band gap, and increased the breadth of polymer light absorption.

Chapter 6 is adapted from the previously published work "Dependence of Conductivity on Charge Density and Electrochemical Potential in Polymer Semiconductors Gated with Ionic Liquids" Bryan D. Paulsen and C. Daniel Frisbie, *J. Phys. Chem. C, 2012, 116 (4), pp 3132–3141*. Here, by taking advantage of the large electrochemical window of room temperature ionic liquids, the position and distribution of the HOMO states of ionic liquid doped poly(3-hexylthiophene) were determined via cyclic voltammetry carried out to extreme oxidative potentials. Additionally, at such high levels of oxidation the induced charge density and electrical conductivity were investigated revealing a potential and charge density dependent finite window of high conductivity. Variable temperature measurements were employed to understand the nature of electronic charge transport, and a series of different ionic liquids and conjugated polymers where investigated, establishing the generality of the results.

Chapter 7 is adapted from the previously published work "An ADMET Route to Low-Band-Gap Poly(3-hexadecylthienylene vinylene): A Systematic Study of Molecular

Weight on Photovoltaic Performance" Joshua C. Speros, Bryan D. Paulsen, Scott P. White, Yanfei Wu, Elizabeth A. Jackson, Bradley S. Slowinski, C. Daniel Frisbie, and Marc A. Hillmyer, *Macromolecules, 2012, 45 (5), pp 2190–2199*. This work, also carried out in conjunction with Joshua Speros, investigated the effects of molecular weight dependence on the properties of poly(3-hexadecylthienylene vinylene). A series of neat polymers, with increasing molecular, was characterized using a variety of optical, electrochemical, and thermal techniques. The series was incorporated into transistor and photovoltaic devices, revealing that increased molecular weight improved charge transport and photovoltaic efficiency. Finally, the morphology and phase behavior of the photovoltaic active layer blends was investigated and mapped out.

Finally, Chapter 8 proposed further research opportunities stemming from this thesis work. Specifically in the case of electrolyte gated devices this includes investigation of the field dependence of charge transport in electrolyte gated P3HT at very high charge carrier density. A natural extension of Chapter 5 is the expansion of the investigations of optoelectronic property tunablity of vinyl containing copolymers to include photovoltaic device studies, and new copolymer series. Also focusing on photovoltaic devices, are proposed studies of vinyl dilution and alkyl chain structure in poly(thienylene vinylene)s, temperature dependent charge transport in bulk heterojunctions, and improved data sets through experimental design driven by numerical methods.

# *2. π-Conjugated Polymers*

π-Conjugated polymers are macromolecular chains of covalently linked repeating sub units (monomers) that display periodically fluctuating electron density, most commonly due to an extended pattern of alternating single and double bonds. There has been a deep sustained interest in conjugated polymers due to their unique optoelectronic properties. While maintaining many of the characteristics of traditional polymers, especially solution processability and synthetic tunability, conjugated polymers display semiconducting properties that make them applicable to a wide range of electronic devices. π-Conjugated polymers were first observed to exhibit significant electrical conductivity in the mid 1960's,[12] and independently observed and brought to the attention of the broader scientific community in the late 1970's.[13] Due to their unique chemical and electronic structure, the optical and electronic behavior of conjugated polymers is still today an area of active study.

## *2.1 Chemical Structure*

The key feature to π-conjugated polymers is the alternation of single and double covalent carbon-carbon bonds extending down the polymer backbone. Carbon readily makes four distinct $sp^3$ hybridized sigma bonds to four other atoms. Alternatively, $sp^2$ carbon can also make two sigma bonds with two atoms, and with a third both a sigma and a pi bond, termed a double bond. The pi bond is relatively weak and pi electrons are loosely bound in comparison to the strongly localized nature of the sigma bond electrons. In π-conjugated systems of alternating single-double bonding, the pi electron wave

functions overlap and the electrons become delocalized. This is readily seen in the model system of cyclohexane and its conjugated cousin benzene. All the elemental valence electrons in cyclohexane are engaged in C-C or C-H localized sigma bonds. However, in benzene, due to its conjugation, there exist C-C pi bonds, whose electron clouds extend above and below the plane of the ring. These orbitals overlap and combine to create a delocalized electron density above and below the plane of the molecule, Figure 2.1.

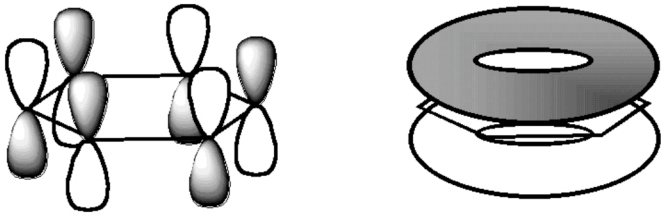

**Figure 2.1** Schematic of the pi orbitals in benzene and their overlap and delocalization into electron clouds.

This same effect can occur down the length of a conjugated polymer backbone. Common conjugated polymers incorporate vinyl or aromatic repeat units along the polymer backbone. Historically, research focused on repeat units incorporating vinyl, phenyl vinyl, thiophene, analine and pyrrole moieties, Firgure 2.2. However, due to synthetic flexibility of conjugated polymers, the variety and complexity of polymer repeat units studied has grown rapidly. Aside from the backbone structure, most conjugated polymers studied today contain alkyl side chains which improve polymer solubility and processing, with the benchmark conjugated polymer, poly(3-hexylthiophene) (P3HT), being a prime example. In this thesis polymers containing thiophene, vinyl, benzothiadiazole, fluorene, and carbazole constituents where studied, Figure 2.3.

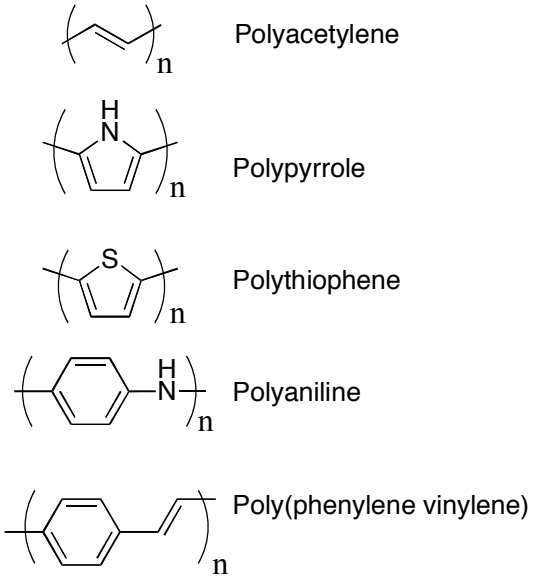


**Figure 2.2** Historically important families of conjugated polymers initially studied.

In polymeric materials, conjugation severely reduces the freedom of chain motion, as pi bonds do not have the available bond rotation inherent in sigma bonds. Thus, conjugated polymers display rod-like behavior, as opposed to random coils, which is a fundamental assumption in most polymer thermodynamic models. While the rigid nature of the polymer backbone can lead to reduced solubility, it also enhances polymer aggregation and ordering which can amplify the effects that conjugation has on the polymer's optoelectronic properties.[14,15]

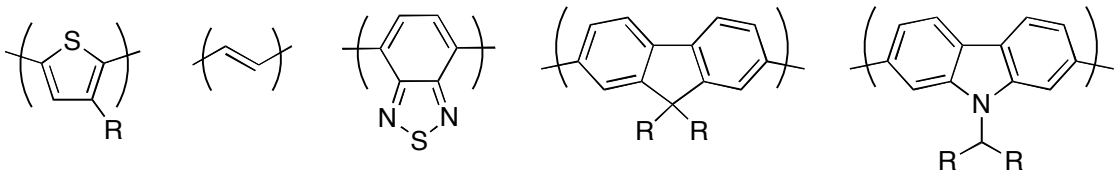

**Figure 2.3** Thiophene, vinyl, benzothiadiazole, fluorene, and carbazole constituents incorporated in the polymers pertinent to this thesis.

## *2.2 Electronic Structure*

In concert with the structural effects, conjugation in polymer systems leads to unique electronic structure. To discuss the electronic structure of conjugated polymers it is necessary to use the model of molecular orbitals. A valence electron in a molecule, when unexcited, lies in the highest occupied molecular orbital, HOMO. If excited, the valence electron can be promoted to the lowest unoccupied molecular orbital, LUMO.

### *2.2.1 Molecular Orbitals and Simplified Band Structure and Density of States*

According to the theory of linear combination of molecular orbitals, when two half filled orbitals are combined to create a bond between atoms, the identical discrete energy levels split into two shared levels, the bonding and anti-bonding states. Each of these states can accommodate two electrons, and thus the bond decreases the overall energy by placing the two donated electrons in the lower energy bonding state and leaving the energetically unfavorable anti-bonding state empty. Extrapolating out to N atoms in a linear chain each contributing a single electron to create a bond with each of its two nearest neighbors, would create 2N states, with the lowest N states containing the 2N shared electrons, Figure 2.4. The energy level splitting that occurs with bond formation is limited to a finite range so in the case of an infinite string of bonded atoms the discrete states would form a continuum of allowed energies within a finite band. Thus in an infinite chain the HOMO and LUMO states will broaden into HOMO and LUMO bands.[16] The number of states per increment of energy is referred to as the density of states (DOS), with DOS describing the "shape" of HOMO and LUMO bands.

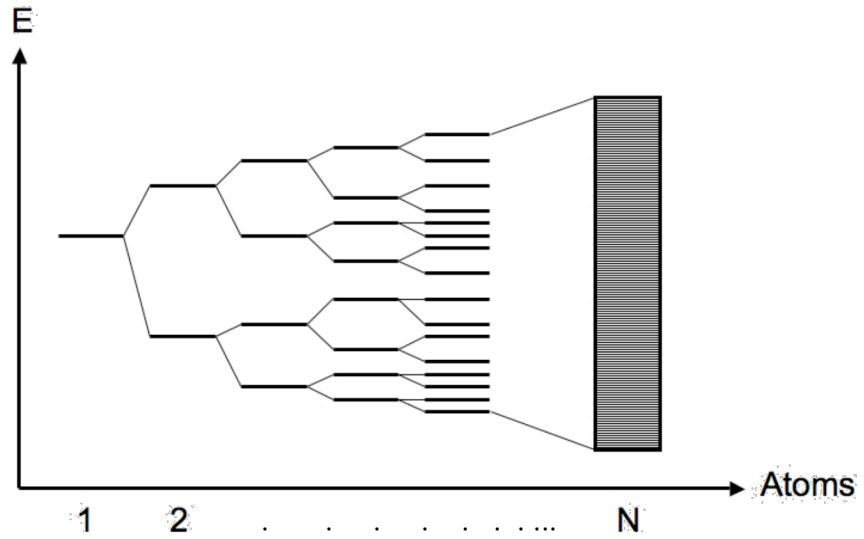


**Figure 2.4** Diagram of molecular orbital splitting as the number of atoms in a system increases.

### *2.2.2 Peierls Instability and Band Gap*

In the case of conjugated polymers, the pi bonds are alternating, that is each $sp^2$ carbon atom is contributing one pi electron. Thus it would follow that there would exist a half filled pi HOMO band, rendering the conjugated polymers metallic. However, according to the Peierls instability, a linear metal is unstable and will undergo a deformation in lattice to allow a relaxation in the electronic energy levels and creation of a new band gap in the middle of the pi HOMO band, Figure 2.5. This creates a completely full HOMO band and an empty LUMO band, rendering the material a insulator or semiconductor.[17] Polyacetylene displays this type of behavior.

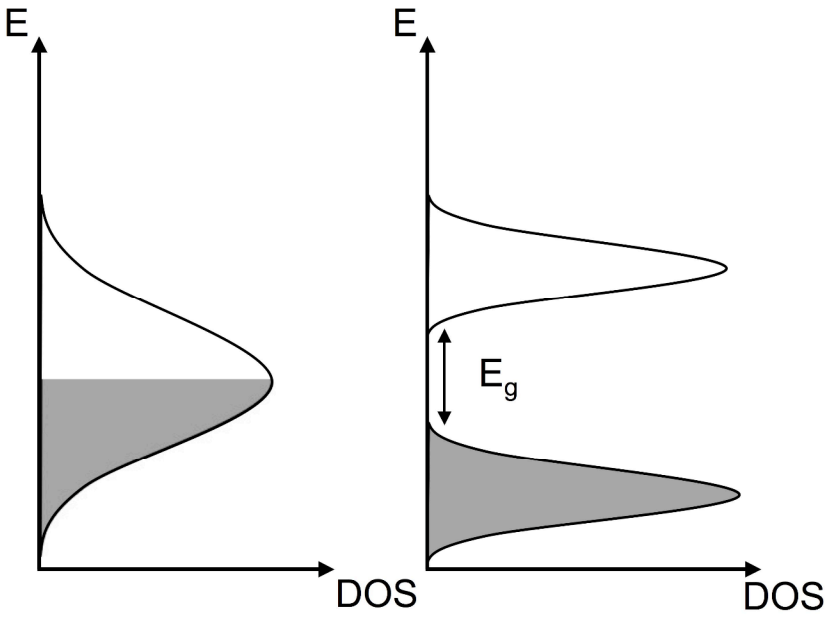


**Figure 2.5** Effect of the Peierls instability on the density of states of a conjugated polymer: splitting of a half filled band and creation of a band gap.

Considering the structure polyacetylene structure, Figure 2.6, if each pi electron is completely delocalized and the carbon atoms are equally spaced, each carbon atom is able to donate a single pi electron to the HOMO band. This should result in polyacetylene having a half filled band of delocalized pi electrons, and thus metallic. Instead polyacetylene undergoes a deformation, creating alternating electron density between the carbon atoms (alternating single/double bonds), and as a result alternating bond lengths. The pi electrons will counteract the energy penalty due to the lattice deformation by lowering their energy, and opening a energy gap.[18] The resulting energy gap in polyacetylene is 1.4 eV,[19] thus classifying it as a semiconductor and not a metal. This holds true for more complicated chain structures, with no pristine undoped conjugated polymers displaying true metallic properties, but all are instead semiconductors.

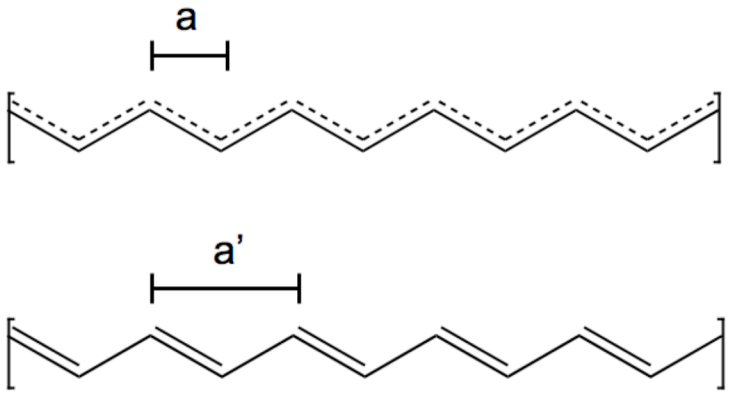


**Figure 2.6** Effect of the Peierls instability on the electron density of polyacetylene.

The other key reason to approach polymer semiconductors using molecular orbital theory is interchain interactions. In a macroscopic polymer material, molecular orbital interactions exist not only along the chains, but on larger scales the interchain interactions become the limiting factor. Thus the proximity, or overlap, of the molecular orbitals of adjacent chains defines much of the bulk properties, such as conductivity and mobility, which have yet to be discussed.

## *2.3 Charge Carrier Generation and Transport*

The ability of a material to transport electrical charge, termed conductivity, is dependent on two key factors: the number of free mobile charge carriers (charge density), and relative ease with which each individual charge carrier can move (carrier mobility). In pristine undoped conjugated polymers the measurable charge density is on the order of $10^{14}$-$10^{17}$ holes $cm^{-3}$, though the majority of charges are trapped due to defects and cannot contribute to the mobile carrier density.[20,21,22,23] Additionally the mobility of these intrinsic carriers is relatively low, $<10^{-1}$ $cm^2$ $V^{-1}$ $s^{-1}$,[24] especially compared to traditional inorganic semiconducting materials, $>10^2$ $cm^2$ $V^{-1}$ $s^{-1}$.[25]

Realization of high performance in optoelectronic applications generally requires a significant charge carrier flux, and thus necessitates an increased mobile charge carrier density, which can occurs in two basic regimes.

First, it can occur by the excitation or injection of electrons to, and transport through, unoccupied molecular orbitals. This type of negative charge carrier transport is referred to as N-type behavior. Conversely, the removal of an electron from, and subsequent motion of its vacancy through occupied molecular orbitals is referred to as P-type behavior, with the charge carrying vacancy termed a "hole". The vast majority of π-conjugated polymers are preferentially P-type materials. Under the correct conditions some π-conjugated can display N-type behavior. When both N and P type behavior (electron and hole motion) are observed, the behavior is referred to as ambipolar.

### *2.3.1 Field Effect: Polarons*

One common and powerful technique by which to induce charge carriers is the field effect. In the field effect, the conjugated polymer is capacitively coupled to a metal electrode in a metal-insulator-polymer structure. The application of electric potential to the metal electrode induces a charge accumulation at the metal-insulator interface, which polarizes the insulating dielectric, thus inducing and stabilizing a two dimensional sheet of oppositely charged carriers at the conjugated polymer-insulator interface, Figure 2.7. Thus, negative polarization of metal electrode induces positively charged holes in the conjugated polymer, and a positive polarization induces negatively charge electrons.

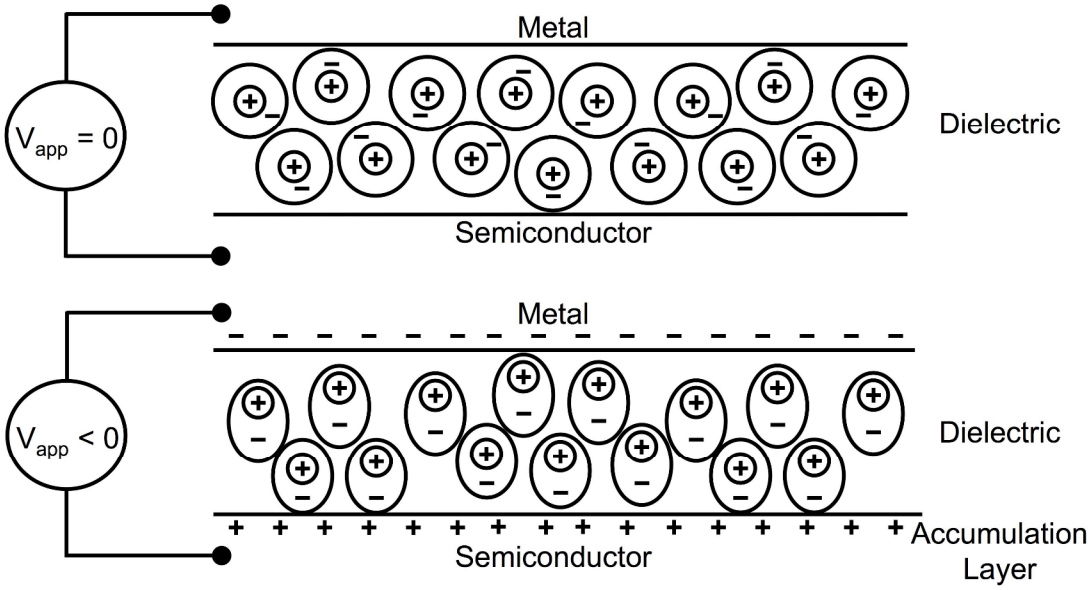


**Figure 2.7** Field effect induced charge carriers in a semiconducting material.

The magnitude of the obtainable two-dimensional charge density is limited by the electric field driven dielectric breakdown of the insulating layer. With common insulating materials this leads to a limit of $10^{13}$ $cm^{-2}$, which can be increased to nearly $10^{14}$ $cm^{-2}$ with the use of high k dielectrics. However, in practice readily accessible charge densities are of the order $10^{12}$ $cm^{-2}$. It is commonly assumed that the accumulation of charge in the conjugated polymers exist in a 1 nm thick layer, thus the equivalent three dimensional charge densities typically achievable in field effect structures is of order $10^{20}$ $cm^{-3}$.

At these charge densities, the charge carriers can be treated as non-interacting. However, the presence of the charge carrier itself induces a structural deformation in the conjugated polymer. In polythiophene based polymers the presence of a positive charge on the polymer induces a local change from the benzoid structure, energetically favored

in neutral state, to the quinoid structure, Figure 2.8. Since the motion of the hole or electron requires a reorganization of the induced structural deformation, it is convenient to treat both the charge carrier and its accompanying deformation as a single quasi-particle, termed a polaron.[26] Thus the polaron is a mobile, singly charged deformation with a finite spin.

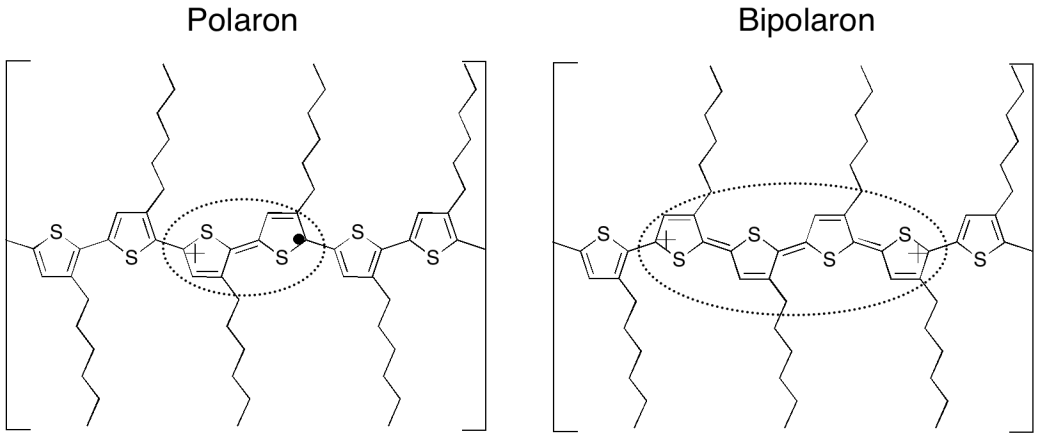


**Figure 2.8** Disruption of the benzoidal structure and quinoidal reorganization due to the presence of a singly charged polaron and doubly charged bipolaron on the backbone of P3HT.

### *2.3.2 Electrochemical Doping: Polarons and Bipolarons*

In order to attain higher charge densities it is necessary to introduce dopants into the conjugated polymer. This can be accomplished by exposing the conjugated polymers to elements or molecules that have small ionization potentials. When incorporated, these dopants ionize and stabilize an oppositely charged carrier on the conjugated polymer backbone, creating a microscopically localized analogue of the field effect. Molecular doping was the first method used to realize conductivity in conjugated polymers.[13] The power of this technique is that the charge density is only limited by the solubility of the dopant in the conjugated polymer.

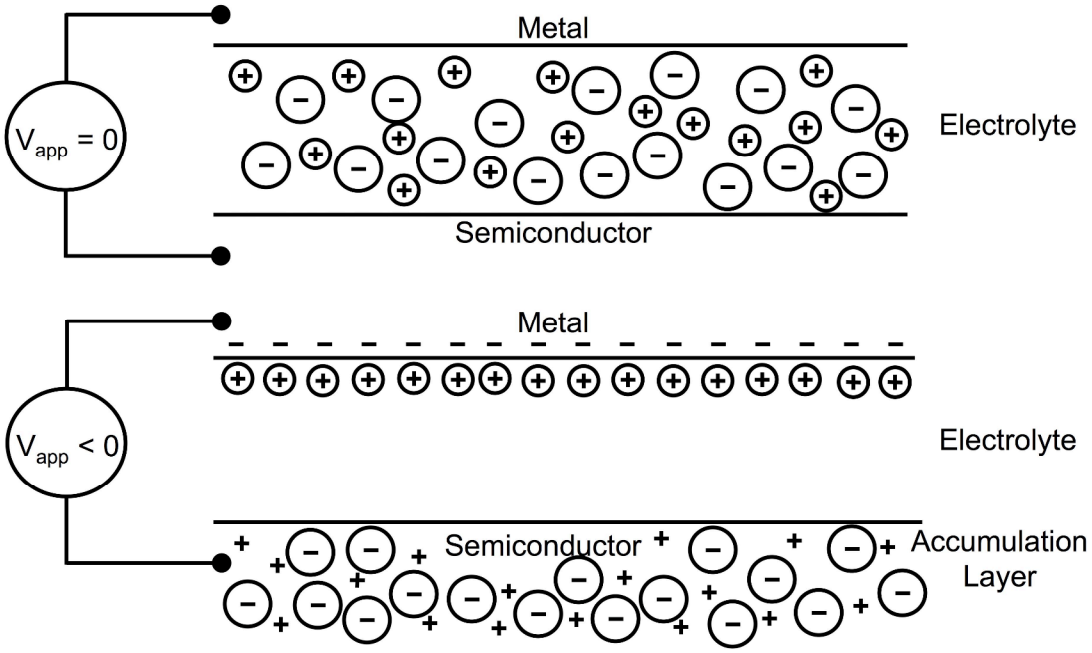


**Figure 2.9** Electrochemically induced charge carriers in a semiconducting material.

Pertinent to this thesis is the process of introducing dopants through electrochemical means.[27] In the case of electrochemical doping, dopant ions are driven into the conjugated polymer from an electrolyte via an electrochemical potential, Figure 2.9. These electrochemical dopant ions stabilize charge carriers in an identical manner to ionized molecular dopants. In addition to the limit of dopant solubility on charge density, electrochemical doping is limited by the potential driven irreversible reaction of the electrolyte and/or conjugated polymer, termed electrolyte breakdown.

Regardless of these limits, electrochemical and molecular doping allow extremely high charge carrier densities of over $10^{21}$ $cm^{-3}$, approaching one hole, or electron, per repeat unit of the conjugated polymer. Despite the Coulombic repulsion due to the carriers same sign, at high carrier concentrations it becomes energetically favorable for the carriers to approach each other and share a single polymer structural deformation.

This creates a doubly charged quasi particle of two charge carriers and one deformation existing at a single energy state, termed a bipolaron.[26] Due to the Pauli exclusion principle, the two carriers must have opposite spin, thus the bipolaron has a net spin of zero.

### *2.3.3 Photogeneration: Excitons and Charge Dissociation*

When light is incident upon a semiconductor, photons with energies equal to or higher than the band gap can excite valence electrons out of their ground state and into unoccupied conducting states. The same holds true for conjugated polymers, but with an important caveat. In conjugated polymers, the excited electron and the newly created positively charged hole are not adequately screened due to the polymers low dielectric constant. In fact the electrostatic attractive force between the electron and hole result in a Coulombic binding energy of ~0.3 eV in polymer systems.[28,29,30] This bound electron hole pair is termed an exciton, Figure 2.10a. Like the previously discussed polaron and bipolaron, in conjugated polymers the exciton also includes a structural reorganization of the conjugated polymer, sometimes referred to as a polaron-exciton.[20] In traditional inorganic semiconducting materials the binding is of the order of a 10 meV, lower than the thermal energy at room temprature, and thus the electron and hole are screened from each other and can move as free carriers.

Under a given illumination, the population of excitons in conjugated polymers is dependent on the ability of the conjugated polymer to absorb light, creating excitons, and the lifetime of the excitons themselves. Given time, the exciton will eventually recombine, with the electron returning to the energy level from which it was promoted, annihilating the hole residing there. This process can occur through a variety of routes.

For instance, the electron can return to its ground state from the initial singlet excited state radiatively, through the process of fluorescence, or non-radiatively, releasing the exciton's energy as heat. Both these emissive (fluorescence) and thermal decay processes occur rapidly, on the order of 0.1 ns and 0.1 ps respectively.[31] These processes can occur so rapidly because both the ground state and the excited state exist as similar singlet spin states. However, prior to recombination from the initial singlet excited state, a change in the spin state, or inter system crossing, can occur, converting from the singlet spin state to a triplet spin state, Figure 2.10b. Transitions from dissimilar spin states are unfavorable, such as the process of recombination from triplet state to a singlet ground state, thus excitons converted to the triplet state have much longer lifetimes of the order of microseconds.[32]

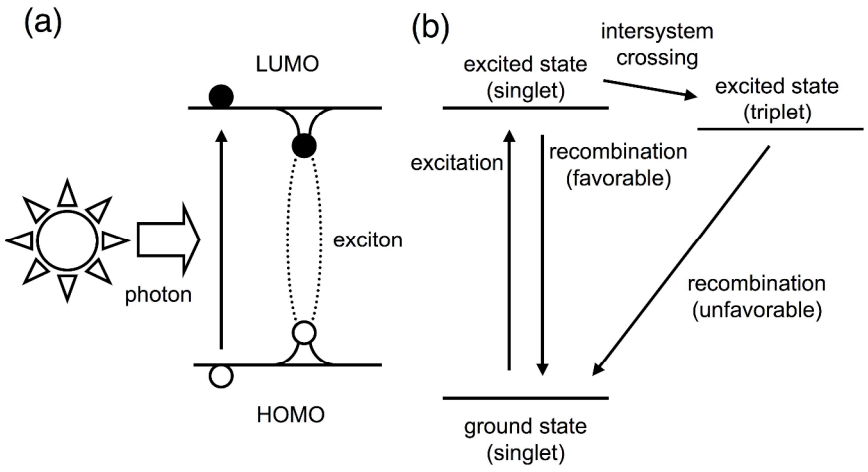


**Figure 2.10** Schematic diagram of (a) light absorption exciting an electron from the HOMO to the LUMO and subsequent relaxation into a bound exciton, and (b) the simplified electronic state diagram of singlet and triplet states.

The concentration of excitons in conjugated polymers under illumination is directly dependent on the intensity of incident light. Compared to field effect or dopant induced

concentrations, the exciton concentration in conjugated polymers due to illumination of sunlight is much lower. For a back of the envelope calculation, consider the benchmark polymer, P3HT. P3HTs absorption lies in the region of highest incident solar photon flux (~4.5 x $10^{17}$ photons $cm^{-2}$ $s^{-1}$ $\mu m^{-1}$),[33] with an absorption coefficient of ~$10^5$ $cm^{-1}$.[34,35] Given P3HT's high absorption strength, a 100nm thick thin film absorbs roughly 60% of incident light in the 200 nm wide wavelength region of high absorbance. With a reported exciton lifetime of 0.4 ns in P3HT,[36] this would yield a steady state exciton density of ~2 x $10^{12}$ $cm^{-3}$.

This photo generated exciton density is much lower than the available charge carrier density in conjugated polymers generated through dopants or the field effect, due to the limited exciton lifetime. Thus for excitons to significantly contribute to the charge carrier density in conjugated polymers, they must rapidly be split into their constituent holes and electrons. In order for an exciton in a conjugated polymer to dissociate into a free electron and hole it must encounter an inhomogeneous energy landscape, where the energetic driving force favoring dissociation out weighs the exciton binding energy. This most commonly occurs at the conjugated polymer interface with a material with disparate energy levels. Thus, the ability excitons to dissociate and contribute free charge carriers is dependent on the ease by they can be transported to an energetically favorable interface.

### *2.3.4 Diffusion and Drift*

Generally, charge transport can be driven by a concentration gradient (diffusion) or a potential gradient (drift). In the case of diffusion, charge transport can be described using Fick's second law, which in one dimension is given as:

$$J = -D\frac{\partial n}{\partial x}$$

Where $J$ is the current density, $n$ is the charge carrier density, and $D$ is the diffusivity. In the case of net neutral species, such as excitons, only diffusion occurs. In such a case, a concentration gradient is the driving force for transport, with carriers moving from regions of high carrier concentration to low carrier concentration. The diffusivity can be related to a characteristic diffusion length, $L$, by a characteristic time, $\tau$, which in the case of excitons is the exciton lifetime.

$$L = \sqrt{D\tau}$$

Similarly to concentration gradient driven diffusion, charge transport driven by a potential gradient (electric field). Termed drift, this behavior can be described using Ohm's law, which in one dimension is given as:

$$J = \sigma E$$

Where $\sigma$ is the conductivity and $E$ is the electric field or potential gradient. The components of the drift and diffusive charge transport can be linearly combined to describe overall transport in a conducting material.

Additionally, the diffusivity and conductivity can be related through the fundamental parameter of charge carrier mobility, $\mu$. The diffusivity and mobility of charge carriers are linked through the Einstein relationship:

$$D = \frac{\mu k_B T}{q}$$

Where $k_B$ is Boltzman's constant, $q$ is the elementary charge, and $T$ is absolute temperature. Likewise, conductivity is simply the product of charge carrier mobility,

charge carrier density, and the elementary charge:

$$\sigma = en\mu$$

While these relations were derived for more idealized systems, they generally hold true for π-conjugated polymers.

### *2.3.5 Activated Charge Transport*

Due to the fact that charge carriers in conjugated polymers are coupled to local structural and electronic deformations (polaron, bipolarn, polaron-exciton), for the most part they do not exist as fully delocalized free carriers, like those in traditional semiconductors and metals.[37] Charge transport of free carriers in traditional materials is limited by scattering events with impurities and phonons, which leads to a negative temperature dependence of charge carrier mobility.[17] Instead, charge carriers in conjugated polymers move through a series of thermally activated hops from available state to available state, which leads to a positive temperature dependence of charge carrier mobility. The necessity of thermal energy for these hopping processes to transpire leads to a positive temperature dependence of carrier mobility, which can be most simply modeled with the Arrhenius relationship:

$$\mu = \mu_o \exp\left(\frac{-E_A}{k_B T}\right)$$

Where $\mu_o$ is the mobility at infinite temperature where all states are accessible, $E_A$ is the average activation energy of the hopping process, $k_B$ is Boltzmann's constant, and $T$ is the absolute temperature.

Due to its simplicity an Arrhenius relationship fails to directly account for a variety of factors, such as the electronic density of states, trap states, field dependence, *etc*. A

variety of models have been applied to describe charge transport in conjugated polymers, including previously developed models for insulators, disordered systems, and models developed in concert with experimental studies of conjugated systems. The Poole-Frenkel behavior describes transport in insulating materials, and incorporates a field dependence that counteracts the activation energy, or strength of localization.[38]

$$J \propto \exp\left(\frac{-\left(E_A - \beta F^{1/2}\right)}{k_B T}\right)$$

Where $F$ is the electric field. Poole-Frenkel like field dependence has been observed in a variety conjugated polymer systems, and is incorporated into more complex charge transport relationships.

The Mott variable range hopping model was developed to describe charge transport in localized disordered systems, and considers both the spatial and energy separation of transport states when calculating the probability that a hopping process will occur.[39] The Mott model has a dimensional exponent not occurring in the simple Arrhenius relation, with the exponential term being raised to the power of *1/(1+d)*, where *d* is the dimensionality of the system. Thus for three dimensions, the mobility in the Mott variable range hopping model trends as:

$$\mu \propto \exp\left(\frac{T_0}{T}\right)^{1/4}$$

Where $T_o$ is a characteristic temperature of the hopping process.

Alternatively, for disordered localized systems, Efros and Shklovskii incorporated the idea of the existence of a Coulombic energy gap.[39] Consequently, due to the Coulomb gap the Efros-Shklovskii model maintains a constant exponent of one half,

regardless of dimensionality, giving:

$$\mu \propto \exp\left(\frac{T_0}{T}\right)^{1/2}$$

It should be noted that experimental reports have shown a temperature dependent transition from low temperature Efros-Shklovskii transport, to higher temperature Mott transport.[40]

All of the above models assume a constant density of states, but this does not hold for conjugate polymers. Many models have incorporated added complexity to account for the density of states, assuming Gaussian and exponential distribution shapes, and various combinations of the two. The most common model is the Gaussian disorder model.[41] However, this model requires extensive modification to account for transport behavior at very high charge density. Today, there still remains no single model that adequately incorporates the temperature, field, and charge density effects simultaneously, impart because there are very few comprehensive data sets covering all of these variables.

### *2.3.6 Density of States and Disorder Effects*

Regardless of the chosen model, some qualitative considerations must be made to interpret experimental $\mu$ vs $T$ data. First, the density of electronic states in conjugated polymers is not constant. At the low charge densities typically achieved in conjugated polymer devices, only states in the tail of the density of states are filled. Thus, as more states are filled, the amount of accessible empty states increases, the rate of hopping increases, and the mobility increases. This dependence of charge mobility on charge density has been experimentally demonstrated in conjugated polymers. Taking this into account one could reasonably expect that if the charge density is such that half the

density of states is filled, a maximum in charge mobility would occur, and if the local density of states is high enough free electron like transport could occur.

However, running counter to the effects of a non-constant density states is disorder, and concomitant localization, introduced with increased charge density. This is especially amplified in molecularly or electrochemically doped polymers, where the dopant ions introduce significant structural disorder in addition to electrostatic disorder.

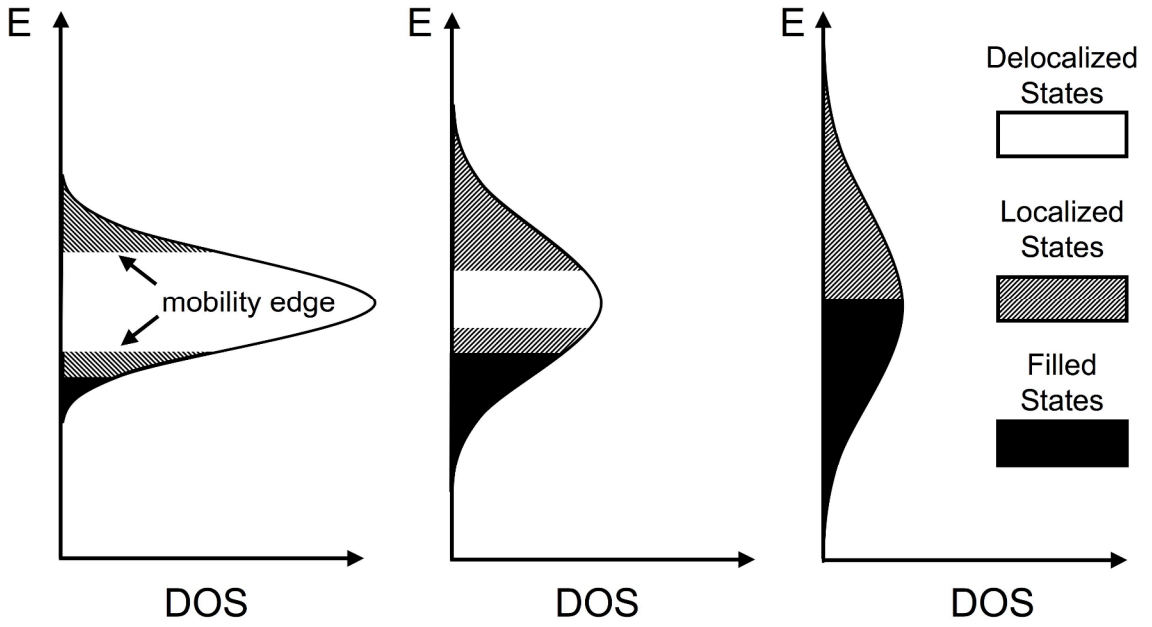


**Figure 2.11** Schematic density of electronic states with increasing charge density illustrating the concomitant increasing localization, broadening of the DOS, and shifting of the mobility edge.

A convenient formalism to combine and describe these two effects is the mobility edge.[39] In disordered materials in regions of low density of states, *e.g.* the distribution tails, charge carriers can be considered localized. The localized states lie below the mobility edge, whose position is determined by the degree of disorder. If the charge

density is increased sufficiently that the density of states is filled beyond the mobility edge, the carriers in those states can move as free carriers. However, the effect of increased charge density is increased disorder, which broadens or smears out the density of states distribution, decreases the local density of states, and shifts the mobility edge to higher and higher charge densities. This is reflected in the experimental difficulty to readily and reproducibly transcend activated hopping and achieve free carrier or metallic like transport in conjugated polymer systems.

# *3. π-Conjugated Polymer Devices*

Since the initial studies nearly fifty years ago, conductive π-conjugated polymers have been incorporated into devices for applications such as: light emission, light harvesting, photodetection, chemical and biochemical sensing, electrically stimulated actuation, solid state memory, logic circuits, and charge storage.[42,43,44,45,46,47,48,49] This has been possible due to seemingly endless ability to synthetically tune the properties of conjugated polymers for any given application. In this thesis, three classes of devices were especially relevant, namely the field effect transistor, electrochemical transistor, and bulk heterojunction solar cell.

## *3.1 Field Effect Transistor*

In 1986, the first polymer semiconductor based field effect transistor was reported.[50] Field effect transistors (FETs), as they are aptly named, employ the field effect (discussed in chapter 2.3.1) to modulate charge density, and thus conductivity, in a semiconducting material. This allows the FETs to be employed as electrical switches in logic circuits and amplifying stages in signal processing. Especially important in semiconducting materials research is the use of FETs as test beds the extract a materials carrier mobility.

### *3.1.1 Device Structure and Operating Principles*

When conjugated polymers are employed as the semiconducting material in a FET, they are most often are incorporated into a structure termed a Thin Film Transistor (TFT). TFTs share all the common components of a FET, but are fabricated through the

deposition of a thin layer of semiconductor onto a substrate, as opposed to the processing of a macroscopic piece of semiconductor. As with FET in general, a TFT is a three terminal devices with a metal source and drain electrode are separated by a channel of semiconducting conjugated polymer thin film, which is capacitively coupled in a field effect structure to a third metal gate electrode, Figure 3.1. The insulating layer, which capacitively couples the channel and gate electrode, is commonly silicon dioxide, but a wide variety of oxides, insulating polymers, and even air/vacuum gaps have been employed.[51,52]

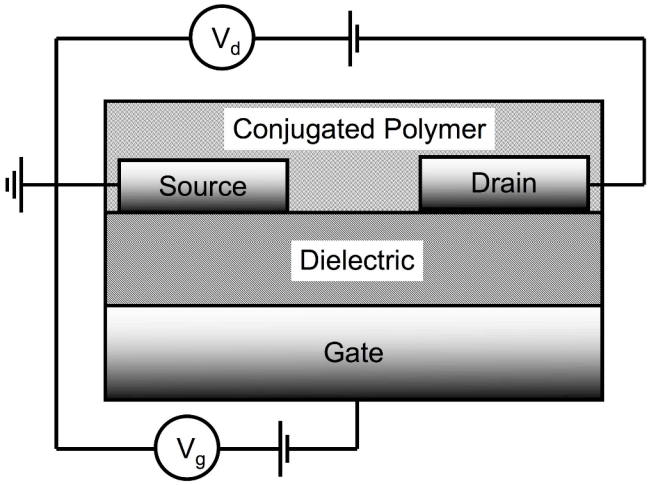


**Figure 3.1** Schematic diagram of a conjugated polymer based field effect transistor structure.

Upon a positive (negative) gate bias, electrons (holes) are able to be injected from the source and drain contacts and to accumulate at the semiconductor/insulator interface. Applying a bias between the source and drain drives the accumulated carriers through the semiconducting channel, Figure 3.2. A convenient formalism is to visualize an applied gate bias as shifting the energy levels either up such that the HOMO can partially empty allowing hole accumulation, or down such that the LUMO can partially fill with

accumulated electrons. To drive current flow, a bias is applied between the source and drain electrodes, with a negative bias allowing holes to "float" uphill toward the drain, or a positive bias allowing electrons to "fall" downhill toward the drain.[53]

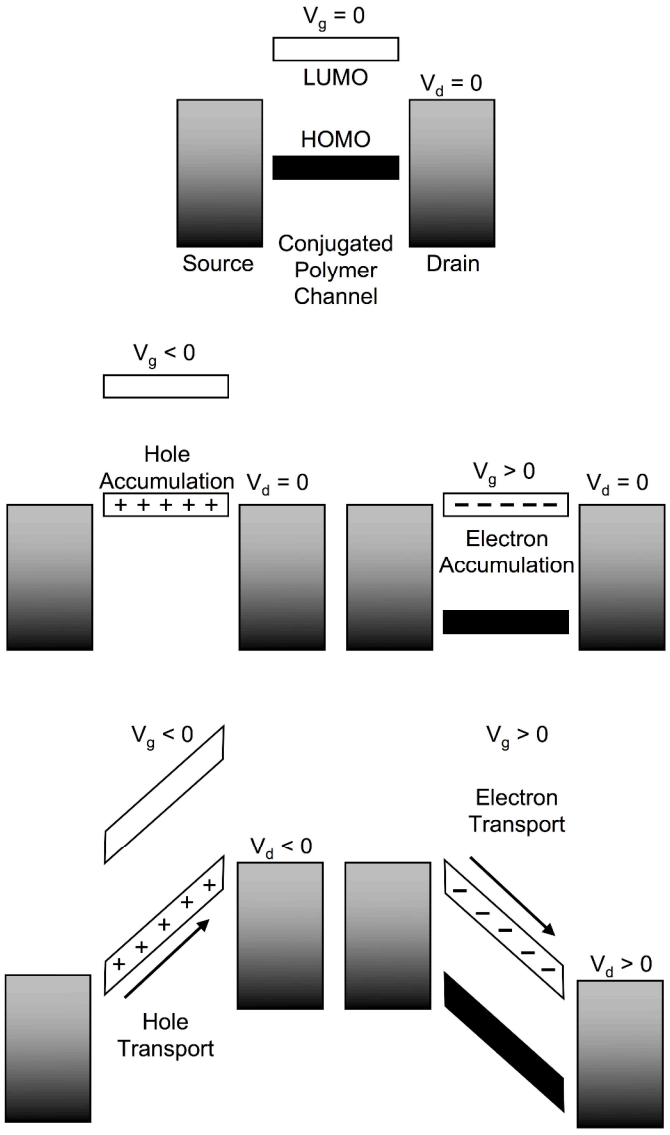


**Figure 3.2** Energy band diagram of a conjugated polymer field effect device under various applied gate and drain potentials illustrating hole and electron accumulation and transport, adapted from reference [53].

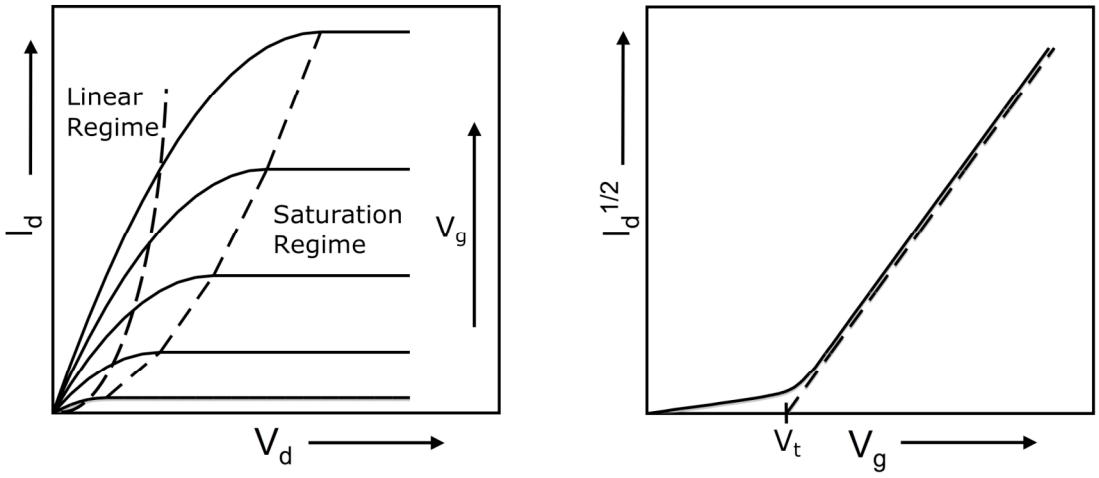


**Figure 3.3** Transistor output curves ($I_d$ *vs* $V_d$) and saturation transfer curves ($I_d^{1/2}$ *vs* $V_g$).

### *3.1.2 Device Model and Figures of Merit*

TFT structures are generally evaluated either by holding the source and gate at a fixed bias and sweeping the drain potential, creating an output curve, or holding the source and drain at a fixed bias and sweeping the gate potential, creating an transfer curve, Figure 3.3. The current flow in TFTs is dominated by field driven charge carrier drift. Thus Ohm's law, written as:

$$I = \frac{W \times H}{L} \times en \times \mu \times V$$

Or:

*Current = Geometric Factors x Number of Charges x Mobility of Charges x Field*

For a transistor this becomes:

$$I_d = \frac{W}{L} \times C_{ox}\left[\left(V_g - V_t\right) - \frac{V_d}{2}\right] \times \mu \times V_d$$

Where $I_d$ is the current collected at the drain electrode, $W$ is the width of the

semiconductor channel, $L$ is the length of the semiconductor channel, $C_{ox}$ is the capacitance of the insulating layer separating the semiconductor channel from the gate electrode, $V_g$ is the voltage applied at the gate electrode, $V_t$ is the threshold or turn on voltage of the transistor, $V_d$ is the voltage applied at the drain electrode, and $\mu$ is the charge carrier mobility. Since the a TFT is a three terminal device, Ohm's law is now complicated as there is a potential dependence to the charge carrier concentration, $n$, which is now dependent on the applied gate and drain potentials and the capacitance of the insulating layer.

The two key extractable parameters from thin film transistor evaluation are the threshold voltage and the charge carrier mobility. The threshold voltage represents the relative ease with which a conducting sheet of charge carriers can be accumulated in the semiconductor channel. This parameter includes factors such as the potential difference of the work function of the metal source/drain electrodes and the molecular orbital levels of the conjugated polymer employed as the semiconductor channel, the potential difference between the gate metal electrode work function and the Fermi level in the semiconductor channel, and the existence of electronic states in which charge carriers can become trapped. $V_t$ is arbitrarily determined from the intercept of the model used to extract charge carrier mobility.

Mobility, the most important device parameter, can be obtained by analyzing the current voltage behavior of a TFT. Treating the source electrode as the ground, when the drain potential is less than the applied gate potential minus the threshold, $V_d < V_g - V_t$, and $V_g$ is greater than $V_t$, the device is said to be operating in the linear regime. In this

regime, the above transistor equation holds, and is rearranged, generally appearing as:

$$I_d = \frac{\mu W C_{ox}}{L}\left[\left(V_g - V_t\right)V_d - \frac{V_d^2}{2}\right]$$

For small values of $V_d$, the $V_d^2$ term becomes negligible, and $I_d$ is linearly dependent on $V_d$ and current voltage behavior is essentially Ohmic. Additionally, in the linear regime $\mu$ is readily extracted from the slope of $I_d$ vs $V_g$:

$$\mu = \frac{L}{W C_{ox} V_d}\frac{\partial I_d}{\partial V_g}$$

When $V_d$ exceeds $V_g$ less $V_t$, $V_d > V_g - V_t$, the drain current ceases to be dependent on drain bias and is said to be operating in the saturation regime and is modeled by the following equation:

$$I_d = \frac{\mu W C_{ox}}{L}\left(V_g - V_t\right)^2$$

In the saturation regime the mobility can be extracted from the slope of $\sqrt{I_d}$ vs $V_g$:

$$\mu = \frac{L}{2 W C_{ox}}\left(\frac{\partial \sqrt{I_d}}{\partial V_g}\right)^2$$

Physically, saturation occurs when the voltage between the source and drain is great enough to drive the accumulated charge density to zero near the drain, *i.e.* the potential difference between the gate and drain is zero or opposite in sign needed to accumulate carriers.

## *3.2 Electrochemical Transistor*

The electrochemical transistor works under the same basic premise as a FET. Through control of electrochemical potential, the charge density is modulated in a

semiconductor channel in order to control or switch the semiconductors conductivity. The key difference is that the electrical insulator, which capacitively couples the semiconductor channel and gate electrodes in a FET device, is replaced with an electrically insulating, but ionically conducting, electrolyte.

### *3.2.1 Electrolyte Gates*

These electrolyte gates come in come in a variety forms, the simplest of which is a dielectric liquid solvent with a dissolved ionic solute (salt). The various combinations of solvent and salt are nearly endless, but divided between aqueous and nonaqueous. Aqueous electrolytes have a limited window of voltage stability due relatively low potential at which electrolysis occurs. There are a many polar and non-polar organic solvents that provide adequate electrochemical windows when applied in electrolyte systems. To achieve very wide electrochemical windows, cooled liquid $SO_2$ can be used as an electrolyte solvent.[54]

Ionic liquids, or room temperature molten salts, represent a more exotic class of liquid electrolyte gates.[55] Consisting of asymmetric, bulky, and often organic anions and cations, ionic liquids are loosely defined as having a melting or glass transition below 100°C. Thus they form a molten ionically dissociated liquid with out the necessity of any solvent. Additionally, due to their molten nature, ionic liquids have a negligible vapor pressure, and will often decompose before they are able to evaporate. The synthetic tunability of ionic liquid anions and cations lead to a near infinite combination of ionic liquids. This has lead to the development of ionic liquids with wide electrochemical window, low viscosities, and high ionic conductivities.

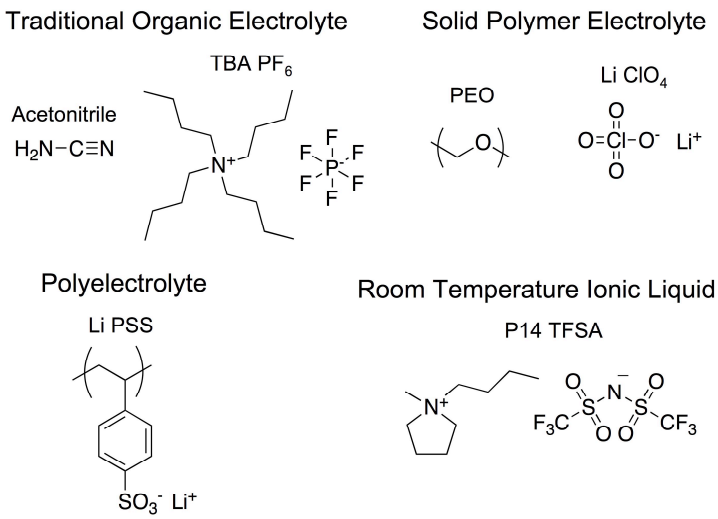


**Figure 3.4** Examples of electrolyte systems used to gate conjugated polymers.

When incorporated into functional devices, it is desirable for the electrolyte gate to be solid form. Many liquid electrolytes can form a mechanically stable film through the addition of a gelation agent. However, any volatile solvents are susceptible to evaporation. Ionic liquids, when gelled with copolymers, have been quite successful as electrolyte gates.[56] Gelled ionic liquids, or ion gels, have been incorporated as electrolyte gates into a variety of printed electronic circuits, including ring oscillators, electrochromic displays, memory circuits, and drive stages for organic light emitting diodes.[57,58,59] Ion gels combine excellent mechanical stability with nonvolatility making them ideal candidates for printed electronic devices.

Some polymers have sufficient ionic conductivity that they can simply replace the liquid solvent creating a solid polymer electrolyte. Solid polymer electrolytes have been studied extensively for use in battery and super capacitor applications.[60] The prototypical solid polymer electrolyte system is lithium perchlorate dissolved in poly(ethylene oxide), PEO. PEO is an effective host polymer for solid polymer electrolytes because the ether

oxygen coordinates strongly with cations. Ion motion is considerable, because the energy barrier restricting segmental motion of the polymer chain is low.[60] This allows conformational changes in the polymer to assist ion transport. Solid polymer electrolytes based on $LiClO_4$ dissolved in PEO have been utilized as gate materials for polymer semiconductors.[61]

Alternatively a polyelectrolyte, a polymer with incorporated anion or cation repeat units, can be used. In such a case the counter ion to the polyelectrolyte is the only mobile ionic species, with the polyelectrolyte locally reorganizing to facilitate the counter ion motion. Poly(styrene sulfonate), PSS, paired with lithium of hydrogen cations, has been demonstrated as a functional electrochemical gate for conjugated polymer systems.[62,63]

Additionally, porous silicon dioxide films have displayed suitable ionic conductivity to be employed as electrolyte gates, though these types of materials lie outside the scope of this thesis.[64] However all these materials set share a common feature. Whereas traditional gate dielectrics rely on the polarization of a static dielectric film, all of these electrolyte gate systems rely on the physical motion of charged ions to induce carriers in a semiconducting material.

### *3.2.2 Operating Principles*

Similarly to TFT devices discussed previously, electrochemical transistors are three terminal devices with a metal source and drain electrode separated by a channel of semiconducting conjugated polymer thin film. This conjugated polymer channel is electrochemically coupled to a third metal gate electrode through an electrically insulating ionically conductive electrolyte, Figure 3.5.

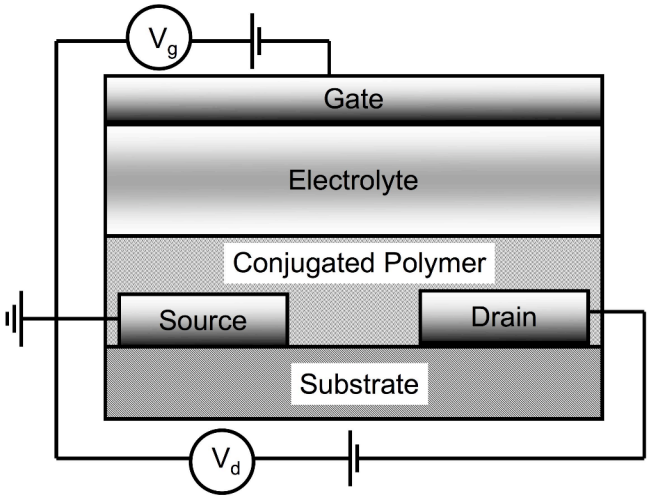


**Figure 3.5** Schematic diagram of a conjugated polymer based electrolyte gated transistor structure.

Upon the application of a negative (positive) gate bias, cations (anions) are attracted to the gate electrode electrolyte interface, forming an electric double layer. Simultaneously, oppositely charged anions (cations) are driven towards the interface of the conjugated polymer and the electrolyte, stabilizing holes (electrons) in the polymer film. These ion stabilized charge carriers that are able to be driven from the source to the drain, through the conjugated polymer, with an applied source-drain bias.

The process of charge accumulation in electrolyte gated conjugate polymers is completely analogous to cyclic voltammetry of conjugated polymer thin films. Hole accumulation is the result of oxidation of the polymer, while electron accumulation is the result of reduction. This accumulation most often occurs in a three dimensional manner, with ions penetrating the polymer film. Alternatively, a two dimensional sheet of charge can be induced in the conjugated polymer channel through the formation or an electric double layer. This occurs when the ions are unable to penetrate the polymer film, such as when a polyelectrolyte, which is too bulky to efficiently transport into the conjugated polymer film, is employed. Applying a bias between the source and drain drives the

accumulated carriers through the semiconducting channel.

### *3.2.3 Device Model and Figures of Merit*

Electrochemical transistor current-voltage behavior can be empirically described with the same models used to describe traditional FETs, discussed previously.[65] The same linear and saturation behavior has been observed in electrolyte-gated devices, and nearly identical current-voltage relations have been derived. The key parameters are still the charge carrier mobility, $\mu$, and the threshold voltage, $V_t$. In some cases, when the channel length is large, and the source-drain bias is small, a simple application of Ohm's law is reasonable, with $\mu$ being extractable from the measured conductivity by estimating the carrier density.

### *3.2.4 Referenced Potential Methods*

One distinct opportunity available in electrochemically-gated transistors, not available in traditional FETs, is the ability to insert a fourth electrode to measure the average potential of the semiconducting channel.[66] Since electrolyte gates consist of mobile ion species, under an applied gate bias the ions reorganize, distributing themselves to minimize electric fields in the bulk of the electrolyte gate. Ideally, the applied potential is dropped at the interfaces of the electrolyte with gate electrode and the semiconductor channel, with potential of the bulk remaining constant, Figure 3.6. For electrolytes with high ionic conductivity, such as ones based on ionic liquids, this idealized assumption holds true. In such systems, a fourth electrode can inserted into the bulk of the electrolyte gate, and used to measure the potential drops at the electrolyte interface with the semiconductor channel and the gate electrode. This reference electrode is not intended to pass current, but instead is desired to maintain a stable potential, which

the gate, source, and drain potentials can be measured in reference to. This allows a decoupled view of the relative potential changes at the semiconductor and gate interfaces under an applied gate bias. That is, the change of the potential of semiconductor channel, in our case a conjugated polymer, is directly accessible.

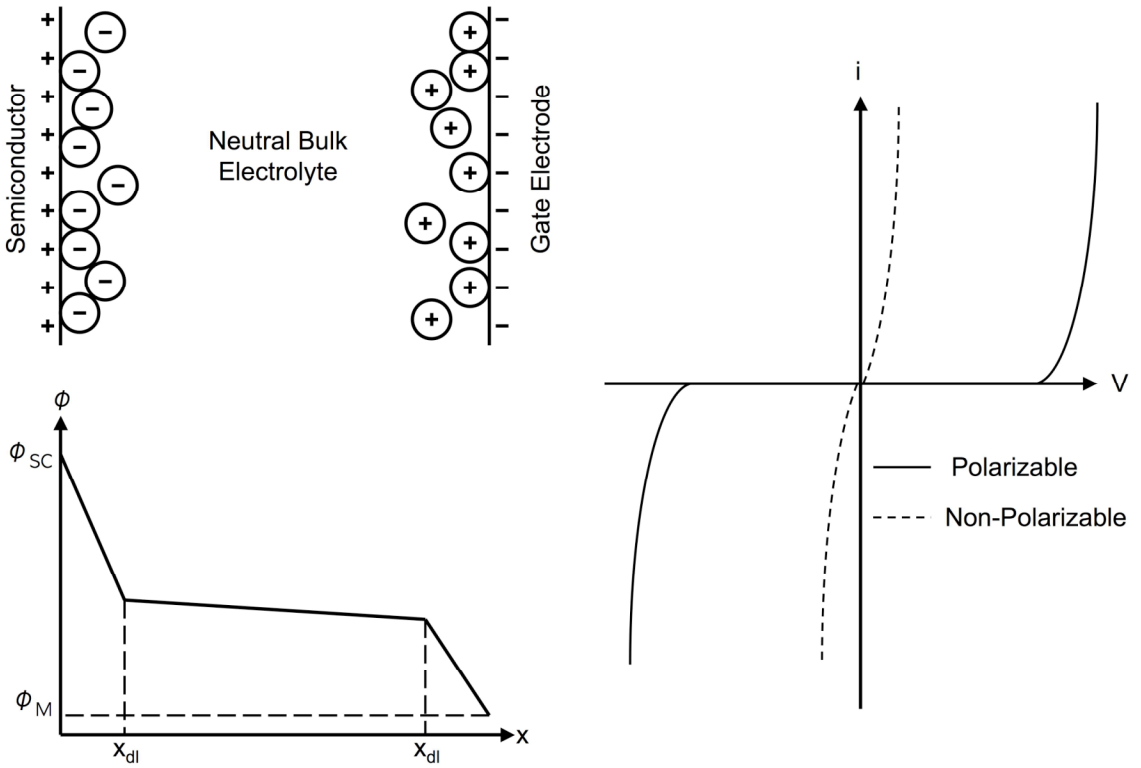


**Figure 3.6** Potential distribution in an electrolyte gate under applied gate bias, and the current voltage behavior of a polarizable gate electrode and a non-polarizable reference electrode.

The potential stability, required of a reference electrode, is achieved by choosing a non-polarizable electode system. A non-polarizable is one which where the passage of very large current densities is required to shift the electrodes potential. This is contrasted with the gate electrode, which is desired to be ideally polarizable, with large shifts in potential achieved with the passage of very small very small current densities, Figure 3.6. Often, stable reference potentials are achieved by incorporating a reference electrode

metal that is in equilibrium with its reduced form, such as the Ag/AgCl reference electrode. However, such electrodes require a structure that encapsulates a constant concentration solution around the electrode, which then forms a junction with the electrolyte system of interest through a porous glass frit.

As if often the case with electrochemically gated transistor devices, such a complex reference electrode is difficult to incorporate into a functioning electrolyte gate, so a simpler bare metal wire quasi-reference electrode is used. Quasi reference electrodes have shown adequate potential stability that they are widely used in electrochemical research. Since quasi-reference electrodes due not have a defined redox couple, their equilibrium electrochemical potential is not explicitly known, and must be measured. This is readily achieved through the addition and electrochemical measurement of a calibrant, whose redox potentials are know. The most common calibrants are ferrocene, and cobaltocene (existing as a cobaltocenium salt), Figure 3.7.

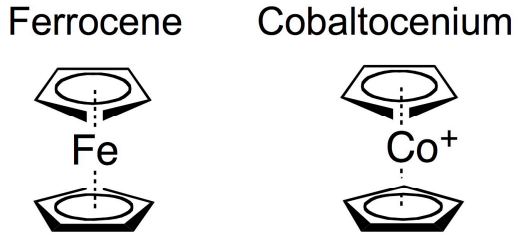


**Figure 3.7** Chemical structure of common reference electrode calibrating redox couples ferrocene, and cobaltocenium.

Calibrated quasi-referenced potential measurements allow direct comparison between different experiments and material sets. In addition, the calibrated quasi-referenced potentials are convertible to the absolute vacuum energy scale, since the

absolute position of calibrant redox processes have been determined.[67] The unique nature of electrolyte gates and there amenability to calibrated reference potential methods allows the determination of the absolute potential of a conjugated polymer, and the absolute potential dependence of charge accumulation and conduction, all of which are key to understanding the nature of the electronic structure and charge transport mechanisms in conjugated polymers.

## *3.3 Bulk Heterojunction Photovoltaic Cell*

Conjugated polymers were first incorporated into solar cell devices in 1993, since then there has been a vast expansion of interest in conjugate polymer materials for potentially cheap efficient large area solar energy conversion.[68] As of writing this thesis, laboratory devices have reportedly achieved an efficiency of nearly 9% of the incident solar energy converted into usable electrical energy.[69] This approaches the efficiency of commercially available amorphous silicon solar cells, making conjugated polymers materials an integral part of emerging renewable energy technology.

### *3.3.1 Excitonic Solar Cells*

Photovoltaic devices serve to generate electrical power from incident sunlight. This is accomplished by the photogeneration of an electrical current and voltage due to the absorption of light. When a conjugated polymer absorbs a photon of light, the resulting excited electron and created hole are not free to current contributing charge carriers, instead they are coulombically bound to one another as an exciton. Thus conjugated polymer solar cells fall under the broader umbrella of excitonic solar cells. In order break up the exciton to be broken up, freeing the electron and hole to be able to contribute to

current, the exciton must encounter an inhomogeneous energy landscape where there exists an energetic driving force, greater than the exciton binding energy, to spatially separate the electron and hole.

In conjugated polymer solar cells, excitonic dissociation is most commonly accomplished at a donor-acceptor interface, where an electron rich (donor) conjugated polymer comes in contact with electron poor (acceptor) material, most commonly a fullerene derivative. In general the fullerene acceptor has a deeper LUMO level than the donor polymer, such that it is favorable for a charge transfer reaction to occur, with the excited electron in donor LUMO transferring (being donated) to the acceptor LUMO. Likewise, the HOMO of the acceptor is deeper than that of the donor, making charge transfer of the hole from the donor unfavorable. Thus with the charge transfer of the electron to the acceptor material, and the hole remaining on the donor, the exciton is split.

The dissociated electron and hole are then free to transport to the cathode and anode respectively to be collected. This transport occurs through hopping processes discussed in Chapter 2. The anode material is chosen such that its work function allows facile extraction of holes from the donor conjugated polymer, likewise the cathode material is chosen to facilitate electron extraction from acceptor material. The cathode and anode are both connected to an external load, thus completing the circuit. This entire process of light absorption, exciton formation, exciton diffusion, exciton dissociation, charge transport, and charge collection is represented schematically in Figure 3.8.

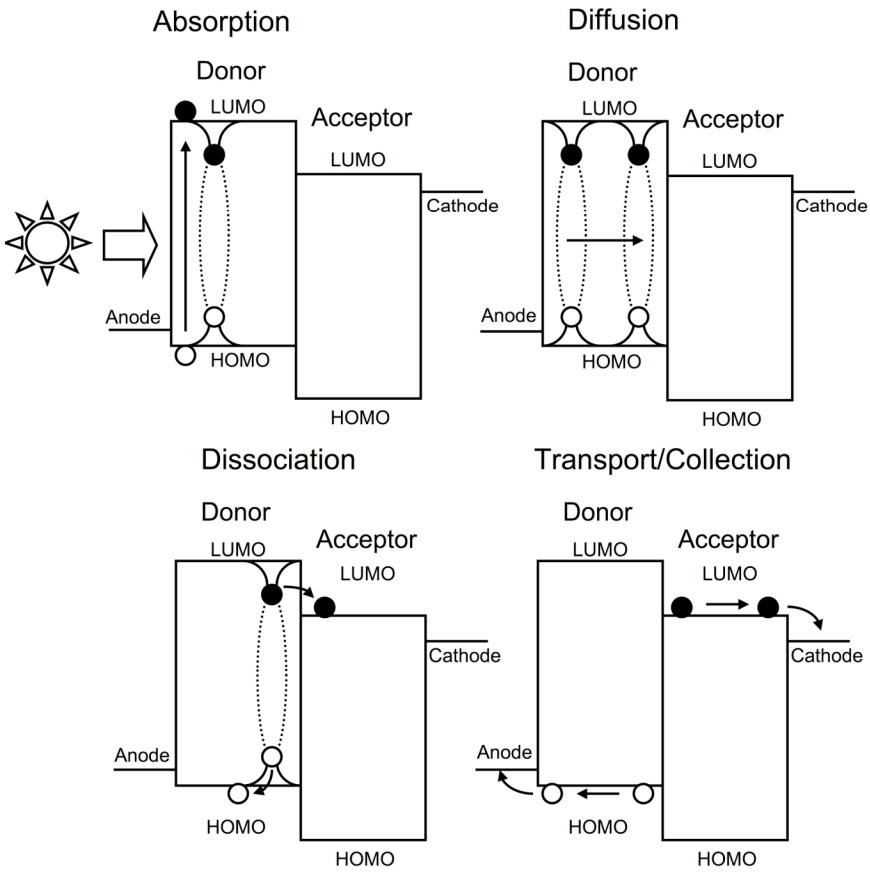


**Figure 3.8** Excitonic solar cell energy level diagrams illustrating the processes of light absorption, exciton diffusion, exciton dissociation, and carrier collection.

Since excitons are a neutral species, they cannot be driven towards the donor acceptor interface with a field, instead they must rely on diffusion to transport them to an interface where they can dissociate. Due to their short lifetimes, excitons in conjugated polymers have severely limited diffusion lengths, on the order of 10 nm.[70] Since efficient absorption of incident light requires ~100 nm of absorbing conjugated polymer, however most of the excitons created throughout the thickness of the absorbing polymer are unable to diffuse to a dissociating interface before the recombine without contributing to

the current of the photovoltaic device. These small diffusion lengths render polymer solar cells consisting of a simple donor-acceptor bilayer incapable of efficient operation, though this is not true of other material sets. In order to overcome this diffusion limitation, the interfacial area between the donor and acceptor has been maximized through the development of nano-scale phase separated donor-accept blends, termed bulk heterojunctions.

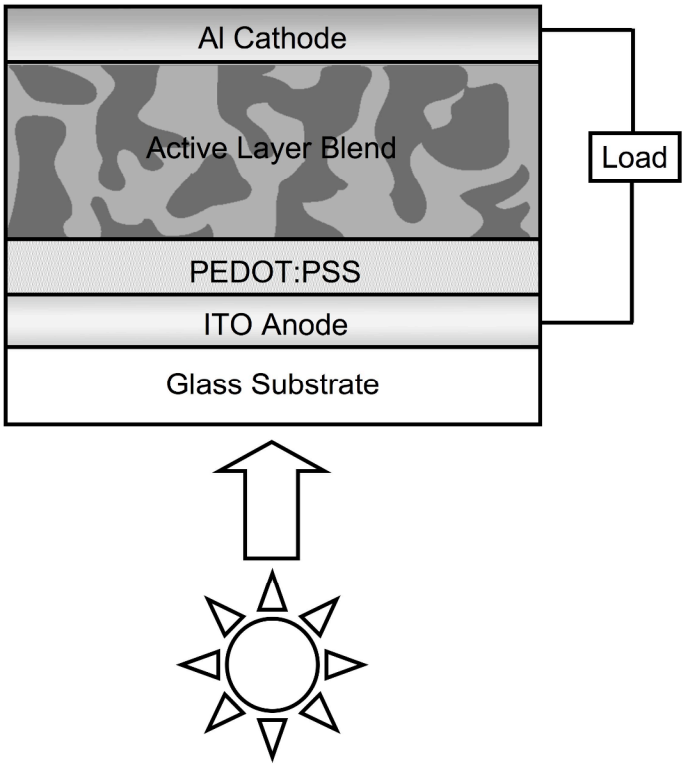


**Figure 3.9** Schematic diagram of a bulk heterojunction photovoltaic cell.

### *3.3.2 Device Structure*

Shown in Figure 3.9, typical conjugated polymer bulk heterojunction laboratory devices exist of a glass substrate coated with a optically transparent electrically conductive film of indium tin oxide, which has been coated with a layer of transparent

poly(styrenesulfonate) doped poly(3,4-ethylenedioxythiophene), PEDOT:PSS. The PEDOT:PSS layer is used to improve the energy level alignment with the donor material, improving hole collection. Atop the PEDOT:PSS layer is the active absorbing layer blend of conjugated donor polymer and acceptor fullerene. This layer is optimized for thickness and donor-acceptor ratio to maximize light absorption, exciton dissociation, and charge transport/collection. Finally a cathode, often aluminum, caps the device. The cathode material is chosen such that its work function is sufficiently shallow to efficiently allow the collection of electrons from the active layer.

### *3.3.3 Figures of Merit*

Bulk heterojunction photovoltaic devices function as diodes, displaying highly asymmetric current-voltage behavior. In the absence of illumination, in reverse (negative) bias, there exists a small current, referred to as the reverse saturation current. Conversely, in forward (postive) bias, the bulk heterojunction can pass very large currents. Illumination induces a negative photogenerated current running in the opposite direction of the forward bias diode current, which at zero bias is referred to as the short circuit current density, $J_{sc}$. At some positive voltage, the photogenerated current is exactly balanced by the forward bias diode current, which defines the open circuit voltage, $V_{oc}$. The $J_{sc}$ and $V_{oc}$ are key parameters in describing photovoltaic performance.

Along the illuminated *J-V* curve, Figure 3.10, there exists a point where the magnitude of the product of the current and voltage (power) is maximized, referred to as the maximum power point. The maximum power point is inevitably smaller in magnitude than the product of the $J_{sc}$ and $V_{oc}$, and the ratio of these two products is referred to as the fill factor, *FF*. The fill factor is defined as the following:

$$FF = \frac{J_{mp} \times V_{mp}}{J_{sc} \times V_{oc}}$$

Fill factor is a convenient unit-less parameter by which to assess solar cell performance. The ratio of the maximum power point and the power of the incident light is the overall power conversion efficiency, *PCE*, and can be related to the $J_{sc}$ and $V_{oc}$ through the fill factor:

$$PCE = \frac{J_{sc} \times V_{oc} \times FF}{I_{light}} \times 100\%$$

Where $I_{light}$ is the intensity, or irradiance, of the incident light.

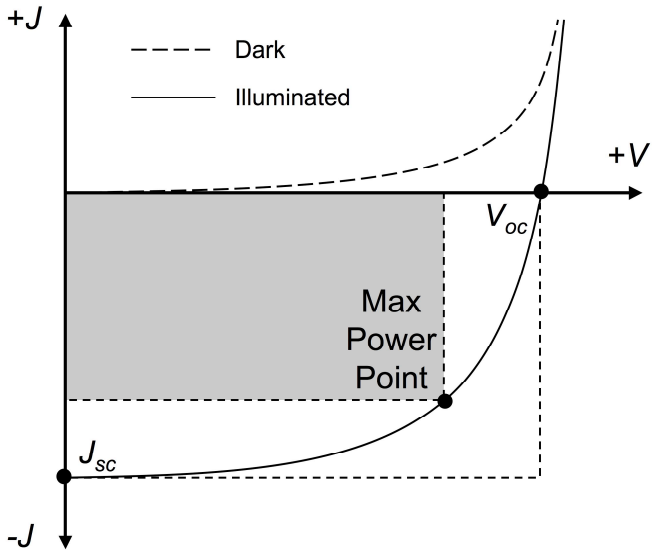


**Figure 3.10** Dark and illuminated bulk heterojunction *J-V* curves.

Generally the incident light is filtered and attenuated to simulate the solar spectrum according to ASTM standards. An alternate assessment of photovoltaic performance is the wavelength dependent incident photon-to-current efficiency, *IPCE*, also commonly referred to as the external quantum efficiency, *EQE*. The *IPCE* is determined by

measuring the monochromatic short circuit current density, $J_{sc,\lambda}$, with the *IPCE* being defined as:

$$IPCE = \frac{J_{sc,\lambda} \times h \times c}{I_{\lambda} \times q \times \lambda}$$

Where $h$ is Planck's constant, $c$ is the speed of light, $q$ is the elementary charge, $\lambda$ is the wavelength of the incident light, and $I_{\lambda}$ is the intensity of the incident monochromatic light. Thus while *PCE* is a single value, *IPCE* is a wavelength dependent distribution of values.

Connecting these parameters to physical processes is important to interpreting experimental results. *FF* is dependent of a variety of processes within a bulk heterjunction device, but for the most part reflect the issues of charge transport within the photovoltaic device. These include the magnitude of recombination and leak currents, which oppose the flow of the photogenerated current, and the overall ease of dissociated electron and hole transport and collection.[71]

Similarly, these issues affect $J_{sc}$ (and *IPCE*), which in addition is dependent on the processes of light absorption, exciton diffusion, and exciton dissociation. $V_{oc}$ is determined when the photogenerated current is exactly balanced by the forward bias diode current. The point at which this occurs in intrinsically linked to the energy difference between the HOMO of the donor and LUMO of the acceptor. Additionally, leak current opposing the flow of the photogenerated current influence $V_{oc}$, with an increase leak resulting in a decreased $V_{oc}$.[71]

# *4. Experimental Methods*

A variety of techniques were required to accomplish this these research. Here is presented the methods of film depositions used to fabricate conjugated polymer based thin film transistor and photovoltaic devices. The electrical, optical, and electrochemical charaterization techniques employed are presented. This chapter draws heavily on the PhD thesis of previous Frisbie group members Derek Stevens and Yu Xia, and is intended as reference for future Frisbie group members.[72,73]

## *4.1 Thin Film deposition Techniques*

All the device structures employed in this research were assembled by the successive deposition of thin film layers. These layers include neat polymers, doped polyelectrolytes, metallic electrodes, and transparent conductive oxides.

### *4.1.1 Substrate Cleaning and Preparation*

All structures were formed on either a glass slide, indium tin oxide coated glass wafer, or heavily p-doped silicon wafer with 3000 Å of thermally grown oxide. All substrates were prepared with successive sonications in acetone, methanol, and isopropyl alcohol for 10 minutes each. This was followed by a 10 minutes UV-ozone exposure.

### *4.1.2 Metal Electrode Deposition and Patterning*

Metal source and drain electrodes with contact pads were fabricated via a photolithography lift off process of e-beam deposited metals, performed at the University of Minnesota Nano Fabrication Center cleanroom. The standardized procedure for depositing and photolithographically patterning gold electrodes with an adhesion layer is

as follows:

1) Deposition of PR1818
   - prebake 1 min 115 $^{o}$C
   - spin coating HMDS (program #2) 3000 rpm 30 sec
   - spin coating PR1818 (program #2) 3000 rpm 30 sec
   - postbake 1 min 105 $^{o}$C

2) Exposure using MA6/BA6 Contact Aligner
   - soft contact (35 mm gap)
   - exposure time 10 sec
     log in / place the mask on the holder (let front part face upward) / press enter (to apply vacuum) / put the holder into the contact aligner / press change mask / press load / load substrate / press enter / press select program (soft contact) / press edit parameter (exposure time 10 sec, gap 35 mm) / exposure / repeat loading and exposure / press change mask / take out mask holder / press enter (to turn off vacuum) / log off

3) Development
   - water : 351 Developer = 1:4 (30 sec)
   - rinse with DI water: (5 min)
   - inspect under microscope

4) Contact Deposition using CHA e-beam evaporator
   - Cr: 25 Å (0.5 Å/sec)/ Au: 225 Å (1 Å/sec)

5) Lift-Off
   - soak in acetone (overnight)
   - rinse with acetone
   - sonicate in acetone (5 min Freq. ~45)
   - dry with nitrogen blowing

The typical source drain structures produced by this method are shown in Figure 4.1. Titanium can be used in place of chromium adhesion layer, likewise platinum may be deposited as the noble metal electrode. This procedure is can be readily used to produce metal electrodes with a wide variety of thicknesses. After electrode deposition, and before the deposition of subsequent layers, patterned substrates where cleaned as described in the previous section.

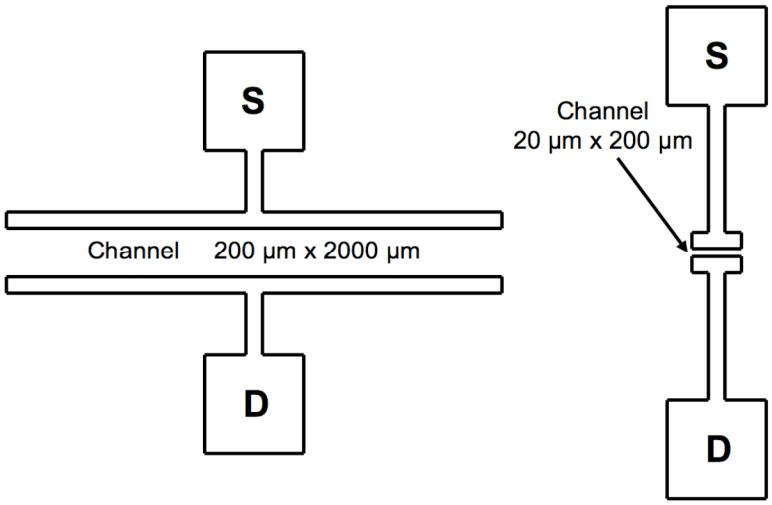


**Figure 4.1** Typical source-drain geometries patterned on $Si/SiO_2$ wafers by the liftoff process.

Simple unpatterned large area gold coated substrates were fabricated using the same e-beam process referred to above. Additionally large area electrode pads were split using a simple wire shadow mask, with the diameter of the wire determining the gap between deposited electrodes. E-beam techniques were eschewed for the deposition of aluminum cathodes employed in photovoltaic devices, due to the inevitable air exposure of devices structures before and after deposition. Instead cathode layers were produced using a thermal evaporation technique, with an evaporator apparatus housed in an inert atmosphere glovebox. The geometry of the solar cell cathodes were defined using steel shadow masks.

### *4.1.3 Conductive Oxide Patterning*

Similar to patterned metal electrodes, transparent conductive indium tin oxide, ITO, anodes for photovoltaic devices were patterned using photolithographic techniques. The key difference was the use of substrates precoated with ITO. Thus instead of a patterned

deposition, a patterned etching was carried out as follows:

1) Cut 2.5" x 2.5" pieces of ITO
2) Clean 10 min ultrasonic with IPA
3) 2 min 115ºC prebake
4) 2-3 min HMDS vapor
5) 1813 photoresist (3000 rpm for 45-60 sec)
6) Soft bake on the hot plate 5 min at 105ºC
7) Mask exposure 5 seconds (Oriel lamp)
8) Immerse in 351 Dev : $H_2O$ (1 : 3) solution for 60 seconds, until you can no longer see any rainbows on the surface or brownish clouds coming off. Recommend using a fresh developer solution.
9) Rinse with water and dry
10) Hard bake on the hot plate at 120ºC for 5 min.
11) Put the etching solution in a 600 ml beaker and place on the hot plate. Make 420 ml of 5% nitric acid, 20% HCl, by mixing 220 ml 37% HCl, 20 ml 70% $HNO_3$, and 180 ml $H_20$.
12) Set the temperature to 85ºC and allow to heat up. After a while (half hour or so), test the temperature of the bath, which should be around 50ºC.
13) Etch the substrates for 3 minutes.
14) Rinse with water and dry
15) Test with ohmmeter to see if ITO is gone.
16) Rinse with acetone followed by 10 minutes ultrasonication in acetone.

17) Cut individual 1” x 1” substrates

This produced ITO patterns with six individually addressable cathode pads per 1” x 1” substrate. As with the metal electrode deposition process, ITO patterning was performed in a cleanroom.

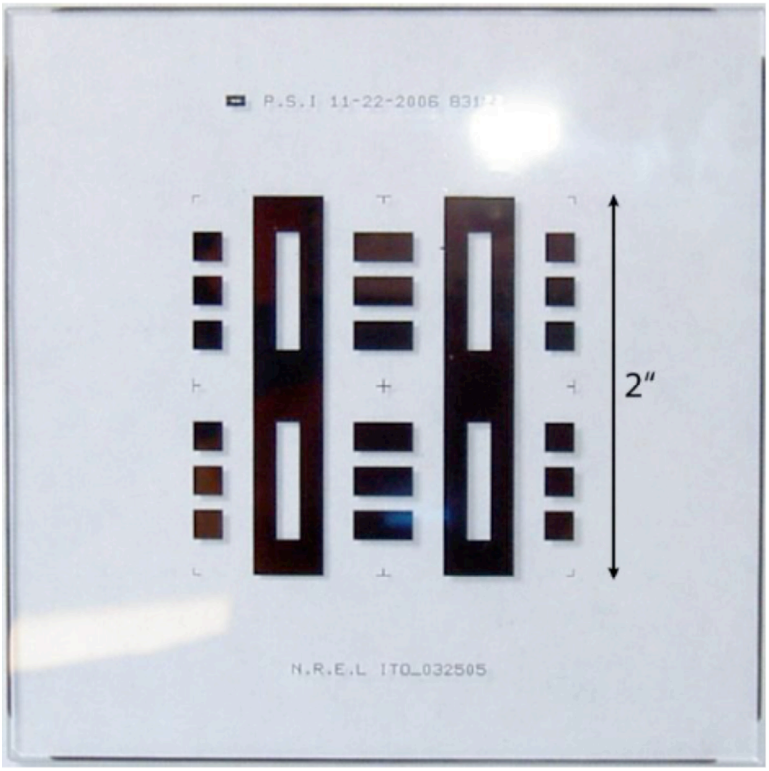


**Figure 4.2** Photolithography shadow mask used to patterned ITO coated glass susbstrates.

### *4.1.4 Spin-Coating*

In all device structures, π-conjugated layers were deposited from solution via spin-coating. Spin-coating works on the following premise: a polymer solution is placed on a substrate, the substrate is radially accelerated ejecting excess solution leaving a layer of solution, whose thickness is determined by the spin speed, solution viscosity, and

substrate surface energy. The substrate continues to spin producing a convective flow of surrounding gas over the substrate driving the evaporation of the volatile solvent leaving a film of the polymer solute. The final film thickness is a product of the solvent choice, solution concentration, and spin speed.

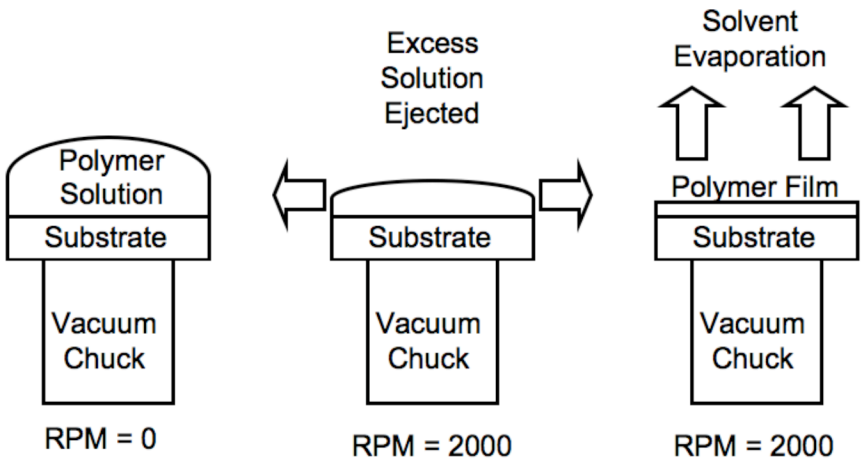


**Figure 4.3** Schematic of spin-coating, illustrating the ejection of excess solution, solvent evaporation, and polymer thin film formation.

For transistor and electrochemical transistor devices, neat π-conjugated polymers were dissolved in chloroform or 1,2-dichlorobenzene (3-30 mg/ml solvent) by stirring over night at elevated temperature. Solutions were spin-coated onto electrode patterned substrates immediately following substrate exposure to UV-ozone. Coated substrates were then baked at 100°C to drive off residual solvent. In order to decrease parasitic capacitance during electrical characterization, the polymer film for field effect transistor devices was manually patterned with a cotton swap to remove excess polymer in areas besides the transistor channel. Solution preparation, spin-coating, and baking were all carried out in a inert atmosphere glovebox. Optical absorption and cyclic voltammetry

samples were prepared in a similar manner, excluding manual patrerning, on gold coated and bare glass respectively.

Photovoltaic devices required two distinct spin-coat layers. First PEDOT:PSS was spin-coated form a commercial aqueous suspension after being passed through a 0.45 μm pore size Teflon syringe filter. The spin-coating was carried out onto ITO patterned glass substrates at 4000 rpm for 45 sec immediately after the substrates were exposed to UV-ozone. This process was repeated once more, with the two successive PEDOT:PSS spin-coatings providing a roughly ~40 nm thick film. As above, the PEDOT:PSS was manually patterned with a cotton swap to remove excess polymer, this time from locations of electrode contact pads. PEDOT:PSS coated ITO patterned glass substrates were then transferred to an inert atmosphere glovebox, where they were baked at 135°C to drive off residual water.

The second spin-coated layer for photovoltaic devices was the bulk heterojunction active layer. π-Conjugated polymers and soluble fullerene PCBM were dissolved in chloroform or 1,2-dichlorobenzene (total concentration 5-50 mg/ml solvent) by stirring over night at elevated temperature. Solutions were spin-coated onto PEDOT:PSS coated ITO patterned glass substrates at spin speeds between 500 and 4000 rpm for 1 minute. Best results and control of device thickness were found when using intermediate concentrations (20-30 mg/ml solvent), and varying the spin speed to control thickness. Immediately following spin-coating the devices were placed in a covered Petri dish to allow a slow dry.

The resultant structures of both transistor and solar cell polymer deposition are

shown in Figure 4.4. The solar cell structure includes the thermally evaporated capping metal cathode layer discussed in section 4.1.2.

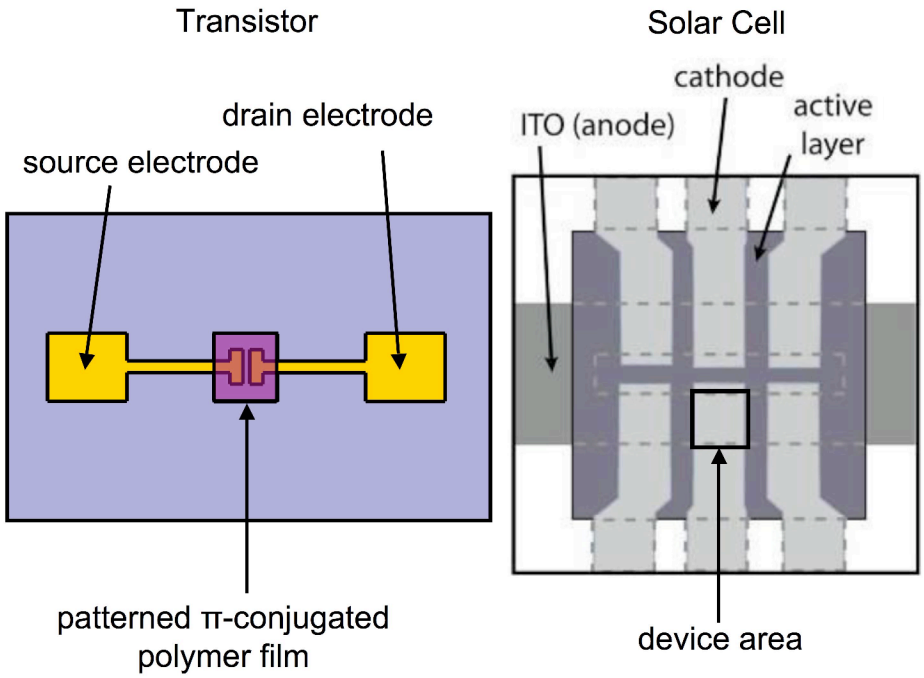


**Figure 4.4** Schematic of π-conjugated thin film transistor and photovoltaic devices.

## *4.2 Optical Characterization*

UV-vis optical absorption spectroscopy was carried out to access the breadth of absorption, extract the optical band gap, and estimate the peak absorption coefficient. Spectra of polymer thin films spin-coated on glass were collected with a Spectronic Genesys 5 spectrometer over a wavelength range of 300–1000 nm. The optical band gap ($E_g^{opt}$) was extracted by by converting the onset absorption ($\lambda_{onset}$) to energy ($E_g^{opt} = 1240/\lambda_{onset}$). The peak absorption coefficient was found by collecting UV-vis spectra of several films of varying thickness, and plotting the peak absorption against film thickness. From a linear fit of the data, the extracted slope represents the absorption

coefficient.

### *4.3 Thermal Characterization*

Thermal analysis using differential scanning calorimetry (DSC) was used to extract polymer glass transition, melting, and crystallization temperatures. Additionally, DSC was used to access polymer fullerene phase behavior. DSC heating and cooling curves were collected using a TA Instruments Q1000 calibrated with indium. Curves were collected at a temperature ramp rate of 10°C with the second heating and cooling sweeps used for transition assignments. Glass transitions were defined as sigmoidal features in the second heating. Positive and negative peaks were assigned as melting and crystallization transitions respectively.

### *4.4 Film Thickness Characterization*

Evaporated metal layer thickness was monitored using quartz crystal microbalance (QCM). However, it was desired to confirm QCM thicknesses and measure spin-coated layer thicknesses. Additionally, film thickness measurements were necessary to estimate optical absorption coefficients and electrochemical charge densities. Thicknesses were measured with profilometery (KLA-Tencor). Metal films were measured at step edges, and polymer films were scratched and measured at the scratch. Care was taken to use small force loadings on soft polymer films to obtain accurate measurements.

### *4.5 Field Effect Transistor Testing*

Field effect transistors were used as test beds to quantify the charge transport behavior of various π-conjugated polymers. Transistors were tested in Desert Cryogenics vacuum probe station at room temperature housed within a $N_2$ glove box. Output and

transfer curves were collected with Keithly 236, 237, and 6517A source meters controlled by customized LabView code. Gate contact was made to the back of the doped wafer substrate. In order to achieve ohmic contact to the gate electrode the back of the substrate was scored with a scribe and coated with silver paste. Source and drain contact was made with tungsten probe tips.

## *4.6 Electrochemical Characterization*

Electrochemical characterization of π-conjugated polymers was carried out to determine the energetic position of the frontier molecular orbitals, the distribution of electrochemical density of state, measure *in situ* the electrical conductivity. The *in situ* conductivity measurements were analogous to the current-voltage characterization of an electrochemical transistor.

### *4.6.1 Cyclic Voltammetry*

The position of the highest occupied molecular orbitals (HOMO) and the density of electrochemical states were collected using cyclic voltammetry. Voltammograms were recorded in ionic liquid supporting electrolytes at a scan rate of 50-100 mV/sec. The working electrode consisted of a gold-coated glass slide spin-coated with the π-conjugated polymer being investigated. The working electrode area was defined by a o-ring connecting the substrate to a custom Teflon liquid cell. The counter electrode and reference electrode consisted of platinum mesh and silver wire respectively. Cyclic voltammograms measured using a Pine AFRDE5 bipotentiosat with an analog-to-digital converter (LabJack) to log the data. The cells were assembled and tested in an inert atmosphere glovebox. HOMO levels were estimated from the oxidation onset relative to

cobaltocene using the equation: $E_{HOMO} = -q(E_{ox,\ onset\ vs.\ Cc\ o/+} + 3.75)$. Integrated cyclic voltammograms of polymer films with known thickness provided the electrochemically induced volumetric charge density.

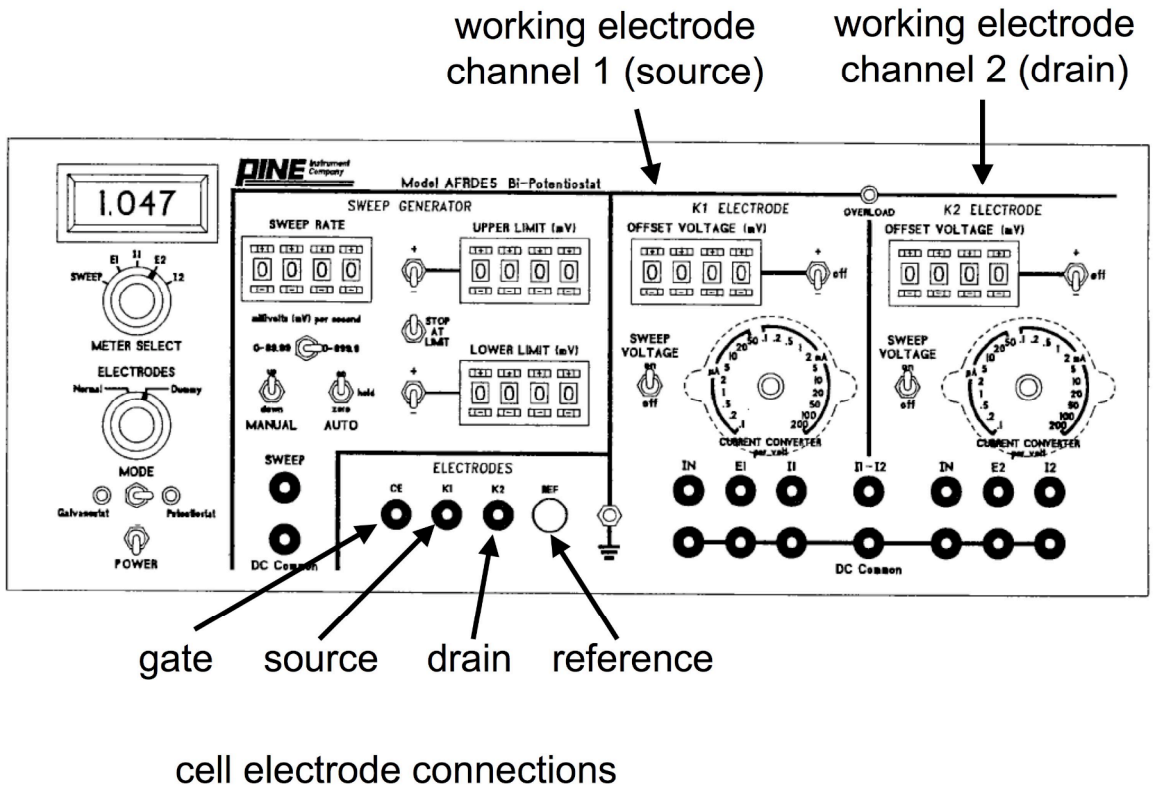


**Figure 4.5** Front panel schematic of the Pine bipotentiostat illustrating the connection scheme for carrying out cyclic voltammetry with a *in situ* conductivity measurement (*i.e.* electrochemical transistor characterization).

### *4.6.2 In Situ Conductivity*

Conductivity measurements were carried out using a working electrode where the gold layer was "split" using a wire shadow mask during metal electrode deposition, creating a source and drain electrode. The continuous polymer film created a transistor channel in the region between the two electrodes. The source and drain electrodes where

biased by connecting each to an individual working electrode channel on the bipotentiostat and offsetting the drain by 10-100 mV. The source-drain potential offset was chosen such that either the charging or conduction current was large with respect to the other. The smaller of the two currents was determined by subtracting the source current from the drain current. Room and variable temperature cyclic voltammograms with *in situ* conductivity measurements were carried out with the cell in a Desert Cryogenics vacuum probe station with a temperature-controlled stage.

## *4.7 Photovoltaic Cell Testing*

In order to access the performance of π-conjugated polymer in photovoltaic devices laboratory test cells were measured under simulated solar illumination. Solar cell current-voltage characteristics were collected using an Agilent 4155C Semiconductor Parameter Analyzer, under dark conditions and simulated solar illumination using a 150 W Xe-arc lamp (Oriel) with an AM 1.5 G filter, attenuated to 100 mW/cm$^2$. Lamp power was calibrated using a broadband Newport thermopile. Contact to the solar cell anode and cathode was accomplished with tungsten probe tips. Ohmic contacts between the tungsten probe tips and the device contact pads were acheived by coating the electrode contact pads with silver paste prior to testing. Current-voltage sweeps were collected from -1 V to +2. All measurements were carried out in air.

# *5. Energy Level Tuning Through Control of Conjugated Co-polymer Composition*[*†]

## *5.1 Overview*

Systematic synthetic tunability of conjugated polymer optical and electronic properties is highly desirable, especially for photovoltaic applications. To accomplish this, one divinyl and three dipropenyl monomers were prepared for ruthenium-catalyzed acyclic diene metathesis (ADMET) polymerization. Homopolymerization afforded three poly(thienylene vinylene)s (PTVs) and a poly(fluorene vinylene) (PFV) with distinct chemical structure and optoelectronic properties. Binary combinations of the thiophene based monomers over a range of compositions gave three series of copolymer samples with tunable HOMO levels and band gaps. The utility of this method was further demonstrated by the preparation of a stoichiometric terpolymer. A binary combination of fluorene and thiophene containing monomers gave a series of copolymer samples, which maximized HOMO level depth and minimized band gap. Polymers were characterized with $^{1}$H NMR spectroscopy, size-exclusion chromatography, ultraviolet-visible spectroscopy, cyclic voltammetry, and field effect transistors. This copolymerization approach effectively demonstrates the ability of ADMET polymerization to prepare

[*]Adapted with permission from "Band Gap and HOMO Level Control in Poly(thienylene vinylene)s Prepared by ADMET Polymerization" Joshua C. Speros, Bryan D. Paulsen, Bradley S. Slowinski, C. Daniel Frisbie, and Marc A. Hillmyer, *ACS Macro Lett., 2012, 1, pp 986–990* Copyright 2012 American Chemical Society.

[†]Work carried out in conjunction with J. C. Speros, who synthesized copolymers, and carried out all NMR, SEC, and mass spectrometry characterization.

conjugated copolymers with tuned optoelectronic properties that span a broad composition window.

## *5.2 Introduction*

The ability to tune the properties of conjugated polymers (CPs) through chemical modification has allowed for their integration in sensors,[74] organic light-emitting diodes,[75] field-effect transistors,[76] and organic photovoltaics (OPVs).[77] OPVs are of particular interest because cost-effective solution processing techniques can be used for their preparation. State-of-the-art OPV power conversion efficiencies now lie in the 7–9% range[78–81] as a result of both device optimization and the development of low band gap CPs typically having a perfectly alternating sequence of donor and acceptor (D-A) monomeric units.[82] Low band gap CPs are desirable because they often afford efficient and broad absorption of the solar spectrum. Systematic tuning of the band gap in a homologous set of CP materials can be ideally used to optimize OPV performance. However, such tunability can be synthetically difficult to achieve in conventional D-A polymers. Here we describe an approach to tunable energy levels based on copolymerization of structurally and electronically distinct monomers.

Few researchers have explored statistical copolymerization methods for the preparation of CPs. Unlike the alternating D-A approach,[83] a primary advantage of this strategy is the ability to probe non-stoichiometric monomer combinations instead of the 1:1 composition imposed by an alternating architecture. Some of the earliest examples of random CPs were aimed at tuning photoluminescence properties and were prepared by Yamamoto coupling of various dibromo monomers.[84,85] However, a broad composition

range was not studied. More recent examples of random CPs make use of palladium-catalyzed Suzuki and Stille coupling strategies.[86,87] These routes require lengthy syntheses of, for example, one diboronic ester/ditin monomer and two dibromo monomers. Additionally, given the alternating nature of these polymerizations only half of the composition window is accessible. Recently, Thompson and coworkers built on the utility of this approach by demonstrating "semi-random" CPs using 2-bromo-5-trimethyltin-3-hexylthiophene, 2,5-bis(trimethyltin)-thiophene, and 4,7-dibromo-2,1,3-benzothiadiazole or dibromo-bisthiophene-diketopyrrolopyrrole monomers and Stille coupling conditions.[88,89] They demonstrated that a small percentage of acceptor moiety in the copolymer backbone had a significant impact on the optoelectronic properties. More recently, this group expanded their Stille coupling approach to "semi-random" CPs by demonstrating control of open-circuit voltage[90] and optimization of OPV efficiency.[91] Inspired by this approach, we sought a methodology that would tolerate a wide variety of functionality, only require two monomers, and avoid the use of tin-containing monomers.

## *5.3 Experimental Methods*

### *5.3.1 Materials and General Methods*

C16 and C16-PTV were prepared according to previous work.[74] Commercially available solvents and reagents were purchased and used as received from Aldrich and Acros. Degassed THF was purified by passage through an activated alumina column and collected in flame-dried, air-free flasks. N,N,N',N'-tetramethylethylenediamine (TMEDA) was dried over molecular sieves and distilled under vacuum from n-butyllithium. All reactions were run under argon or vacuum using standard Schlenk

techniques. $^{1}H$ and $^{13}C$ NMR spectra were acquired on either a Varian INOVA 500 or 300 MHz spectrometer. Spectra were referenced internally to tetramethylsilane ($^{1}H$) or to residual solvent peaks ($^{13}C$). High resolution mass spectrometry was performed on a Finnigan MAT 95 mass spectrometer operating in EI (electron impact) mode. Samples were introduced using a solid probe. Size exclusion chromatography (SEC) analysis was performed in $CHCl_3$ (1 mL/min, 35 °C) using a Hewlett Packard (Agilent Technologies) 1100 Series liquid chromatograph equipped with three PlGel 5 μm Mixed-C (Polymer Laboratories) columns with pore sizes of 500, $1\times10^3$, and $1\times10^4$ Å. The columns were calibrated using polystyrene standards (Polymer Laboratories), and the refractive index signal was recorded with a Hewlett Packard 1047A refractive index detector. Ultraviolet-visible (UV-Vis) absorption spectra for polymer solutions and thin films were acquired on a Spectronic Genesys 5 spectrometer over a wavelength range of 300–1000 nm. The solution ($CHCl_3$) spectra were obtained in a 1 cm quartz cuvette, and the film spectra were obtained by spin casting a $CHCl_3$ solution (10 mg/mL, 1500 rpm, 40 s) on a glass substrate. Elemental analysis was performed by Atlantic Microlab Inc. in Norcross, GA using combustion coupled with thermal conductivity detection.

### *5.3.2 Electrochemical and Electrical Characterization*

Electrochemical measurements were carried out in a ~1 ml Teflon cell with a Pt mesh counter electrode and Ag wire quasi-reference electrode. Assembled cells had a defined working electrode area of 0.709 $cm^2$. Cyclic voltammagrams (CV) of the polymer coated Au working electrodes were measured using a Pine AFRDE5 bipotentiosat with an analog-to-digital converter (LabJack) to record data. The cells were assembled and tested in an inert atmosphere glovebox. The ionic liquid 1-butyl-1-

methylpyrrolidinium bis(trifluoromethylsulfonyl)imide ([P14][TFSI]), purchased from EMD Chemicals (Gibbstown, NJ), was used as received as the electrolyte medium. Following each polymer film measurement, the quasi reference electrode was calibrated through the addition, and measured reduction potential, of cobaltocenium hexafluorophosphate ($CcPF_6$), purchased from Sigma-Aldrich (St. Louis, MO). HOMO levels were estimated from the oxidation onset relative to cobaltocene using the equation: $E_{HOMO} = -q(E_{ox,\ onset\ vs.\ Cc\ o/+} + 3.75)$.

Bottom gate bottom contact geometry transistors were fabricated on doped Si wafers with 3000 Å of thermally grown oxide. Gold source-drain contacts, *ca.* 250 Å as measured by profilometry and quartz crystal microbalance, were deposited via electron beam evaporation (Temescal) of a 25 Å chromium adhesion layer and 225 Å of gold, and patterned via the lift-off technique. Substrates were cleaned with successive acetone, methanol, and isopropyl alcohol sonications followed by an $UV/O_3$ exposure. In a $N_2$ glove box, cleaned substrates were surface treated with OTS, octadecyltrichlorosilane, by spin-coating from hexanes at 4000 rpm for 1 minute. Immediately following, polymer active layers were spin-coated from 10 mg/ml chloroform or 1,2-dichlorobenzene solutions at 2000 rpm, and baked on a hot plate at 105 °C for 10 minutes to drive off residual solvent. Transistors were tested in Desert Cryogenics vacuum probe station at room temperature housed within a $N_2$ glove box. Output and transfer curves were collected with Keithly 236, 237, and 6517A source meters controlled by customized LabView code.

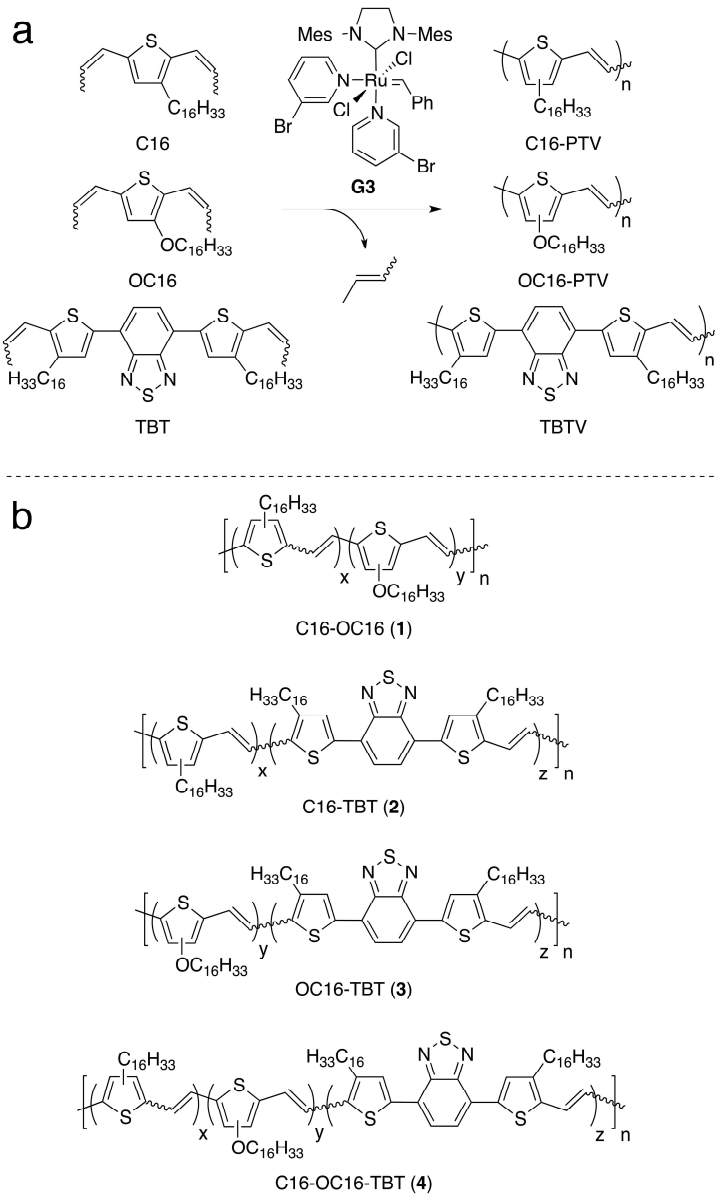


**Figure 5.1** (a) Homopolymer synthesis by ADMET (b) and copolymer structures.

## *5.4 Results and Discussion*

### *5.4.1 Synthesis and Characterization*

Acyclic diene metathesis (ADMET) polymerization is a step-growth polymerization that typically links α,ω-dienes to generate linear polymers with

unsaturated repeat units.[92] ADMET polymerization has been used to prepare polymers for diverse applications.[93] In the CP arena, poly(acetylenes),[94] poly(phenylene vinylenes),[95] poly(fluorene vinylenes),[96] poly(carbazole vinylenes),[97] and poly(thienylene vinylenes)[98,99] (PTVs) have all been prepared by ADMET polymerization. This polymerization technique has also been used to prepare statistical non-conjugated copolymers.[100,101]

We synthesized three monomers, 2,5-dipropenyl-3-hexadecylthiophene (C16), 2,5-dipropenyl-3-hexadecyloxythiophene (OC16), and 4,7-Bis(5-propenyl-4-hexadecyl-2-thienyl)-2,1,3-benzothiadiazole (TBT), all sharing the same reactive propenyl functionality (Figure 5.1a). The respective low band gap homopolymers and a broad range of copolymers were synthesized by ADMET polymerization. All polymers were prepared using a highly active 3-bromopyridine functionalized ruthenium metathesis catalyst (G3).[102] For consistency the same hexadecyl solubilizing side chain was installed in all three monomers. Monomers were also designed to be electron rich (OC16) or electron poor (TBT) as compared to the "neutral" variant (C16).

The C16 monomer was prepared following a previous literature report[99] in 68% overall yield with a *Z*:*E* ratio of 83:17. The synthesis of OC16 began by treating 3-bromothiophene with the sodium alkoxide of 1-hexadecanol in the presence of copper iodide. Lithiation of the 3-hexadecyloxythiophene product with n-butyllithium followed by treatment with N,N'-dimethylformamide (DMF) and acidic workup afforded the dialdehyde. A salt-free Wittig reaction provided OC16 in 52% overall yield with a *Z*:*E* ratio of 65:35. Synthesis of the TBT monomer began with the Stille coupling of 4,7-

dibromo-2,1,3-benzothiadiazole and 2-tributylstannyl-4-hexadecylthiophene catalyzed by bis(triphenylphosphine) palladium (II) chloride. The product was treated with DMF and phosphorus oxychloride under Vilsmeier-Haack conditions to afford the dialdehyde.[103] The conversion of dialdehyde to TBT under salt-free Wittig conditions gave an overall yield of 16% and a *Z*:*E* ratio of 62:38 (see Supporting Information for synthetic details).

Homo- and copolymerization of C16, OC16, and TBT monomers was conducted under reduced pressure (20–50 mtorr) in anhydrous 1,2,4-trichlorobenzene with G3 (1 mol%). Polymerizations were allowed to proceed for 16–48 h before precipitation in a non-solvent (methanol or acetone) and purification by Soxhlet extraction with the same non-solvent. Relative number-average molecular weights were determined by size-exclusion chromatography (SEC) in chloroform versus polystyrene standards. $^1$H NMR spectroscopy was employed to characterize all polymers and to determine the average monomer composition in the copolymer structures. However, the NMR data was not useful with respect to sequence distribution determination.

The C16:OC16 ratios in isolated copolymers (**1a**–**i**) were quantified using $^1$H NMR spectroscopy and were within a few percent of the feed ratios in all cases (Table 5.1). The second copolymer series employed the C16 and TBT monomers (**2a**–**e**), and again the feed ratios closely matched the average copolymer compositions as determined by $^1$H NMR spectroscopy. All isolated polymers were of roughly the same apparent molar mass ($M_n$ ca. 6 kg/mol) and molar-mass dispersity allowing for direct comparison of optical behavior. Copolymers in this series could be monitored qualitatively by color change. The OC16 and TBT monomers were used in preparation of the third copolymer

series (**3a**–**c**), and average copolymer composition calculated using $^{1}$H NMR spectroscopy was very close to the feed ratios. To demonstrate the synthetic versatility of this copolymerization approach a terpolymer (**4**) was prepared by combining equimolar amounts of the three monomers. The terpolymer composition from $^{1}$H NMR spectroscopy was close to the feed ratio.

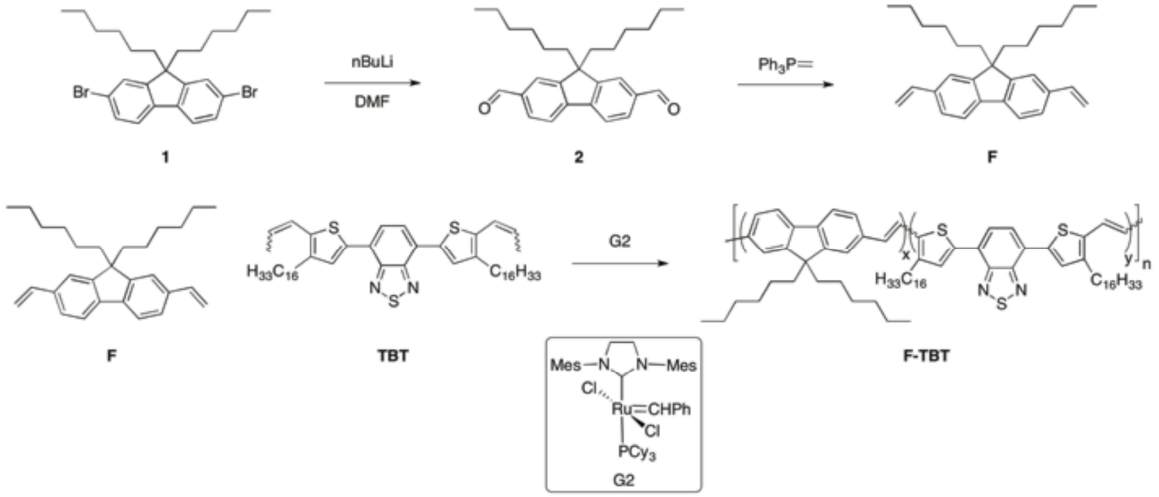


**Figure 5.2** Fluorenyl monomer (F) prepepara tion and ADMET synthesis of F-TBT copolymer.

Shown in figure 5.2, the synthesis of 2,7-divinyl-9,9-dihexyl-9H-fluorene (F) began by treating commercially available 2,7-dibromo-9,9-dihexyl-9H-fluorene with n-butyllithium in the presence of N,N,N',N'-tetramethylethylenediamine to generate the dilithiated species. This was reacted with N,N-dimethylformamide (DMF) and quenched with a mild HCl solution to generate 2,7-dicarbaldehyde-9,9-dihexyl-9H-fluorene. The dialdehyde was then reacted with a methylphosphorus ylide to generate F.

Copolymers of F and TBT were synthesized by first dissolving the monomers in 1,2,4-trichlorobenzene and adding the second generation Grubbs catalyst (G2). The polymerization was performed under vacuum to remove small molecule byproducts

(ethylene and 2-butene) and to drive the conversion of monomers to polymer. The copolymers (**5**) were isolated by precipitation in cold methanol and purified by soxhlet extraction. Copolymer molecular weight was determined by size-exclusion chromatography in chloroform versus polystyrene standards.

**Table 5.1** NMR, SEC, and UV–vis data for homo- and copolymers

| sample ID[a] | observed ratio[b] | $M_n$ (kg/mol)[c] | $D_M$[c] | $\lambda_{max,soln}$ (nm)[d] | $\lambda_{max,film}$ (nm)[e] | $E_g^{opt}$ (eV)[f] |
|---|---|---|---|---|---|---|
| C16-PTV | – | 33 | 2.2 | 582 (623) | 625 (677) | 1.66 |
| OC16-PTV | – | 4 | 1.6 | 634 | 676 | 1.49 |
| TBTV | – | 7 | 1.9 | 662 (422) | 683 (429) | 1.49 |
| C16-OC16 | C16:OC16 | | | | | |
| **1a** (90:10) | 89:11 | 34 | 2.8 | 591 (626) | 632 (682) | 1.64 |
| **1b** (80:20) | 80:20 | 14 | 1.9 | 593 (629) | 630 | 1.62 |
| **1c** (70:30) | 68:32 | 9 | 1.7 | 595 | 630 | 1.59 |
| **1d** (60:40) | 56:44 | 7 | 3.3 | 587 | 627 | 1.58 |
| **1e** (50:50) | 47:53 | 8 | 1.5 | 602 | 639 | 1.56 |
| **1f** (40:60) | 37:63 | 7 | 2.2 | 621 | 656 | 1.55 |
| **1g** (30:70) | 27:73 | 3 | 1.4 | 601 | 644 | 1.55 |
| **1h** (20:80) | 19:81 | 8 | 1.5 | 619 | 659 | 1.53 |
| **1i** (10:90) | 8:92 | 5 | 1.3 | 600 | 635 | 1.53 |
| C16-TBT | C16:TBT | | | | | |
| **2a** (95:5) | 95:5 | 10 | 1.7 | 580 (611) | 620 | 1.59 |
| **2b** (80:20) | 79:21 | 6 | 1.2 | 622 | 660 | 1.50 |
| **2c** (60:40) | 63:37 | 6 | 1.4 | 641 (435) | 678 (460) | 1.49 |
| **2d** (40:60) | 41:59 | 5 | 1.4 | 649 (433) | 680 (446) | 1.49 |
| **2e** (20:80) | 22:78 | 6 | 1.5 | 662 (430) | 686 (439) | 1.49 |
| OC16-TBT | OC16:TBT | | | | | |
| **3a** (75:25) | 78:22 | 3 | 1.1 | 638 | 686 | 1.46 |
| **3b** (50:50) | 55:45 | 4 | 1.2 | 640 (433) | 685 (452) | 1.46 |
| **3c** (25:75) | 23:77 | 4 | 1.2 | 645 (423) | 681 (437) | 1.48 |
| C16-OC16-TBT | C16:OC16:TBT | | | | | |
| **4** (1:1:1) | 0.36:0.34:0.30 | 4 | 1.2 | 624 (434) | 670 (440) | 1.49 |

[a]Values in parentheses are monomer feed ratios. [b]Determined by integration of appropriate resonances in $^1$H NMR spectra. [c]Determined by SEC in $CHCl_3$ versus polystyrene standards. [d]ca. $10^{-5}$ M in repeat unit in $CHCl_3$; values in parentheses are secondary peaks/shoulders. [e]Polymer film spin coated from $CHCl_3$ onto glass substrates; values in parentheses are secondary peaks/shoulders. [f]Determined from onset absorption of thin film ($E_g^{opt}$ = 1240 (nm eV)/$\lambda_{onset}$ (nm)).

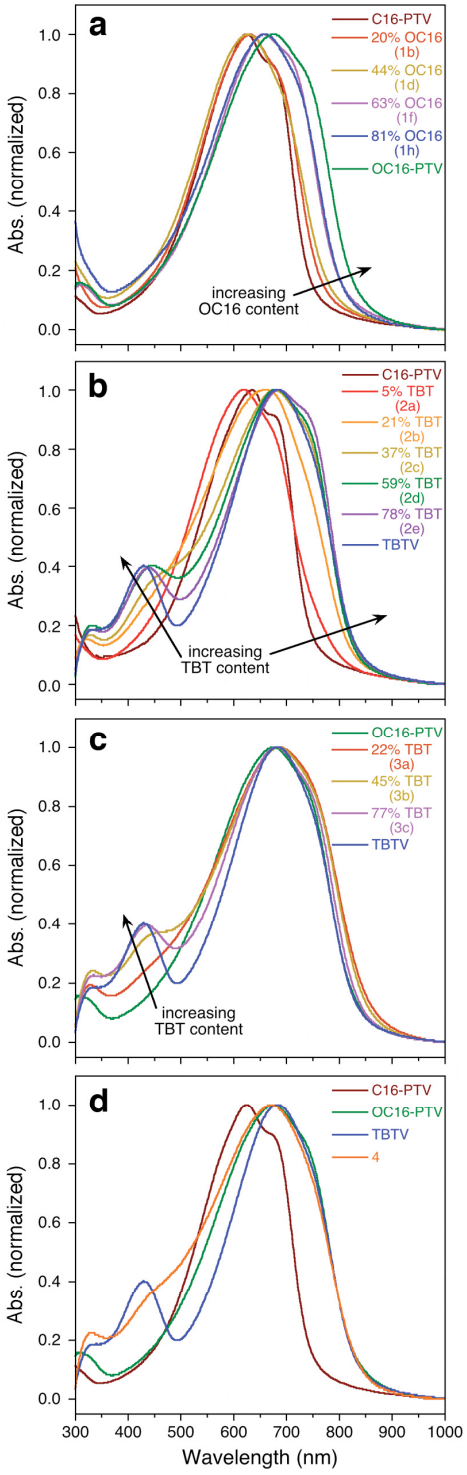


**Figure 5.3** UV–vis spectra of (a) C16-OC16 (**1**), (b) C16-TBT (**2**), (c) OC16-TBT (**3**), and (d) C16-OC16-TBT (**4**) as thin films on glass substrates. Corresponding homopolymers are shown in each series to highlight trends.

### *5.4.2 Thienyl Vinyl Donor Optical Characterization*

Optical behavior was analyzed in dilute chloroform solutions ($10^{-5}$ M in monomer repeat units) by ultraviolet-visible spectroscopy (UV–vis). Absorption maxima ($\lambda_{max}$) for C16-PTV, OC16-PTV, and TBTV homopolymers were 582, 634, and 662 nm, respectively. As observed previously, C16-PTV displayed a second $\lambda_{max}$ (623 nm) suggesting aggregation-induced vibronic fine structure.[99] TBTV also showed a second peak at 422 nm likely due to the π-π* transition; we attribute the peak at 662 nm to intramolecular charge transfer.[104] Thin film UV–vis spectra demonstrated predictable red shifts in absorption maxima as compared to solution spectra (Figure 5.3). Values of the optical band gaps ($E_g^{opt}$) were determined from the onset of absorption in the polymer thin film ($E_g^{opt} = 1240 / \lambda_{onset}$). C16-PTV was found to have an $E_g^{opt}$ of 1.66 eV, while both OC16-PTV and TBTV gave a value of 1.49 eV. All spectroscopic and chromatographic data are summarized in Table 5.1.

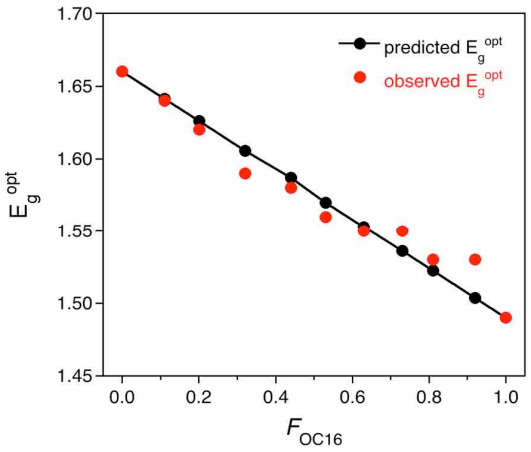


$$predicted\ E_g^{opt} = x_{C16}(1.66\ eV) + x_{OC16}(1.49\ eV)$$

**Figure 5.4** Predicted (see mixing equation) and measured (from thin film UV-Vis spectra) $E_g^{opt}$ of series **1** versus mole fraction (*F*) of OC16 in the copolymer.

The $\lambda_{onset}$ of C16-OC16, series **1**, thin films shifted to longer wavelengths (lower $E_g^{opt}$) as more OC16 was incorporated into the copolymer (Figure 5.3a). Although the molar mass range in this polymer series was large (3–34 kg/mol), this likely had minimal impact on $E_g^{opt}$, which in PTVs has been shown to saturate around ten repeat units.[105] Therefore, we posit that the observed differences in $E_g^{opt}$ are largely the result of copolymer composition. Figure 5.4 demonstrates the agreement between the predicted and actual $E_g^{opt}$ based on the sum of the mole fraction weighted values of the homopolymer bandgaps. Unlike series **1**, which showed a progressive shift in $E_g^{opt}$, the $E_g^{opt}$ of this series saturated upon addition of 20% TBT monomer. As suggested by Thompson and coworkers,[88,89,91] applying this "trace acceptor" concept to other CP systems may allow for significantly altered absorptive properties with minimal changes to the overall polymer composition. For series **3**, the π-π* transition from TBT proved a useful means of confirming the increase in TBT content (Figures 5.3c). Interestingly, the $E_g^{opt}$ of all three copolymers was slightly lower than that of the parent homopolymers. This is possibly the result of intramolecular charge transfer; the same phenomenon attributed to reduced band gap in D-A materials.[106] Terpolymer **4** exhibited a much broader absorption than the respective homopolymers in solution and as a thin film (Figure 5.3d) by UV–vis spectroscopy.

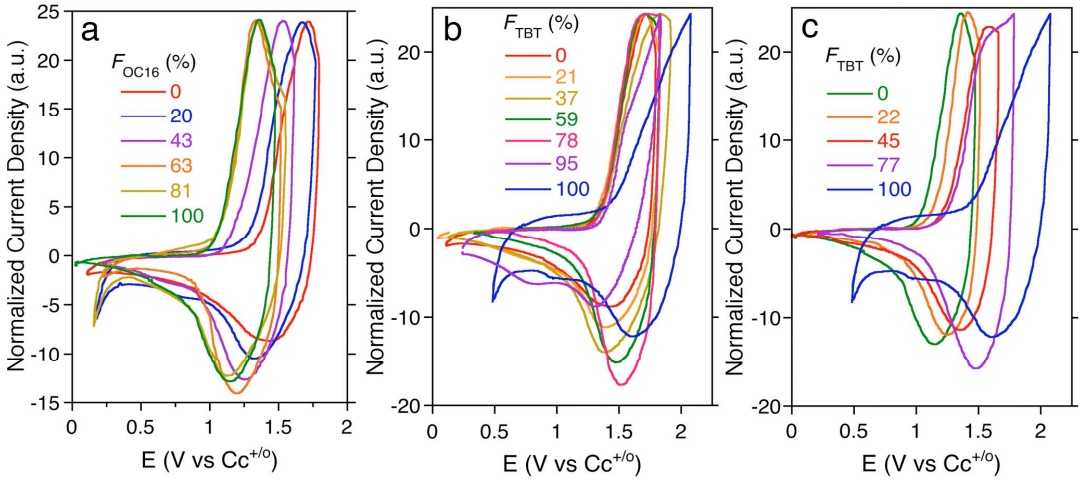


**Figure 5.5** Cyclic voltamograms of copolymer series (a) **1**, (b) **2**, and (c) **3** collected in [P14][TFSA] ionic liquid electrolyte at 50 mV/sec.

### *5.4.3 Thienyl Vinyl Donor Electrochemical Characterization and Energy Levels*

The homo- and copolymers were characterized by cyclic voltammetry (CV) to quantify the impact of copolymerization on the position of the highest occupied molecular orbital (HOMO). The room temperature ionic liquid 1-butyl-1-methylpyrrolidinium bis(trifluoromethylsulfonyl)imide ([P14][TFSA]) was employed as the electrolyte system as its broad window of electrochemical stability provided high sweep-to-sweep stability and sample-to-sample reproducibility.[107] The HOMO level of each polymer was calculated from the onset of electrochemical oxidation (Figure 5.5). The measured reference potentials for each sample were internally calibrated using the standard redox couple cobaltocenium hexafluorophosphate ($CcPF_6$) known to undergo a reversible reduction at -1350 mV vs the ferrocene redox couple in ionic liquids.[108,109]

In the case of series **1**, the incorporation of OC16 into C16 lead to the linear decrease in the potential of the onset of oxidation from 1.06 V vs $Cc^{+/o}$ for pure C16, to 1.37 V vs $Cc^{+/o}$ for pure OC16. The cyclic voltamograms of series **2** displayed a constant

oxidation onset consistent with that of pure C16 regardless of TBT content, excluding pure TBT which displayed on oxidation onset of 1.48 V vs $Cc^{+/o}$. Series **3** mirrored the behavior of series **1**, with the incorporation of OC16 into TBT lead to the linear decrease in the potential of the onset of oxidation from that of pure TBT to that of pure OC16

Taking the ferrocene oxidation potential to lie 5.1 eV below vacuum level,[110] the HOMO levels were calculated as $E_{HOMO} = -(E_{(onset,ox\ vs\ Cc+/o)} + 3.75)$ eV. The HOMO level positions of C16-PTV, OC16-PTV, and TBTV were -5.12, -4.81, and -5.23 eV, respectively. For reference, regioregular poly(3-hexylthiophene) measured in the same electrolyte system gave a HOMO level position of -5.06 eV.

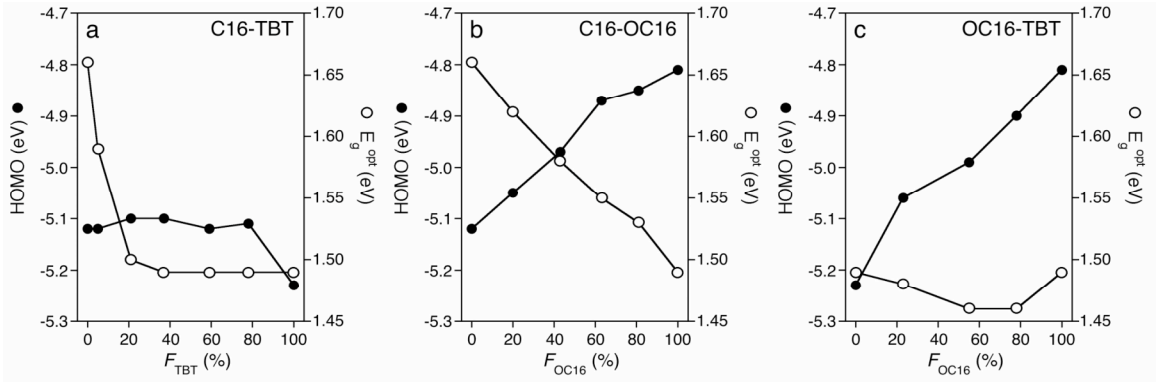


**Figure 5.6** HOMO level position from CV (filled circles) and $E_g^{opt}$ from UV–vis (open circles) versus copolymer composition (*F*) of (a) C16-TBT, (b) C16-OC16, and (c) OC16-TBT thin films.

Copolymers of C16-TBT demonstrated saturation behavior in both HOMO level and $E_g^{opt}$ (Figure 5.6a). Upon incorporation of 22% C16 into the TBTV polymer chain the HOMO level position was immediately pinned to that of the C16-PTV homopolymer (≈ –5.1 eV). On the other hand, the $E_g^{opt}$ saturated at the TBTV homopolymer value of ~1.5 eV at 21% TBT monomer incorporation. This behavior is consistent with the

generally accepted concept that the acceptor monomer (TBT) sets the LUMO level, and the donor monomer (C16) sets the HOMO level even at low levels of incorporation.[82,88]

Interestingly, the C16-OC16 and OC16-TBT copolymers did not follow the saturation behavior observed for C16-TBT. Instead, the HOMO level increased (310 meV range) and the $E_g^{opt}$ decreased (170 meV range) monotonically with increasing OC16 content in the C16-OC16 copolymers (Figure 5.6b). Likewise, the HOMO levels of OC16-TBT copolymers could be tuned over a 420 meV range (Figure 5.6c). However, despite the increase in HOMO level in the OC16-TBT copolymers, the $E_g^{opt}$ varied little as the respective homopolymers had identical band gaps.

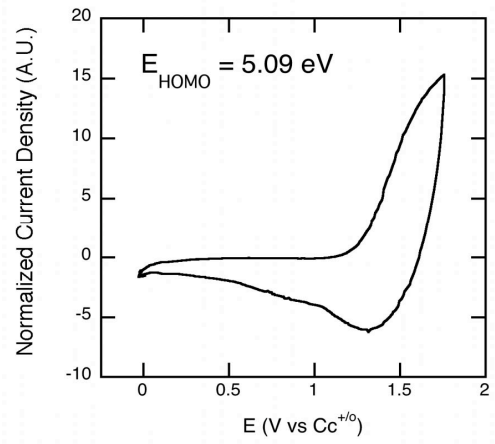


**Figure 5.7** Cyclic voltammogram of terpolymer, **4**, collected in [P14][TFSA] ionic liquid electrolyte at 50 mV/sec.

Finally, the HOMO level position of the terpolymer (**4**) (36% C16, 34% OC16, and 30 % TBT) was determined by CV (-5.09 eV, Figure 5.7) and was consistent with that of the copolymers containing approximately 36% OC16. The $E_g^{opt}$ (1.49 eV) was consistent with that of the copolymers containing approximately 30% TBT according to the relationships shown in Figure 5.6.

By adding the magnitude of the $E_g^{opt}$ of each sample to the electrochemically determined HOMO level position, the lowest occupied molecular orbital, LUMO, can be estimated. This allows energy diagrams to be created, shown in figure 5.8, with the common fullerene acceptor PCBM shown for reference. Aside from the C16-TBT series, the LUMO level appeared to move in conjunction with the HOMO level with variations in copolymer composition.

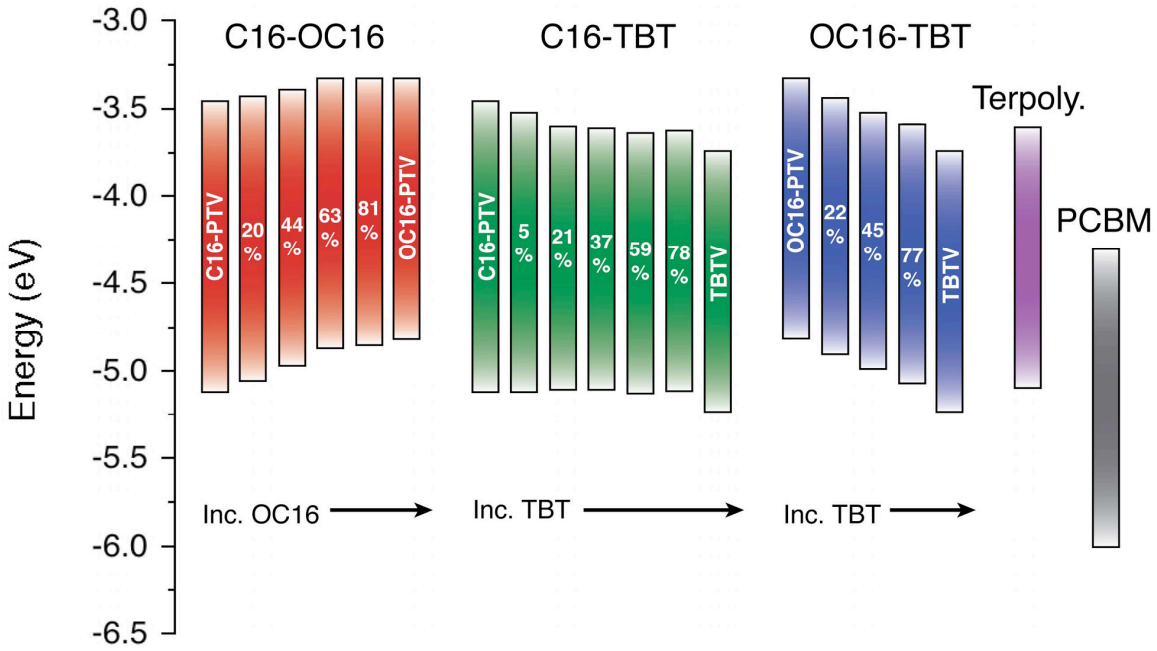


**Figure 5.8** Band diagram of C16-OC16 (red), C16-TBT (green), and OC16-TBT (blue) series. The terpolymer (purple) and PCBM (gray) are shown for completeness. LUMO levels were estimated from HOMO levels and $E_g^{opt}$ (LUMO = HOMO + $E_g^{opt}$).

The nonlinear behavior observed in C16-TBT copolymers is consistent with related phenomena in other D-A polymers, where the donor determines the HOMO level. However, this explanation does not adequately describe the monotonic behavior observed for the HOMO levels in the C16-OC16 and OC16-TBT copolymers. This is perhaps due

to the relatively large differences between HOMO levels of the corresponding homopolymers. As illustrated by Figure 5.8, we have shown that ADMET polymerization is an ideal means of generating CPs with precisely controlled optoelectronic properties and allows for systematic combination and optimization of various CP properties (e.g., HOMO/LUMO levels, band gap, photoluminescence, absorption strength, charge transport, etc.) with minimal synthetic effort. Specifically, in these thienylvinyl based systems a narrow band gap is readily achievable,[111] however the HOMO levels do not reach an adequate depth to achieve the highest expected performance. An idealized polymer for photovoltaic applications should have a $E_g^{opt}$ of 1.3-1.8 eV and a HOMO level position of 5.4-5.8 eV,[112] thus a donor providing a deeper HOMO is desired.

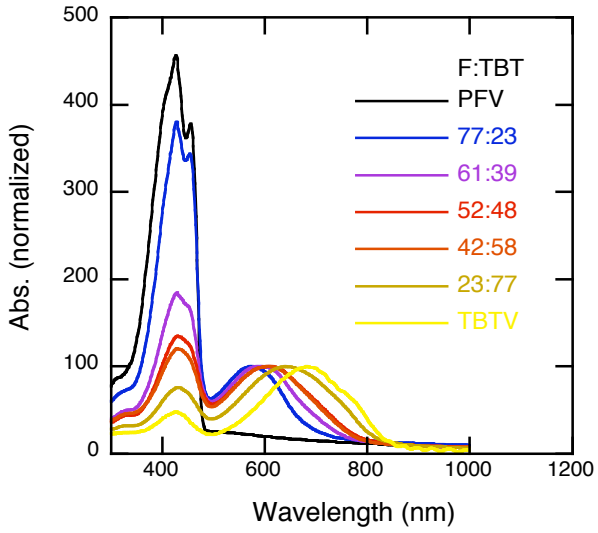


**Figure 5.9** Normalized UV-Vis absorption spectra of PFV, copolymer series **4**, and TBTV thin films.

### *5.4.4 Fluorenyl Vinyl Donor Optical Characterization*

To extend this synthetic tunability to random copolymer systems with deeper HOMO levels, fluorene (F) and benzathiadiazole (TBT) based vinyl and propenyl monomers were polymerized using the ADMET technique. Optical characterization of the F-TBT copolymer series (**4**) with UV-Vis absorption was carried out on spin-coated thin films, figure 5.9. Neat PFV homopolymer, polymerized from F, displayed a $\lambda_{max}$ of 427 nm, and like C16, second $\lambda_{max}$ of 457 nm due to order induced vibronic couplong. PFV displayed a $\lambda_{onset}$ of 479 nm, corresponding to a $E_g^{opt}$ of 2.59 eV. In series **4**, incorporation of TBT lead to a drastic decrease in $\lambda_{onset}$, and thus $E_g^{opt}$, with 20% monomer fraction of TBT resulting in an 800 meV reduction of $E_g^{opt}$. Additionally, TBT incorporation led to a suppression of the vibronic peak in the region of F absorption, as the F absorption became obscured by the TBT π-π* transition.

**Table 5.2** NMR, SEC, and UV–vis data for homo- and copolymers

| sample ID[a] | observed ratio[b] | $M_n$ (kg/mol)[c] | $D_M$[c] | $\lambda^1_{max,film}$ (nm)[d] | $\lambda^2_{max,film}$ (nm) | $E_g^{opt}$ (eV)[e] |
|---|---|---|---|---|---|---|
| PFV | – | 2.0 | 1.4 | 427(456) | – | 2.59 |
| TBTV | – | 6.9 | 1.9 | 430 | 682 | 1.49 |
| F-TBT | F:TBT | | | | | |
| **4a** (80:20) | 77:23 | 38.8 | 2.5 | 429(454) | 574 | 1.77 |
| **4b** (60:40) | 61:39 | 31.2 | 2.3 | 430(453) | 591 | 1.65 |
| **4c** (50:50) | 52:48 | 21.9 | 2.3 | 430 | 610 | 1.58 |
| **4d** (40:60) | 42:58 | 13.0 | 1.8 | 430 | 607 | 1.57 |
| **4e** (20:80) | 23:77 | 8.4 | 1.7 | 430 | 640 | 1.51 |

[a]Values in parentheses are monomer feed ratios. [b]Determined by integration of appropriate resonances in $^1$H NMR spectra. [c]Determined by SEC in $CHCl_3$ versus polystyrene standards. [d]Polymer film spin coated from $CHCl_3$ onto glass substrates; values in parentheses are secondary peaks/shoulders. [e]Determined from onset absorption of thin film ($E_g^{opt}$ = 1240 (nm eV)/$\lambda_{onset}$ (nm)).

Excluding PFV, TBTV and all the series **4** copolymers were of sufficient molecular weight that there conjugation lengths were likely not limited by the polymer chain length, and thus there $E_g^{opt}$ were assumed saturated.[105] Despite its low molecular weight, the PFV $E_g^{opt}$ was similar to other vinyl incorporating polyfluorenes,[113,114] and likely would not decrease significantly if higher molecular weights were achieved.

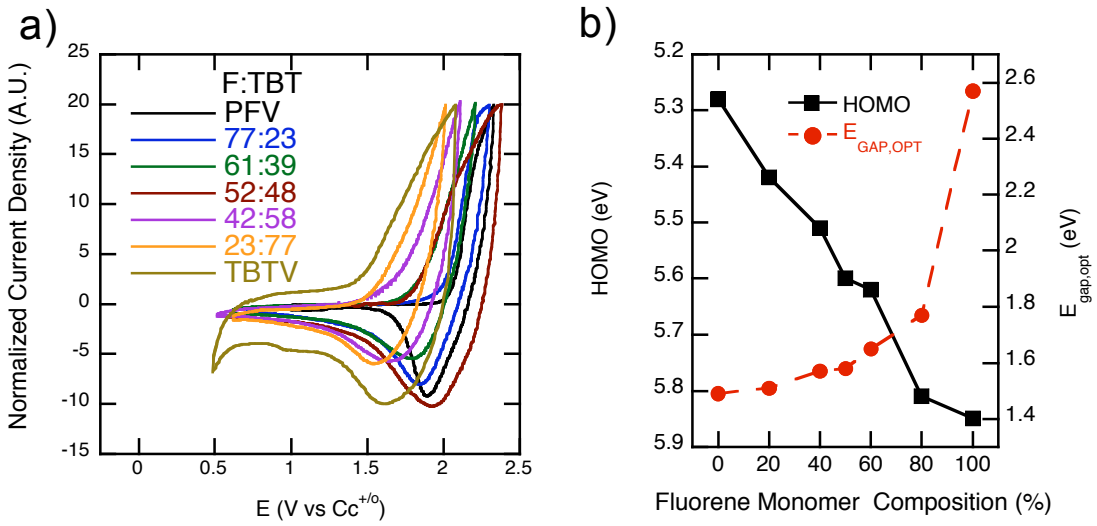


**Figure 5.10** (a) Cyclic voltammograms of PFV, series **4**, and TBTV thin films collected in [P14][TFSA] ionic liquid electrolyte at 50 mV/s. (b) HOMO level position and optical band gap of PFV, series **4**, and TBTV thin films.

### *5.4.5 Fluorenyl Vinyl Donor Electrochemical Characterization and Energy Levels*

When examined with cyclic voltammetry, PFV displayed a large positive onset of oxidation at 2.10 V vs $Cc^{+/o}$. In F-TBT copolymers, the onset of oxidation decreased roughly linearily with increasing TBT content, figure 5.10a. By varying the relative F and TBT fractions, series **4** allowed the decrease of oxidation onset from 2.10 to 1.48 V vs $Cc^{+/o}$. Converting oxidation onsets to energy level positions on the vacuum scale, the HOMO position was tuned from 5.28 to 5.85 eV, a range of nearly 0.6 eV. Adding the

$E_g^{opt}$ to the HOMO level, the LUMO levels were estimated and energy diagrams constructed, figure 5.11. Whereas in series **1** and **3** the HOMO and LUMO levels both shifted roughly equally, in series **4** any TBT incorporation resulted in roughly constant LUMO, within ±100 meV, with only the HOMO systematically varying. This is the inverse of series **2** where C16 incorporation pinned the HOMO level, and the LUMO level varied with composition. All the copolymers in series **4** displayed $E_g^{opt}$ and HOMO level positions in the ideal range making them good potential candidates for high performance polymer-fullerene bulk heterojunction solar cells.

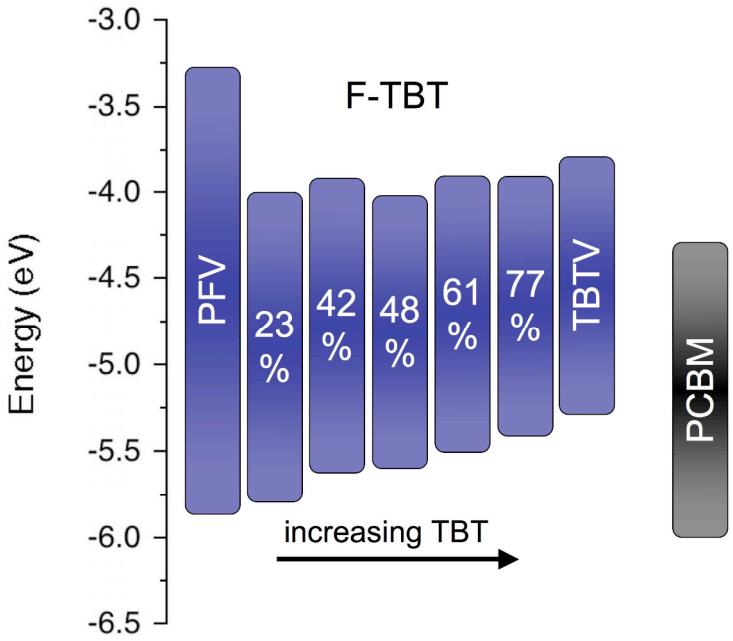


**Figure 5.11** Energy level diagram of PFV, copolymer series **4**, TBTV, and PCBM for reference.

### *5.4.6 Fluorenyl Vinyl Donor Hole Transport Properties*

Extending beyond the characterization of copolymer energy levels, transistors were made of the series **4** samples to investigate the effects of tuned energy levels on hole

transport. Bottom gate, bottom contact devices were fabrication with an OTS monolayer treated silicon dioxide gate dielectric. Transfer and output curves were collected for each sample, with the hole mobility, $\mu_h$, and threshold voltage, $V_t$, extracted from the saturation regime of transistor operation. Decent device performance was observed, with $\mu_h$ varying from ~$10^{-4}$ to ~$10^{-3}$ $cm^{-2}$ $V^{-1}$ $s^{-1}$, and $V_t$ varying from ~50 down to ~5 V, figure 5.12. Unexpectedly, the extracted $\mu_h$ varied non-monotonically with copolymer composition, displaying local maxima in field effect mobility at 39 and 77% TBT monomer, but with no copolymer sample exceeding the hole mobility of neat PFV. To confirm these results, multiple trials of multiple devices were carried out for each copolymer sample, with the statistically accuracy reflected in the error bars in figure 5.12.

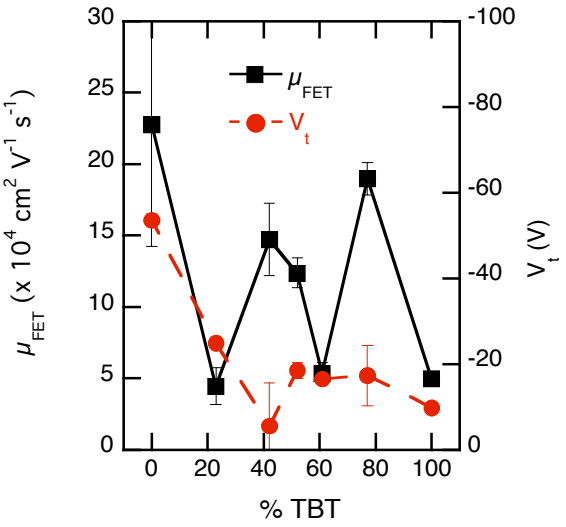


**Figure 5.12** Extracted field effect hole mobility and threshold voltage of copolymer series **4**, PFV (0%), and TBTV (100%) transistors.

While a common result is increased carrier mobility with increased polymer molecular weight, this system showed no correlation with molecular weight, table 5.2. In fact, the highest molecular weight sample yielded the lowest $\mu_h$, while the lowest

molecular weight yielded the highest $\mu_h$. Clearly there are structural and energetic factors that in this case trumped chain length. Despite the low molecular weight of neat PFV, the thin film UV-Vis displayed very strong vibronic structure common in highly ordered high mobility polymers.[99] Therefore, the decent measured device parameters were not unanticipated. Surprising was the existence of local hole mobility maxima to either side of a 50:50 donor to acceptor monomer composition. The enhancement of charge transport in asymmetric donor-acceptor ratios has significant implications in a field where copolymer donor-acceptor compositions besides 50:50 are not often studied.

The $V_t$ trend was somewhat more straightforward; with $V_t$ generally decreasing as the HOMO level becomes shallower. This reflects the reduction in energy barrier to charge injection and extraction from the source-drain electrodes. These hole transport studies reveal a complicated interplay between molecular orbital energy level position, molecular weight, inter-chain structure, and donor-acceptor character at work.

## *5.5 Conclusion*

Having characterized the energy levels and band gaps of four series of ADMET synthesized statistical copolymers, it has become apparent that statistical copolymerization is a powerful tool to tune the optical and energetic properties of conjugated polymers. This is especially pertinent to photovoltaic applications were a specific combination of band gap and energy level position is desired. The efficacy of this method has been demonstrated by the systematic variation of band gap and HOMO level position by over 1 eV, and LUMO level position by 700 meV. Additionally, we have shown that the combination of donor and acceptor monomers produced energy

levels that followed a variety of mixing rules, including straightforward linear combination, HOMO level pinning, and LUMO level pinning. Investigating charge transport in the copolymers showing ideal band gaps and HOMO level positions, it became clear that energy levels are just one of several factors dictating charge transport. The requisite next steps are to incorporate into photovoltaic devices and test the copolymers displaying idealized band gaps and HOMO level positions, specifically the F-TBT series, to directly relate the tunability of polymer energy levels with the tunability of photovoltaic decide performance.

# *6. Dependence of Conductivity on Charge Density and Electrochemical Potential in Polymer Semiconductors Gated with Ionic Liquids*[*]

## *6.1 Overview*

We report the hole transport properties of semiconducting polymers in contact with ionic liquids as a function of electrochemical potential and charge carrier density. The conductivities of four different polymer semiconductors including the benchmark material poly(3-hexylthiophene) (P3HT) were controlled by electrochemical gating (doping) in a transistor geometry. Use of ionic liquid electrolytes in these experiments allows high carrier densities of order $10^{21}$ $cm^{-3}$ to be obtained in the polymer semiconductors and also facilitates variable temperature transport measurements. Importantly, all four polymers displayed a non-monotonic dependence of the conductivity on carrier concentration. For example, for P3HT in contact with the ionic liquid 1-ethyl-3-methylimidazolium tris(pentafluoroethyl)trifluorophosphate ([EMI][FAP]), the hole conductivity reached a maximum of 85 S/cm at 6 x $10^{20}$ holes $cm^{-3}$ or 0.16 holes per thiophene ring. Further increases in charge density up to 0.35 holes per ring produced a reversible drop in film conductivity. The reversible decrease in conductivity is due to a carrier density dependent hole mobility, which reaches 0.80 ± 0.08 $cm^2$ $V^{-1}$ $s^{-1}$ near the conductivity peak. The conductivity behavior was qualitatively

[*]Adapted with permission from "Dependence of Conductivity on Charge Density and Electrochemical Potential in Polymer Semiconductors Gated with Ionic Liquids" Bryan D. Paulsen and C. Daniel Frisbie, *J. Phys. Chem. C, 2012, 116 (4), pp 3132–3141* Copyright 2012 American Chemical Society.

independent of the type of ionic liquid in contact with the polymer semiconductor though there were quantitative differences in the current versus gate voltage characteristics. Temperature dependent measurements of the mobility in P3HT revealed that it is activated over the range 250-350 K. Both the pre-exponential coefficient $\mu_0$ and the activation energy $E_A$ depend non-monotonically on carrier density with $E_A$ becoming as small as 20 meV at the conductivity peak. Overall, the peak in conductivity versus carrier density appears to be a general result for polymer semiconductors gated with ionic liquids.

## *6.2 Introduction*

Understanding electrical transport mechanisms in polymer semiconductors is an ongoing challenge with several potential benefits including the discovery of new transport phenomena and the design of materials with better performance in electronic devices. It is well known that highly doped conjugated polymers can exhibit metal-like conductivities as high as $10^4$ S/cm,[115,116] but detailed understanding of the temperature dependence of transport and the nature of the charge carriers in these systems is still lacking. It is also generally understood that both conductivity and carrier mobility increase with carrier concentration in these materials.[117,118] Conductivity is naturally expected to be proportional to carrier concentration and likewise mobility also often increases with carrier concentration because of trap filling. However, it is also possible to "over-charge" polymer semiconductors such that their conductivity decreases with increasing carrier concentration. This behavior was shown elegantly in electrochemical doping experiments of Wrighton and colleagues in the 1980s and early 1990s,[119,120] and in

particular in a 1990 publication.[121] In these experiments, conjugated polymers were incorporated into microelectrochemical transistors; gating of the polymer semiconductor in contact with electrolyte allowed reversible charging and discharging of the polymer film and simultaneous measurement of conductivity. It was shown that conductivity versus gate voltage exhibited a peak. The gate voltage is directly proportional to charge density and thus it was clear that beyond some optimum charge concentration the conductivity of the polymer decreased with increasing carrier density. This effect is also referred to as negative transconductance because the slope of the drain current versus gate voltage characteristic, $dI_D/dV_G$, of the transistor is negative.

This basic result has been reproduced by other research groups.[122,123,124,125,126,127,128] The effect is not a chemical or electrochemical degradation as the conductivity versus gate voltage behavior is entirely reversible. A possible explanation for the behavior may be band filling, i.e., at very high states of charge the HOMO band of the material is essentially full of holes and there is not an adequate number of empty states to hop to.[121,129] Others have proposed that bipolaron formation at high carrier densities leads to self-trapping of charge and a decrease in conductivity.[130]

In this paper, we describe an investigation of conductivity in four benchmark polymer semiconductors that are electrochemically gated with ionic liquids. For these experiments, we employ a microelectrochemical transistor geometry similar to the Wrighton experiment. The key difference is that we use ionic liquids as the electrolyte instead of more conventional solvent-based electrolytes. Ionic liquids offer important advantages.[131] First, like more conventional electrolytes, they have wide electrochemical

stability windows that facilitate very large charge accumulations in excess of $10^{21}$ $cm^{-3}$. Second, ionic liquids have extremely low vapor pressures making them compatible with cryogenic vacuum probe stations, and thereby facilitate variable temperature transport measurements. Third, it is straightforward to carry out the gating experiments with different ionic liquids (many are available) so that the role of the ionic liquid in the measured transport characteristics can be assessed.

Using ionic liquid gates, we observe the same peak in conductivity versus gate voltage behavior reported previously,[121] thus verifying the generality of this effect in several different polymer semiconductors and simultaneously demonstrating the utility of ionic liquids for observing this phenomenon. In addition, we exploit the fact that the referenced electrochemical potential is convertible to the absolute energy scale versus the vacuum level. By recording the gate displacement (charging) currents as a function of potential (essentially the cyclic voltammogram of the polymer) we are able to estimate the density of electronic states for the electrochemically doped polymer semiconductor. Finally, we have measured the mobility as a function of carrier density and temperature. The activation energy for the mobility shows a clear minimum versus carrier density, i.e., it increases beyond the carrier concentration corresponding to the conductivity peak. To our knowledge, this is the first report of temperature dependent carrier mobility measurements of polymer semiconductors in the high carrier density, negative transconductance regime.

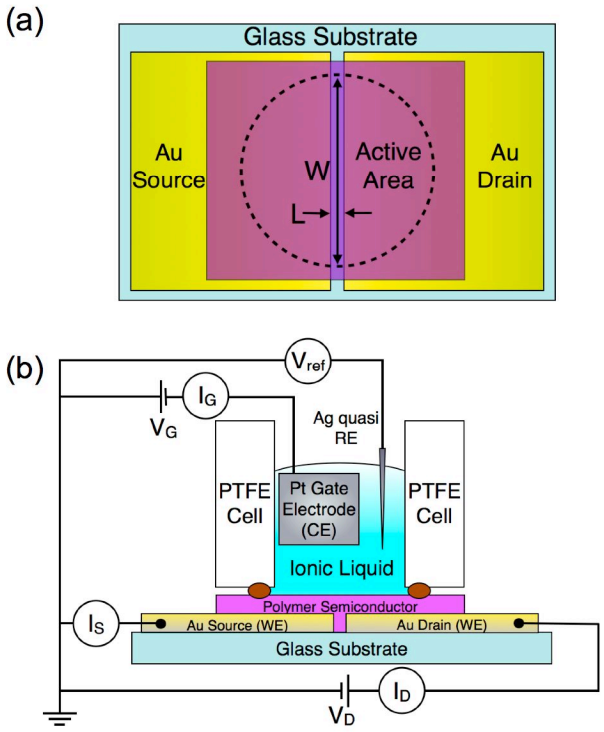


**Figure 6.1** (a) Top view of the microelectrochemical transistor and (b) cross-section of the device and electrochemical cell.

## *6.3 Experimental Methods*

### *6.3.1 Materials*

Regio-regular poly(3-hexylthiophene) (P3HT) was purchased from Rieke Metals (Lincoln, NE) and poly(2-methoxy-5-(2′-ethylhexyloxy)-1,4-phenylenevinylene) (MEH-PPV) was purchased from Sigma-Aldrich (St. Louis, MO). Both polymers were purified by successive Soxhlet extractions with methanol, acetone, and hexane. Poly(9,9-dioctylfluorene-co-benzothiadiazole) (F8BT) was purchased from American Dye Source (Baie D'Urfé, Quebec) and was used as received. Poly(3-decyl-2,5-thienylene vinylene) (P3DTV) was prepared using methods previously reported.[132] 1-Ethyl-3-methylimidazolium bis(trifluoromethylsulfonyl)imide ([EMI][TFSA]), 1-butyl-1-

methylpyrrolidinium bis(trifluoromethylsulfonyl)imide ([P14][TFSA]), 1-ethyl-3-methylimidazolium tris(pentafluoroethyl)trifluorophosphate ([EMI][FAP]), 1-butyl-1-methylpyrrolidinium tris(pentafluoroethyl)trifluorophosphate ([P14][FAP]), and trihexyl(tetradecyl)phosphonium tris(pentafluoroethyl)trifluorophosphate ([P666,14][FAP]) were purchased from EMD Chemicals (Gibbstown, NJ)) and used as received. Cobaltocenium hexafluorophosphate ($CcPF_6$) was purchased from Sigma-Aldrich (St. Louis, MO) and used as received.

### *6.3.2 Device Fabrication and Characterization*

E-beam evaporation (Temescal) was used to deposit a 25 Å Cr adhesion layer followed by 225 Å of Au on 1"x1" glass substrates, as measured by a quartz crystal microbalance. Source and drain electrodes were separated by a 250 $\mu$m channel defined using a wire shadow mask during depositions. Electrode thickness was confirmed with profilometery (KLA-Tencor). 10 mg/ml solutions of P3HT and P3DTV in 1,2-diclorobendzene, and 5 mg/ml solutions of MEH-PPV in chloroform were spin-coated at 2000 rpm for 2 min, followed directly by a 20 min bake on a hot plate at 105 ºC to drive off residual solvent. F8BT was spin-coated from a solution of 20 mg/ml in toluene at 2000 rpm for 2 min, followed directly by a 20 min anneal on a hot plate at 290 ºC. Solution preparation, spin-coating, and baking steps were all preformed in an inert atmosphere glovebox ($O_2$ < 5 ppm). Polymer layer thickness was measured by profilometery.

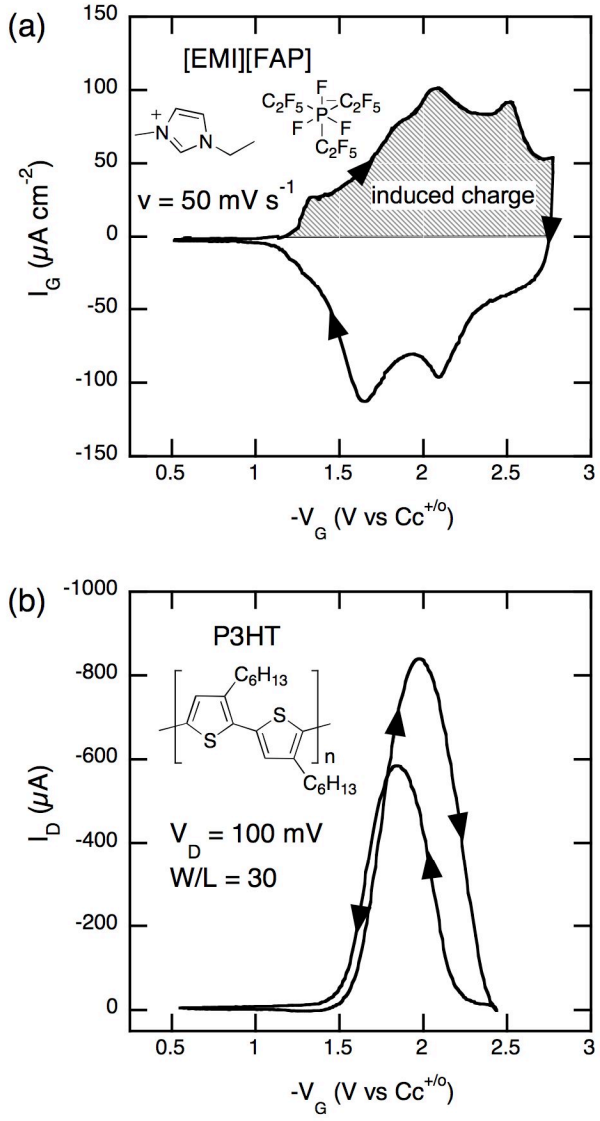


**Figure 6.2** (a) A cyclic voltammogram ($I_G$-$V_G$) of an [EMI][FAP] gated ~50 nm thick P3HT film, $V_G$ is swept at 50 mV $s^{-1}$. (b) Drain current as a function of gate voltage for an [EMI][FAP] gated ~30 nm thick P3HT film with a W/L aspect ratio of 30 and a 100 mV source to drain bias.

### *6.3.3 Electrical and Electrochemical Measurements*

Electrochemical measurements were carried out in a ~1 ml Teflon cell with a Pt mesh counter electrode and Ag wire quasi-reference electrode, Figure 6.1. Assembled cells had a defined working electrode area of 0.709 $cm^2$. Cyclic voltammagrams (CV)

and *in situ* conductivity were measured using a Pine AFRDE5 bipotentiosat with an analog-to-digital converter (LabJack) to log the data. The cells were assembled and tested in an inert atmosphere glovebox. Room and variable temperature CV with *in situ* conductivity measurements was carried out with the cell in a Desert Cryogenics vacuum probe station with a temperature-controlled stage. The vacuum probe station was housed in an inert atmosphere glovebox so that air exposure of the samples could be rigorously avoided.

## *6.4 Results and Discussion*

### *6.4.1 Electrochemistry and Finite Potential Window of Conductivity for [EMI][FAP]-Gated P3HT*

Figure 6.2 shows the cyclic voltammogram and source-to-drain current of [EMI][FAP] gated P3HT as a function of gate bias, $V_G$. $-V_G$ is equivalent to the potential of the working (source) electrode. P3HT films gated with [EMI][FAP], Figure 6.2a, displayed an onset of oxidative charging at a referenced gate bias of +1.25 V versus the $Cc^{+/o}$ redox couple. An initial charging feature occurred at +1.35 V, consistent with reported electrochemistry of regioregular P3HT.[133] This feature is attributed to the preferential oxidation of the crystalline domains, as it is not observed in fully amorphous regiorandom P3HT. Following were additional oxidation peaks at +1.85, +2.10, and +2.50 V vs $Cc^{+/o}$. P3HT showed stable oxidation out to +2.8 V, which is 800 mV beyond what is typically obtainable in P3HT gated with a traditional organic electrolyte. Two large reduction peaks dominated the reverse sweep at +2.10 and +1.65 V. When [P14][FAP] was employed as the gate electrolyte, the resulting cyclic voltammagrams, Figure 6.3, were essentially identical. The small initial peak, shoulder, and two larger

forward oxidative peaks all occurred at the same potentials. However, the return reduction peaks occurred ~150 mV lower potentials indicating a more difficult dedoping process when using [P14][TFSA].

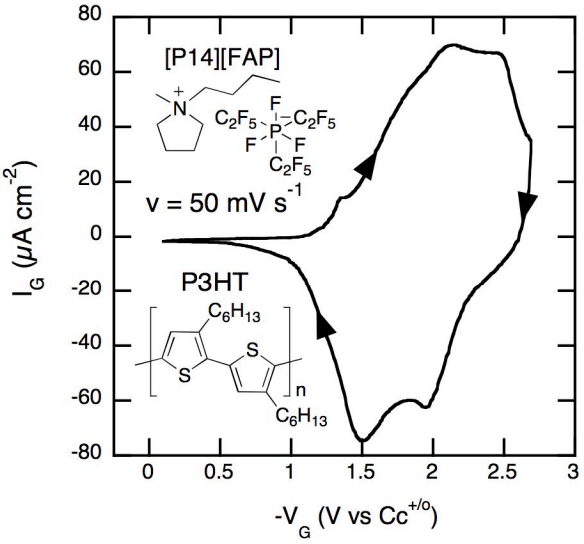


**Figure 6.3** Cyclic voltammogram of a ~30 nm thick P3HT film gated with [P14][FAP].

With the drain biased at +100 mV relative to the source, the resulting hole channel current, Figure 6.2b, overcame the film charging currents and showed measurable conduction at +1.4 V. $I_D$ increased dramatically with increasing potential, peaking at +2.0 V, beyond which it dropped rapidly until being largely suppressed by +2.45 V. Thus, there is a peak in $I_D$ vs $V_G$ and a finite electrochemical window between +1.5 and +2.4 V over which conductivity is high. On the reverse sweep, $I_D$ again showed similar behavior, but the peak in $I_D$ was shifted 130 mV negative, and suppressed by 30%. This current suppression on the reverse sweep was not attributed to any irreversible degradation, as both the forward and reverse currents showed excellent sweep-to-sweep repeatability and stability. In fact, a [EMI][FAP] gated P3HT film with $V_D$ = +100 mV

was cycled 70 consecutive times through the conduction window and displayed only a 12% decrease in the forward and reverse peak currents, Figure 6.4. When films were cycled a few times and then allowed to rest at open circuit for a few minutes, successive cyclic voltammograms and transfer curves were identical to the initial one. This excellent stability allowed a rigorous study of charge carrier density and hole transport without being limited by device stability over time and potential.

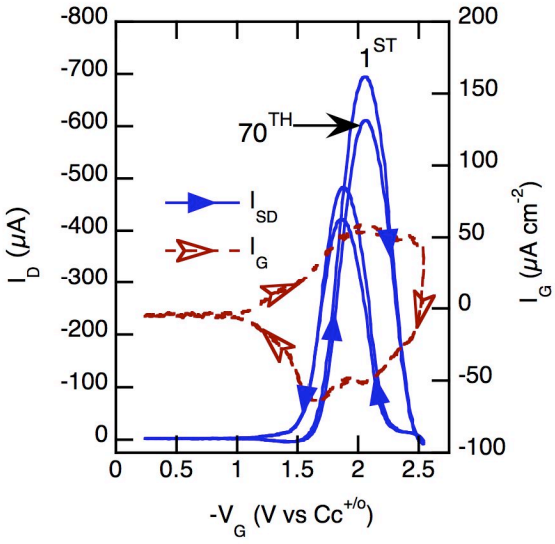


**Figure 6.4** 1st and 70th consecutive cyclic voltammograms and transfer curves of a ~30 nm thick P3HT film gated with [EMI][FAP].

### *6.4.2 Charge Density Determination*

An accurate measure of the induced charge carrier density is required to investigate charge transport in a meaningful way. Electrolyte gated devices share much in common with field effect devices and can be described with very similar models.[134] In traditional FET measurements the charge density may be estimated assuming a constant capacitance of the dielectric with charge accumulation occurring beyond some threshold voltage.[135] Recent reports on high performance electrolyte gated transistors have used a

method similar methodology, but in place of a constant capacitance, a low frequency potential dependent capacitance was determined by impedance spectroscopy.[136] In the case of electrolyte gated polymer devices, the charging is considered "pseudocapacitive" in nature as charge is induced due to a redox reaction in the polymer, as opposed to the simple electrostatic means (the "field effect") in the case of traditional dielectric capacitor structures.[137] Measuring this charging is complicated in electrolyte gated materials due to (i) mass transport of the charge carrier stabilizing ions, (ii) side reactions that do not result in induced charge carriers, (iii) and electrical leak at the polymer-electrolyte interface. Additionally, those same processes may occur at the gate electrode-electrolyte interface. In order to avoid unnecessary assumptions, a direct charge density measurement, decoupled from gate electrode effects, that can be carried out simultaneously with conductivity measurements is desired.

We measure the charge induced in [EMI][FAP] gated P3HT with a cyclic voltammogram, in the same manner as a displacement current measurement is used to measure capacitively induced charge in a traditional field effect structure.[138,139] The application of a large area platinum mesh gate (counter) electrode in a liquid cell minimizes the influence of gate electrode processes. The magnitude of the induced charge, $Q$, was calculated by integration of the gate current, $I_G$, of the forward portion of the cyclic voltammogram.

$$Q = \int \frac{I_G}{\left(dV/dt\right)} dV$$

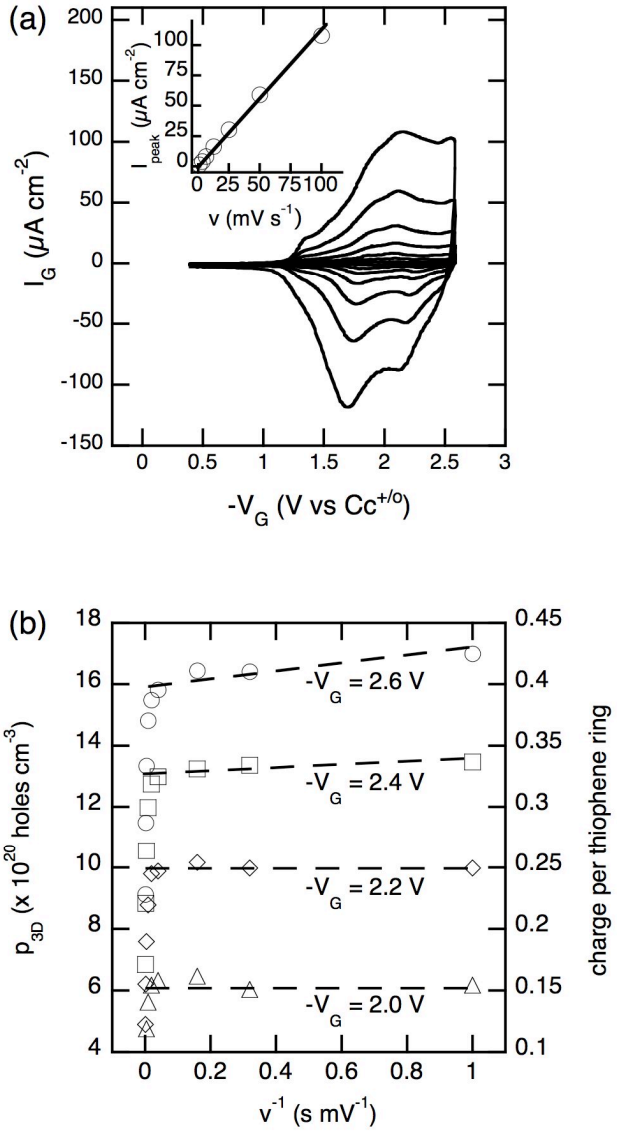


**Figure 6.5** (a) Cyclic voltammograms with peak current densities (inset) at sweep rates of 1 to 100 mV $s^{-1}$ and (b) integrated potential dependent charge densities at sweep rates of 1 to 800 mV $s^{-1}$ in a ~30 nm thick P3HT film gated with [EMI][FAP]. Below sweep rates of ~100 mV $s^{-1}$, charge density is independent of sweep rate.

The three-dimensional charge carrier density, $p_{3D}$, was determined by dividing the induced charge by the area of the polymer-coated electrodes, thickness as measured by profilometery, and the unit charge.

$$p_{3D} = \frac{Q}{eAt_{film}}$$

Note that the polymer thickness was measured on the neat, undoped polymer film, and the film will swell upon electrochemical doping, introducing a systematic error in $p_{3D}$. However, the variation in $t_{film}$ does not affect estimation of the charge per thiophene ring. To estimate the fraction of thiophene rings charged, the charge carrier density was multiplied by the volume of the crystalline P3HT unit cell (1.00 x $10^{-21}$ $cm^3$) and divided by the number of thiophene rings units in each cell.[140]

$$charge/thiophene\ ring = \frac{p_{3D}V_{Cell}}{4}$$

This estimate treats the entire film as crystalline, although the volume fraction of crystalline domains in P3HT is only on the order of 20%, with the remainder being amorphous. Generally, in semi-crystalline polymers the amorphous domains are 10-15% less dense than the crystalline domains.[141] In the case of regioregular P3HT, the density of the amorphous domains has yet to be quantified, and the commonly reported P3HT density of 1.1 g $cm^{-3}$ is in fact derived from x-ray crystallography.[142] Thus, the charge per thiophene ring may be over estimated by as much as 10%.

In order to assure the viability of these methods to access charge density, cyclic voltammograms of P3HT gated with [EMI][FAP] were collected over a series of sweep rates, Figure 6.5a. Figure 6.5b shows the integrated charge of the forward sweep versus inverse sweep rate for a variety of channel potentials. The plateau between sweep rates of 1 and 100 mV $s^{-1}$ reveals a sweep rate independent constant maximum pseudocapacitive charge attainable in the polymer film at a given potential. At higher

sweep rates the integrated charge abruptly falls off as the diffusion of ions into the polymer film limits charging of the film. Only at extreme potentials above +2.2 V vs $Cc^{+/o}$, does the plateau at low sweep rate take on a finite slope (Figure 6.5b) due to charge transfer of a nonpseudo-capacitive nature, *i.e.*, leak currents. Oxidative charging was observed to be completely reversible, *e.g.* integrated *reverse* (negative going) scans of [EMI][FAP] gated P3HT films revealed >99% of the induced positive charge was removed. Furthermore, the peak current values of the oxidation peaks, shown in Figure 3b inset, scaled linearly with sweep rate over the range of 1 to 100 mV/s, consistent with complete charging of a surface-localized material.[143,144]

These variable sweep rate displacement current measurements revealed that [EMI][FAP] gated P3HT readily and reversibly reached charge densities of 1.8 x $10^{21}$ holes $cm^{-3}$ (at +2.75 V), which corresponds to 0.4 – 0.5 holes per thiophene ring along the polymer backbone. Charge density was also determined by integrating the current decay following a potential step. Charge densities obtained by this method exceeded the sweep rate plateau values (Figure 6.5b) by >15%, probably due to the inability to deconvolute the current components due to psuedocapacitive charging and the Cotrell-like behavior of the leak currents.

When inducing such high charge densities it is important to consider the effect of ion incorporation on film structure, in particular the effect of film swelling. Assuming that no void space within the P3HT is available to the anion dopant, an upper limit to the degree of expected swelling was calculated by adding the Van der Waals volume of the incorporated anions. The Van der Waals volume of the anions was calculated using a

method based on the Bondi Radii, which gave good agreement with a wide range of other IL constituent anions and cations calculated with more rigorous methods.[145,146] In the case of the [FAP] and [TFSA] anions, the P3HT film has likely not swollen more that 50% and 40%, respectively, at the highest induced charge attained in this study (~0.5 dopant anions per thiophene ring). Likewise, at peak conductivity, the [EMI][FAP] doped P3HT has likely not swollen more than 15%. This calculation of a upper limit on swelling is in agreement with x-ray crystallography studies of poly(3-alkylthiophene) incorporating a variety of anion species, which show that crystallinity is retained up to loadings of 0.45 charge per thiophene ring.[147,148,149] Thus, the maximum charge density *per volume* quoted above, 1.8 x $10^{21}$ holes $cm^{-3}$, may actually be closer to 1 x $10^{21}$ holes $cm^{-3}$, considering the effects of swelling. However, the charge concentration calculated *per thiophene ring* should be unaffected.

### *6.4.3 Charge Density Dependent Hole Transport*

An accurate measure of the hole density allows the determination of the average hole mobility, $\mu$, as a function of hole density. In the regions of high charge carrier densities and high conductivity, as considered here, spectroscopic studies have shown that the charge carriers in P3HT predominately exist as diamagnetic bipolarons,[150,151] with the conversion of polarons to bipolarons corresponding to a dramatic increase in hole mobility.[152] When considering the charge transport in these regimes, it is convenient to consider the transport behavior in terms of a disorder dominated hopping process.[153,154] In agreement with previous theoretical and experimental studies, $\mu$ initially increases with

increasing charge density, as the number of available hopping sites increases.[118,128,135,155.156.157.158.159.160.161]

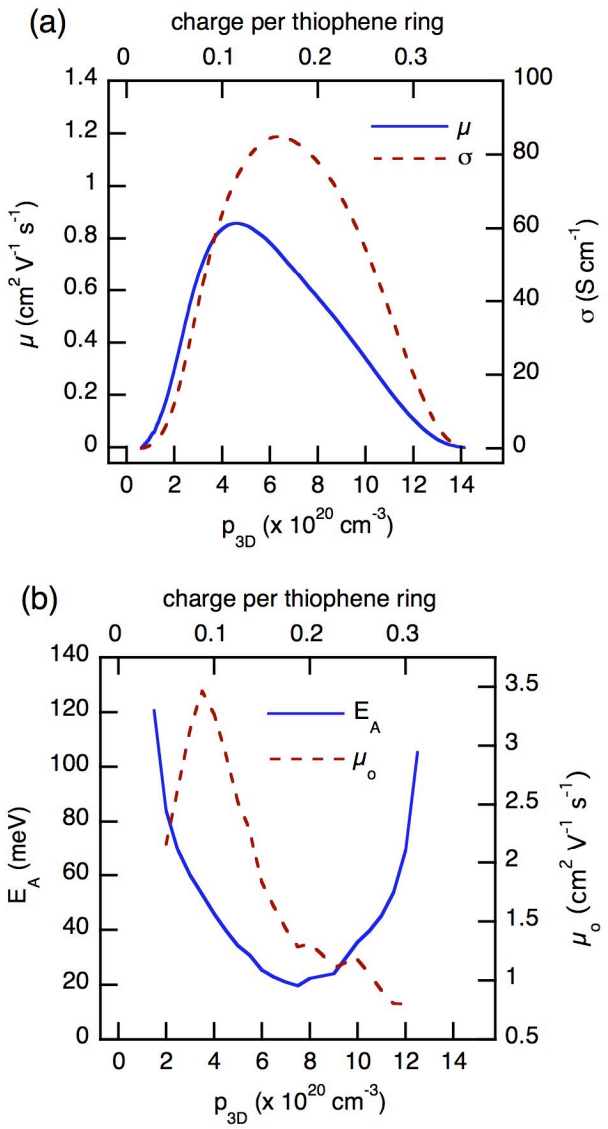


**Figure 6.6** Room temperature charge density dependent (a) conductivity and hole mobility, and (b) activation energy and exponential prefactor ($\mu_o$) of a [EMI][FAP] gated P3HT film.

As shown in Figure 6.6a, hole mobility was 1.3 x $10^{-2}$ $cm^2$ $V^{-1}$ $s^{-1}$ at 0.03 holes per thiophene ring, and steadily increased with increasing charge density, reaching a maximum of 0.86 $cm^2$ $V^{-1}$ $s^{-1}$ at 0.12 holes per thiophene repeat unit, or 4.6 x $10^{20}$ holes

$cm^{-3}$. Beyond 4.6 x $10^{20}$ holes $cm^{-3}$, the mobility decreased, but the hole density steadily increases, resulting in a peak conductivity of 85 S $cm^{-1}$ at 0.16 holes per thiophene repeat unit, or 6.4 x $10^{20}$ holes $cm^{-3}$. Further increases in charge density resulted in decreases in hole mobility and conductivity, which were largely suppressed by 0.35 holes per thiophene repeat unit, or 1.4 x $10^{21}$ holes $cm^{-3}$. This behavior was found to be highly reproducible sweep-to-sweep and device-to-device, with six devices displaying the same mobility charge density relationship, and an average peak hole mobility value of 0.80 ± 0.08 $cm^2$ $V^{-1}$ $s^{-1}$ (error is one standard deviation).

A general weakening of the charge density dependence and eventual plateau of carrier mobility at very high carrier density has been theoretically described,[160,162,163] but detailed comparisons of models with experimental measurements at charge densities beyond $10^{21}$ holes $cm^{-3}$ (clearly in the negative transconductance regime) have not been reported. Spectroscopic experiments have been employed to determine the degree of delocalization of holes in P3HT. Electron-nuclear double-resonance studies have pointed to charge delocalization over roughly 20 thiophene rings.[164] Additionally, Kaake, *et al* have reported the complete quenching of neutral ring infrared modes at an equivalent charge density of one hole for every twenty thiophene rings.[165] At this charge density, we measure high hole mobilities of ~0.4 $cm^2$ $V^{-1}$ $s^{-1}$. Based on prior spectroscopy results, at the hole concentration corresponding to peak mobility, which is one hole for every eight thiophene rings, there is very substantial overlap of the localized hole wave functions.

To further investigate the hole transport throughout the finite potential window of conductivity, transfer curves with simultaneous cyclic voltammograms of P3HT were

collected from 350 K down to the freezing point of [EMI][FAP] near 250 K. Electrochemical reference potentials are known to be temperature dependent, likewise the pseudocapacitance cannot be assumed to be independent of temperature. Therefore, dynamic measurements above the ionic liquid freezing point were carried out, allowing for direct charge density measurements, obviating any assumptions of charge density. The temperature dependent constant charge density mobility was fit with a simple Arhennius relation, Figure 6.7. Figure 6.6b shows plots of the activation energy, $E_A$, and the mobility pre-exponential factor, $\mu_o$, as a function of hole density.

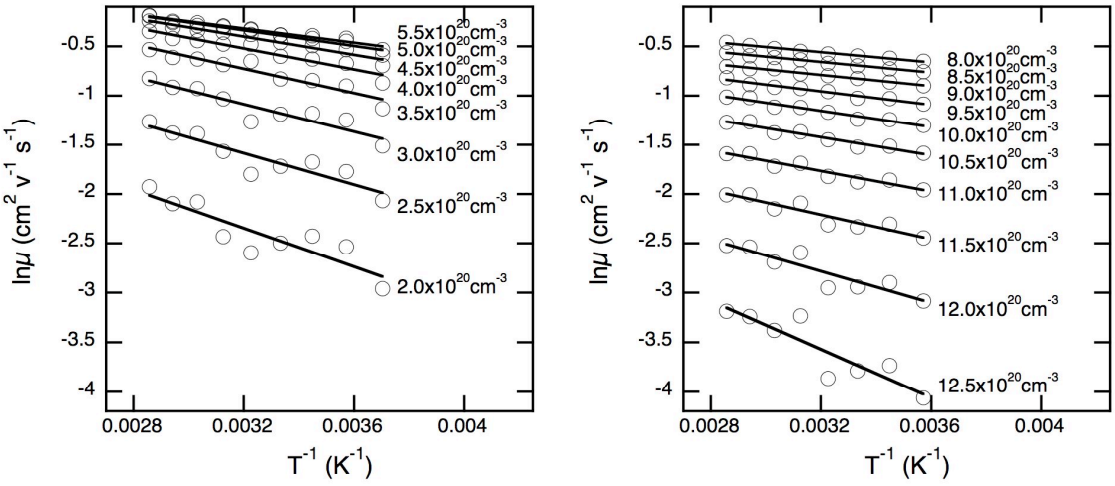


**Figure 6.7** Natural log of hole mobility plotted versus inverse temperature of a [EMI][FAP] gated P3HT film at various charge densities.

Upon increasing hole density, the activation energy expectedly dropped leading to a region of very weakly activated transport ($E_A$ = 20 – 25 meV) between 6 x $10^{20}$ and 9 x $10^{20}$ holes $cm^{-3}$. Beyond 9 x $10^{20}$ holes $cm^{-3}$ the activation energy increased as hole mobility and conductivity decreased. The activation energy mirrored the conductivity, with the highest conductivity occurring in the region of lowest activation energy.

Likewise, the pre exponential factor roughly followed the same trend as the mobility, increasing with increasing charge density to a peak at ~4 x $10^{20}$, near the mobility peak, and decreasing with further increasing hole density. While the activation energy for hole mobility dropped considerably, hole transport remained weakly activated and did not transition into a metallic regime.

### *6.4.4 Electronic Density of States*

With an accurate measurement of both charge density and electrochemical potential, it is possible to map the electronic density of states (DOS) for electrochemically doped P3HT.[166,167] To achieve this, calibrated electrochemical potentials can be converted to the vacuum energy scale.[168] The relative quasi-reference electrode potentials of $Fc^{o/+}$ and $Cc^{+/o}$ redox couples in ionic liquid electrolytes have been shown to be consistent with traditional electrolyte systems.[169] Taking the onset of oxidation in P3HT gated with [EMI][FAP] to be the reported value of 5.1 eV below the vacuum level,[170] the electrochemical DOS was mapped. The value of the DOS was derived directly from the gate charging current measured with cyclic voltammetry.

$$DOS = \frac{dN}{dE} = \frac{\Delta Q}{eV_{film}\Delta E} = \frac{I_G}{evt_{film}}$$

The number of states available at a given energy level can be described as the change in induced charge, $\Delta Q$, divided by the product of the change in potential, $\Delta E$, volume of polymer film ($V_{film}$) and the electron charge ($e$). This in turn is equal to the gate current density, $I_G$, divided by the potential sweep rate ($v$), film thickness ($t_{film}$) and the electron charge.

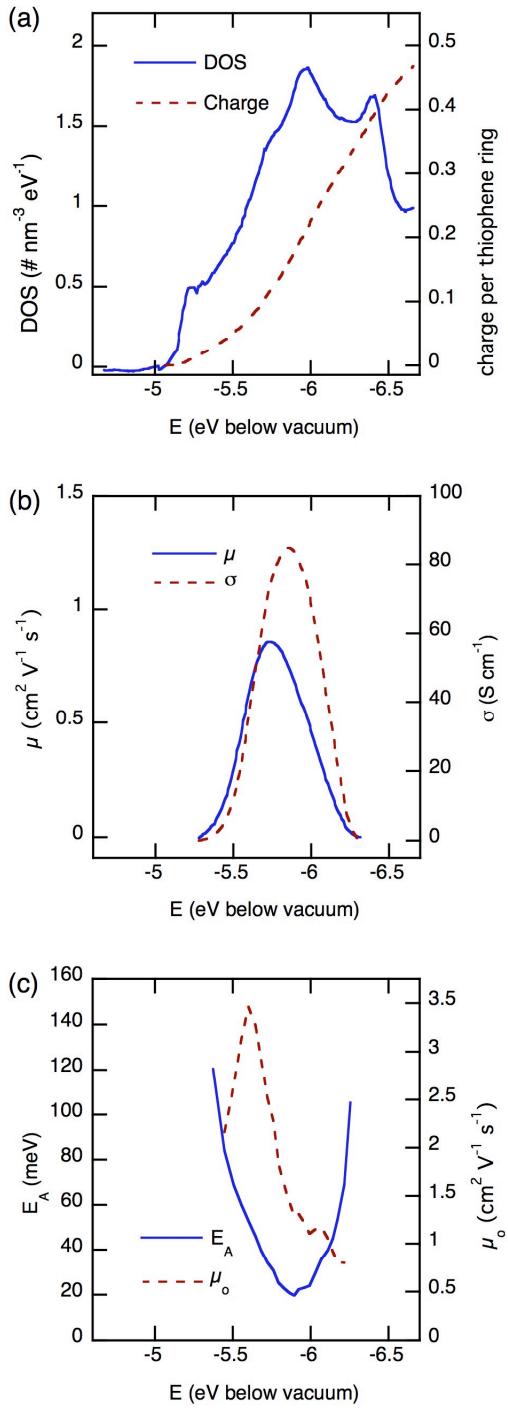


**Figure 6.8** Room temperature (a) electrochemical density of states and total hole concentration per thiophene ring, (b) hole mobility and conductivity, and (c) variable temperature derived activation energy and exponential prefactor ($\mu_o$) vs energy of a [EMI][FAP] gated P3HT film.

Figure 6.8a displays plots of the DOS and total accumulated holes per thiophene ring, to a depth of 6.7 eV below vacuum level. The measurable DOS displayed a complex structure and spanned 1.5 eV, though it appeared to extend deeper than the anodic stability limit of [EMI][FAP]. It is important to bear in mind that the DOS obtained this way pertains to the doped P3HT/[EMI][FAP] *composite*, i.e., the DOS is not the same for a neat P3HT film. Electrical transport in neat P3HT can accurately be described by a Gaussian DOS with a width of 0.1 eV,[171,172] which is drastically narrower than the DOS of the doped P3HT/[EMI][FAP] composite. Electrochemical doping likely introduces additional structural and electrostatic disorder which leads to a broadening of the DOS, resulting in DOS widths that are significantly larger than the neat material.[158,173] Also the semiconductor film will swell upon electrochemical doping, which introduces systematic error in $t_{film}$ noted previously. Thus, the DOS values in Figure 6.8a (left axis) could be conceivable inaccurate by up to 50%. The shape and widths, however are unaffected, and likewise the charge per thiophene ring (right axis) is also unaffected by swelling of the film.

The shape, size, and total number of states of the DOS of conjugated polymers, and their doped composites, are still areas of active discussion. Here, the DOS of [EMI][FAP] doped P3HT was found to display a small shallow peak, a shoulder, and two additional peaks at 5.2, 5.7, 6.0, and 6.4 eV respectively. Previously the DOS shape of doped P3HT has been considered to be exponential,[174] Gaussian,[160] or a combination of two Gaussians.[158] Our experimentally measured DOS is much more complex in shape, and can be approximated with no fewer that four Gaussians. It should be noted that our

highest induced charge density, 1.8 x $10^{21}$ holes $cm^{-3}$, exceeds by a factor of two what previous studies had considered to be the total number of states in the DOS.[158,171]

The mobility and conductivity previously plotted versus charge density can be replotted on the absolute energy scale, Figure 6.8b, as the conductivity measurements were carried out versus a calibrated reference electrode. Consistent with earlier work, we propose the shallowest features of the DOS are due to the preferential charging of the crystalline domains of P3HT, which provide a lower energy state for holes to occupy.[175] The filling of these states precedes the dramatic increase in mobility and conductivity, which does not occur until 150 meV into the DOS, at which point the hole density has already reached ~0.01 holes per thiophene ring or ~4 x $10^{19}$ holes $cm^{-3}$.

A peak hole mobility of 0.86 $cm^2$ $V^{-1}$ $s^{-1}$ and a shoulder in the DOS both occurred at ~5.7 eV, at a hole density of 4.6 x $10^{20}$ holes $cm^{-3}$. As mentioned above, this density corresponds to a hole on every eighth thiophene ring. Up to the mobility maximum, the DOS can be adequately approximated with two Gaussian distributions, in agreement with transport modeling[158] and molecular dynamic studies,[176] albeit with significantly broader Gaussians. Beyond 5.7 eV the mobility decreases, but the hole density is steadily increasing, resulting in a peak conductivity of 85 S $cm^{-1}$ at ~5.9 eV. Filling states deeper into the DOS, the mobility drops dramatically, largely suppressing conduction by 6.3 eV, equivalent to 1.4 x $10^{21}$ holes $cm^{-3}$ or 0.35 holes per thiophene ring. To our knowledge, the mobility decrease and the features of the DOS at these extreme charge densities and potentials has not received extensive theoretical consideration.

The charge density dependent activation energy and pre exponential factor can also be converted to the vacuum scale (Figure 6.8c). Traveling deeper into the hole DOS, the activation energy expectedly drops as the number of accessible transport states grows. This leads to a region of very weakly activated transport ($E_A$ = 20 – 25 meV) between 5.8 and 6.0 eV. The pre-exponential factor peaks at 5.6 eV and decreases deeper into the DOS. Beyond 6.0 eV the activation energy increased as hole mobility decreased and conductivity was minimized. The hole mobility and DOS behavior can be summed up in the following: initial charging introduces deep coulomb traps that inhibit mobility. Beyond some threshold (~4 x $10^{19}$ holes $cm^{-3}$) mobility rapidly increases as localized hole wave functions begin to overlap. However it may be that concomitant disorder, including film swelling, due to ion incorporation may eventually counteract the carrier wave function overlap, frustrating the achievement of a more conductive state, and eventually suppressing mobility.

### *6.4.5 Cation and Anion Effects*

The numerous possible combinations of anions and cations, which form ionic liquids, allow for wide tunability of ionic liquid properties, such as viscosity, ionic conductivity, and electrochemical stability.[177,178] Additionally, when used as electrolyte gates, the interactions between the ionic liquid and the gated material produce significant differences in charge carrier transport.[179,180] To investigate the dependence of polymer conductivity on choice of ionic liquid, P3HT was gated with various combinations of the [EMI] and [P14] anions, and the [FAP], [TFSA], and [P14,6,6,6] cations.

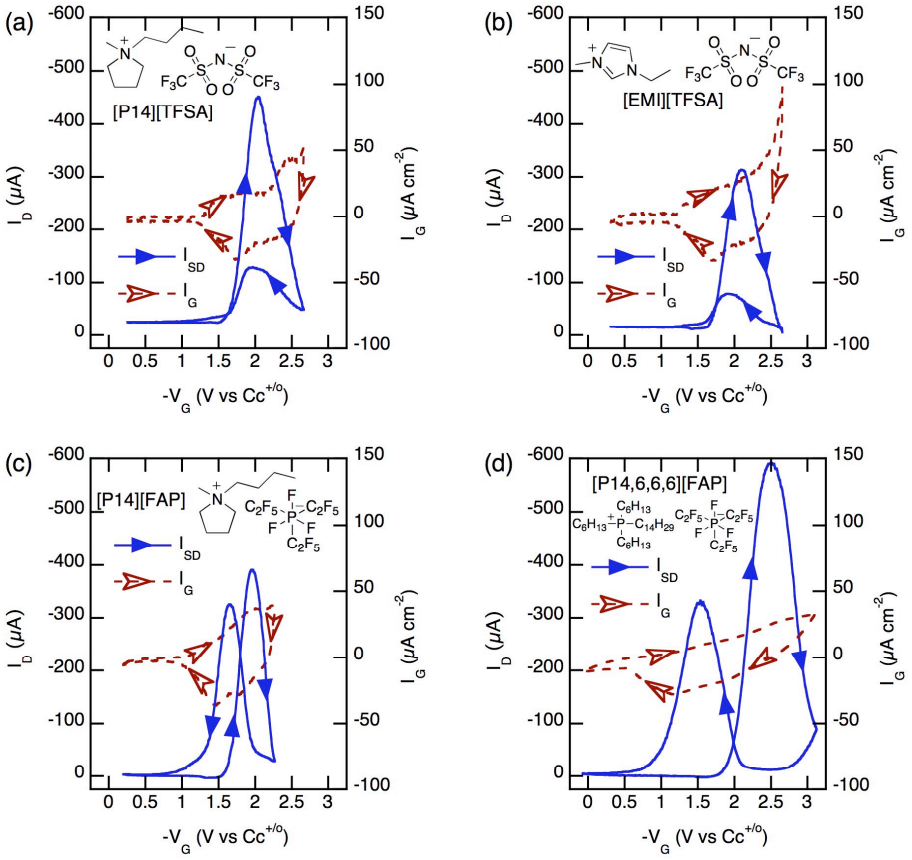


**Figure 6.9** Simultaneously collected transfer curves and cyclic voltammograms of ~30 nm P3HT films gated with (a) [P14] [TFSA], (b) [EMI][TFSA], (c) [P14][FAP], and (d) [P14,6,6,6][FAP] ionic liquid electrolytes collected at a sweep rate of 50 mV $s^{-1}$ and a source drain bias of 100 mV.

Figure 6.9 shows simultaneously collected transfer curves and cyclic voltammograms of P3HT gated with [P14][TFSA], [EMI][TFSA], [P14][FAP], and [P14,6,6,6][FAP]. Similar to [EMI][FAP], shown in Figure 6.2, all four ionic liquid gates revealed a finite electrochemical window of conductivity in P3HT with their peak hole mobility and conductivity values shown in Table 6.1.

**Table 6.1** Peak hole mobility, peak conductivity, forwar d-reverse current maxima hysteresis, and IL viscosity for various P3HT/IL combinations.

| ionic liquid | $\mu_{peak}$ ($cm^2\ V^{-1}\ s^{-1}$) | $\sigma_{peak}$ ($S\ cm^{-1}$) | Hysteresis (mV) | $\nu_{IL}$ ($mm^2\ s^{-1}$) |
|---|---|---|---|---|
| [EMI][TFSA] | 0.37 | 37.3 | 190 | - |
| [P14][TFSA] | 0.70 | 53.6 | 90 | - |
| [EMI][FAP] | 0.86 | 84.8 | 130 | 20.1[56] |
| [P14][FAP] | 0.46 | 46.5 | 310 | 60.9[56] |
| [P14,6,6,6][FAP] | ~0.6 | 70.4 | 970 | 120.4[56] |

[P14][TFSA] and [EMI][TFSA] gated P3HT revealed onsets of oxidation at +1.25 and +1.30 V vs $Cc^{+/o}$ respectively, and onsets of substantial conductivity at +1.55 and +1.60 V, respectively. A broad reduction feature, consisting of a shoulder and a peak, dominated reverse sweeps. Both ionic liquids incorporating the [TFSA] anion showed a heavily suppressed conductivity peak on the return sweep, and poor sweep-to-sweep reproducibility, with both the forward and reverse conductivity peaks severely degrading with successive sweeps. This irreproducibility is attributed to an irreversible reaction between the P3HT and the IL at high potentials. For [EMI][TFSA], the gate current exhibited a clear exponential character past +2.5 V, indicative of electrolyte break-down. This electrochemical instability is likely due to the presence of impurities, the most detrimental of which is water. ILs incorporating the [TFSA] anion are known to be relatively hydrophilic in comparison to ILs incorporating the [FAP] anion, and water content drastically reduces the potential window of electrochemical stability.[181]

P3HT films gated with [P14][FAP] shared much in common with [EMI][FAP] gated films (see Supporting Information). The onset of oxidation occurred earlier at +1.15 V, and the onset of substantial conductivity at +1.55 V. At +1.35 V, an oxidation

peak associated with charging of the P3HT crystalline domains occurred, followed by a large oxidation peak at +2.0 V. The hysteresis between forward and reverse peak conductivity was 300 mV, over twice that of [EMI][FAP]. While the electrochemical stability was on par with [EMI][FAP], the mobility reached a maximum of 0.45 $cm^2 V^{-1} s^{-1}$, roughly half of what was obtained with [EMI][FAP] gated P3HT. P3HT films gated with [P14,6,6,6][FAP] showed distorted cyclic voltammograms, with a very large hysteresis between the forward and reverse peak conductivity of 970 mV. Charge density determination was frustrated by the lack of a clear onset of oxidation, however the peak conductivity approached that of [EMI][FAP] gated films.

The anion choice ([TFSA] vs [FAP]) was found to determine the device stability. Both ionic liquids containing the [TFSA] anion showed poor stability and reproducibility at potentials beyond ~2.0 V, regardless of cation choice. In contrast, all three ionic liquids containing the [FAP] anion displayed excellent anodic stability, allowing a clear view of the finite potential window of conductivity with good sweep-to-sweep reproducibility.

The electrochemical and charge transport behavior of [FAP]-containing ILs still showed significant variation depending on cation choice. The peak achievable hole mobilities and conductivities were found to be affected by choice of cation, with [EMI][FAP] displaying hole mobility and conductivity values nearly twice that of [P14][FAP]. This electrical transport dependence has been proposed to be due the strength of the hole-ion interaction. [179,180] Unfortunately, in this system the strength of the

hole-anion interaction is more difficult to assess and the elucidation of the hole mobility dependence on IL choice requires further investigation.

The cation choice also affected the forward-reverse hysteresis of the *I-V* curves. The hysteresis of the conductivity peak was found to directly relatable to the viscosity of the ionic liquid,[182] Table 6.1, which is strongly dependent on cation choice. It has been shown that ion diffusivities of ionic liquids are inversely proportional to viscosity,[183] thus the observed hysteresis is dependent on ion transport. Additionally, these ion transport effects are likely due to ion transport in and out of the P3HT film, as the hysteresis also showed a marked dependence on P3HT thickness.

Both of these effects show that the P3HT is not doped and dedoped through simple anion transport in and out of the film. Instead, the cation is of key importance in the doping/dedoping process, either through charge-balanced solvation of mobile anion dopants, or by cation transport to counter balance trapped anion dopants. The latter is most likely occurring in IL/P3HT systems as recent electrochemical quartz crystal mircobalance studies of IL doped polythiophene derivative, PEDOT, have shown that some anions become trapped and that the doping/dedoping process occurs by a combination of both anion and cation transport.[184] This would imply that after the first cycle, the film is a swollen P3HT/IL composite regardless of whether it is neutral or oxidized, with the relative amount of incorporated anions and cations varying with the degree of oxidation.

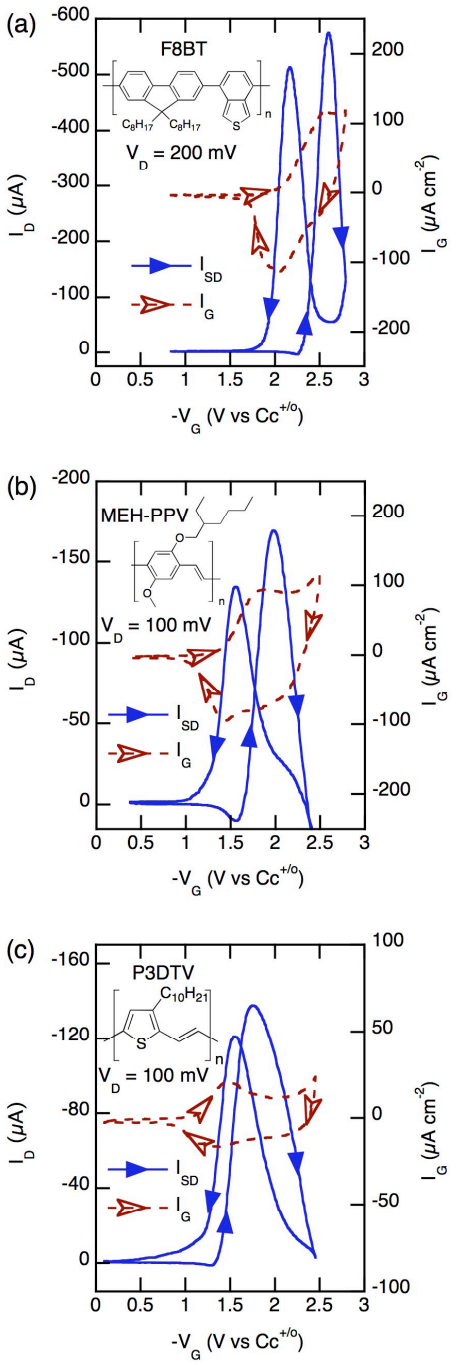


**Figure 6.10** Simultaneously collected $I_D$-$V_G$ and cyclic voltammograms of (a) a F8BT film swept at 25 mV $s^{-1}$ with a source drain bias of 200 mV, and (b) MEH-PPV and (c) P3DTV films both swept at 50 mV $s^{-1}$ with a source drain bias of 100 mV, all gated with [EMI][FAP] ionic liquid electrolyte.

### *6.4.6 Polyfluorene, Polyphenylenevinylene, and Polythienylenevinylene*

The wide electrochemical stability window of [EMI][FAP] was employed to explore the generality of the finite potential window of conductivity in several semiconducting polymers. Figure 6.10 shows the simultaneously collected transfer curves and cyclic voltammograms of the polyfluorene, F8BT, the poly(phenylene vinylene), MEH-PPV, and the low bandgap poly(thienylene vinylene), P3DTV, all gated with [EMI][FAP]. All three show the general behavior seen in the P3HT/[EMI][FAP] system, Figure 6.2, consisting of electrochemical oxidation followed by a dramatic increase in film conductivity, which peaks and rapidly decreases with further oxidation. Upon the reverse cathodic sweep back to the neutral state, broad reduction peaks are observed coupled again with finite conductivity regimes, with varying degrees of hysteresis between forward and reverse peak conductivities.

**Table 6.2** Oxidation onsets, conduction onsets, HOMO levels, and peak mobility and conductivity values of various polymer semiconductors gated with [EMI][FAP].

| polymer | $E_{ox,onset}$ (V vs $Cc^{+}/Cc^{o}$) | $E_{cond,onset}$ (V vs $Cc^{+}/Cc^{o}$) | HOMO (eV) | $\mu_{peak}$ ($cm^2\ V^{-1}\ s^{-1}$) | $\sigma_{peak}$ ($S\ cm^{-1}$) |
|---|---|---|---|---|---|
| P3DTV | +1.15 | +1.35 | 5.0[38] | 0.27 | 20.9 |
| P3HT | +1.25 | +1.40 | 5.1[38] | 0.86 | 84.8 |
| MEH-PPV | +1.40 | +1.70 | 5.2[53] | 0.08 | 6.9 |
| F8BT | +2.05 | +2.30 | 5.9[54] | 0.07 | 11.7 |

The oxidation and conduction onsets of all the polymers trend with reported HOMO levels,[160,185,186] with oxidation and conduction in P3DTV, having the shallowest HOMO level, occurring at the lowest potentials, and F8BT, having the deepest HOMO level, occurring at the highest potentials. In the case of the F8BT, the onset of oxidation occurred at +2.05 V vs $Cc^{+/o}$. The single oxidation peak occurred at +2.55 V, and was

rapidly followed by the peak in conductivity of 11.7 S $cm^{-1}$ at +2.60 V. A peak mobility of 8.3 x $10^{-2}$ $cm^2$ $V^{-1}$ $s^{-1}$ was reached at a potential +2.55 V. There was a hysteresis of 440 mV in the conductivity peak between the forward and reverse sweep. The reproducibility on successive sweeps using a polymer with a HOMO a full 1 eV deeper than P3HT further revealed the extended anodic stability of [EMI][FAP] as a gate for polymer systems.

The onset of oxidation of MEH-PPV occurred at +1.40 V. The peak mobility of 8.1 x $10^{-2}$ $cm^2$ $V^{-1}$ $s^{-1}$ occurred nearly simultaneously to the single oxidation peak near +1.9 V, and was of the same order of previously reported mobility values for highly doped PPVs.[167] The peak conductivity of 6.9 S $cm^{-1}$ occurred at +2.0 V, and there was a hysteresis of 430 mV in the conductivity peak between the forward and reverse sweep. The onset of oxidation of P3DTV occurred at +1.15 V, and a single oxidation peak occurred +1.50 V. The peak mobility of 0.27 $cm^2$ $V^{-1}$ $s^{-1}$ and peak conductivity of 20.9 S $cm^{-1}$ occurred at +1.65 and +1.75 V respectively, with the peak mobility rivaling that of pristine unsubstituted poly(thienylene vinylene).[187] There was a relatively small hysteresis of 200 mV in the conductivity peak between the forward and reverse sweep.

All four polymers in this study displayed clear windows of finite conductivity, supporting the conclusion that with the choice of a suitably stable electrolyte, the non-monotonic transport behavior is common to semiconducting polymers. Additionally, MEH-PPV samples were prepared in a manner known to give amorphous films,[188,189] while F8BT was annealed in a manner known to give highly crystalline films,[190] showing that this behavior is not morphology specific. Thus, the general trend of an orders of

magnitude increase in mobility with increasing charge carrier density, followed by a mobility peak and a steep decrease in mobility and conductivity upon further increases in charge density, appears to be general over different chemical structures and morphologies of polymer semiconductors.

## *6.5 Conclusions*

The electrochemistry and conductivity of P3HT gated with the ionic liquid liquid [EMI][FAP] was investigated at extreme charge densities and anodic potentials. P3HT displayed a finite potential window of high hole conductivity. The potential dependent charge density was rigorously determined from cyclic voltammetry, and was used to map the electrochemical density of hole states. The mobility and conductivity were investigated across the DOS, revealing the complex dependence of hole transport on charge density. Hole mobility is vastly increased with increasing charge density up to a concentration of 0.12 holes per P3HT repeat unit, beyond which increases in charge density were detrimental to hole transport, eventually suppressing it completely. Variable temperature cyclic voltammetry and conductivity measurements reveal thermally activated hole transport that becomes very weakly activated in regions of high conductivity. The ionic liquids [EMI][TFSA], [P14][TFSA], [P14][FAP], and [P14,6,6,6][FAP] were investigated as electrolyte gates for P3HT demonstrating the important role of the anion in oxidative stability, and the role of the cation in facilitating the doping and de-doping of the P3HT. The semiconducting polymers F8BT, MEH-PPV, and P3DTV were also investigated using the [EMI][FAP] electrolyte gate, further

supporting the generality of the finite potential window of high conductivity in electrolyte gated polymer semiconductor systems.

# *7. Low-Band-Gap Poly(3-hexadecylthienylene vinylene): A Systematic Study of Molecular Weight and Photovoltaic Performance*[*†]

## *7.1 Overview*

The effect of molecular weight on organic photovoltaic device performance is investigated for a series of low band gap (ca. 1.65 eV) poly(3-hexadecylthienylene vinylene)s (C16-PTVs) prepared by acyclic diene metathesis (ADMET) polymerization. By utilizing monomers of varying cis:trans (*Z*:*E*) content seven C16-PTVs were prepared with a number average molecular weight range of 6–30 kg/mol. Polymers were characterized by size-exclusion chromatography, $^{1}$H NMR spectroscopy, ultraviolet-visible spectroscopy, thermogravimetric analysis, wide-angle X-ray scattering, and differential scanning calorimetry. C16-PTVs were integrated into bulk-heterojunction (BHJ) solar cells with [6,6]-phenyl-$C_{61}$-butyric acid methyl ester (PCBM), and conversion efficiency was found to increase with increasing molecular weight. This observation is attributable to an increase in polymer aggregation in the solid state and a corresponding increase in hole mobility. Finally, phase behavior and morphology of the C16–PTV:PCBM active layers were investigated by differential scanning calorimetry and

[*]Adapted with permission from "An ADMET Route to Low-Band-Gap Poly(3-hexadecylthienylene vinylene): A Systematic Study of Molecular Weight on Photovoltaic Performance" Joshua C. Speros, Bryan D. Paulsen, Scott P. White, Yanfei Wu, Elizabeth A. Jackson, Bradley S. Slowinski, C. Daniel Frisbie, and Marc A. Hillmyer, *Macromolecules, 2012, 45 (5), pp 2190–2199* Copyright 2012 American Chemical Society.

[†] Work carried out in conjunction with J. C. Speros, who synthesized all polymers, and carried out all NMR, SEC, TGA, TWAX and mass spectrometry characterization.

atomic force microscopy, respectively.

## *7.2 Introduction*

The promise of low-cost, solution-processable solar cells continues to motivate significant academic[191–193] and industrial research[194] in organic photovoltaics (OPVs). Optimization of both photoactive conjugated polymers and OPV architectures has led to efficiency increases from 2.5% in 2001[195] to greater than 7% in the present day.[196–200]Although contemporary devices are approaching practical maximum efficiencies of 11% theoretically predicted by Veldman et al.,[201] fundamental understanding of OPV operation and the connection to molecular parameters of the active layer components is an ongoing challenge. A particularly important parameter for OPV performance is the molecular weight of the conjugated polymer. Prior molecular weight studies have focused on OPVs utilizing poly(alkylthiophene)s (P3ATs)[202–206] and a handful of alternating donor-acceptor (D-A) polymer chain architectures.[207–209] These examples demonstrate an improvement in device efficiency, hole mobility, optical properties, and film morphology with increasing molecular weight. Expanding the scope of materials for which molecular weight influences are observed and understood is desirable.

Acyclic diene metathesis (ADMET) polymerization has been employed to prepare a wide variety of materials ranging from polyethylene derivatives[210] to conjugated polymers.[211–216] Poly(thienylene vinylene)s (PTVs) are a particularly interesting class of low band gap conjugated polymers for OPVs.[217–220] A variety of synthetic methodologies have been exploited to prepare PTVs,[221–228] with maximum OPV efficiencies reaching 2%.[229] Recently, Qin and Hillmyer detailed the synthesis of poly(3-hexylthienylene

vinylene) using ADMET polymerization in conjunction with functional group tolerant Grubbs catalysts.[230] Appreciable molecular weights (ca. 10 kg/mol) were reported, but these were only achieved after sequential catalyst additions. Realization of higher molecular weights was likely prevented by poor polymer solubility and catalyst decomposition.

Herein, we describe the ADMET preparation of seven poly(3-hexadecylthienylene vinylene) (C16-PTV) samples over a range of molecular weights (Scheme 1a). The use of a longer alkyl chain allowed for enhanced solubility at increased chain length. In addition, a more active Grubbs catalyst was utilized to reach high molecular weight at lower catalyst loadings. By addressing deficiencies in the ADMET synthesis of PTVs, we report one of the highest PTV molecular weights to date. The dependence of PTV molecular weight on charge mobility was assessed in a field effect transistor (FET) structure. These materials were then integrated into BHJ OPVs with [6,6]-phenyl-$C_{61}$-butyric acid methyl ester (PCBM) to elucidate the impact of molecular weight on performance. Finally, a temperature-composition morphology map for C16-PTV:PCBM was constructed using differential scanning calorimetry (DSC), and blend morphology was investigated with atomic force microscopy (AFM).

## *7.3 Experimental Methods*

### *7.3.1 Materials and General Methods*

Commercially available solvents and reagents were purchased and used as received from Aldrich and Acros. Degassed THF was purified by passage through an activated alumina column and collected in flame-dried, air-free flasks. All reactions were

run under argon or vacuum using standard Schlenk techniques. $^{1}H$ and $^{13}C$ NMR spectra were acquired on either a Varian INOVA 500 or 300 MHz spectrometer. Spectra were referenced internally to tetramethylsilane ($^{1}H$) or to residual solvent peaks ($^{13}C$). High resolution mass spectrometry was performed on a Finnigan MAT 95 mass spectrometer operating in EI (electron impact) mode. Samples were introduced using a solid probe. Size exclusion chromatography (SEC) analysis was performed in $CHCl_3$ (1 mL/min, 35 °C) using a Hewlett Packard (Agilent Technologies) 1100 Series liquid chromatograph equipped with three PlGel 5 μm Mixed-C (Polymer Laboratories) columns with pore sizes of 500, $1\times10^{3}$, and $1\times10^{4}$ Å. The columns were calibrated using polystyrene standards (Polymer Laboratories), and the refractive index signal was recorded with a Hewlett Packard 1047A refractive index detector.

Ultraviolet-visible (UV-Vis) absorption spectra for polymer solutions and thin films were acquired on a Spectronic Genesys 5 spectrometer over a wavelength range of 300–1000 nm. The solution spectra were obtained in a 1 cm quartz cuvette, and the film spectra were obtained by spin casting a $CHCl_3$ solution (10 mg/mL, 1500 rpm, 40 s) on a glass substrate. Elemental analysis was performed by Atlantic Microlab Inc. in Norcross, GA using combustion coupled with thermal conductivity detection. Polymer decomposition temperatures were determined by thermogravimetric analysis (TGA) using a PerkinElmer Pyris Diamond TG/DTA 6300 with aluminum sample pans. Polymer melting and crystallization transitions were quantified by differential scanning calorimetry (DSC) using either a TA Instruments Q1000 or Discovery DSC calibrated with indium. Cyclic voltammetry (CV) was run using a Pine Instruments bipotentiostat

with a Pt wire couter electrode, an Ag wire pseudo reference electrode, and Au-coated glass working electrode. C16-PTV was spin coated onto the working electrode from a 1,2-dichlorobenzene solution, and voltammograms were recorded in 1-butyl-1-methylpyrrolidinium bis(trifluoromethylsulfonyl)imide, [P14][TFSA], as the supporting electrolyte at a scan rate of 50 mV/sec. HOMO levels were estimated from the oxidation onset relative to cobaltocene using the equation: $E_{HOMO} = -q(E_{ox,\ onset\ vs.\ Cc\ o/+} + 3.75)$. Temperature-dependent wide-angle X-ray scattering (TWAXS) data was collected at various temperatures in an $N_2$ atmosphere using a Bruker D8 Advance and a temperature-controlled sample cell. Poly(3,4-ethylenedioxythiophene):poly(styrenesulfonate) (PEDOT:PSS, Clevios P VP AI 4083) aqueous dispersion and [6,6]-phenyl-C61-butyric acid methyl ester (PCBM) were purchased from Heraeus Materials Technology (West Conshohocken, PA) and American Dye Source (Baie-d'Urfé, Quebec) respectively. Atomic force microscopy (AFM) was performed on an Agilent 5500 environmental SPM with an open-loop scanner operating in tapping mode in the repulsive regime. AFM samples were prepared by spin coating a 1:4 wt% (C16-PTV:PCBM) solution in 1,2-dichlorobenzene onto a PEDOT:PSS coated glass slide.

### *7.3.2 Device Fabrication and Characterization*

Photovoltaic devices were fabricated on patterned indium tin oxide (ITO) coated glass substrates (Delta Technologies (Stillwater, MN), sheet resistance 8–12 ohms/sq), cleaned with successive acetone, methanol, and isopropyl alcohol sonications followed by an UV/$O_3$ exposure. PEDOT:PSS was spin-coated from a filtered water suspension twice at 4000 rpm, forming *ca.* 30-40 nm films as measured by profilometry (KLA Tencor P-10). Coated substrates were then transferred to nitrogen atmosphere glove box

and annealed at 135 °C for 10 minutes. All remaining fabrication steps were carried out in a $N_2$ glove box. PTV:PCBM active layers were spin-coated from 1,2-dichlorobenzene solutions, varying spin speed and concentration in order to control active layer thickness. Still wet spun devices were placed in covered Petri dishes to slowly dry. Aluminum cathodes, *ca.* 100 nm as measured by profilometry and quartz crystal microbalance, were formed via thermal evaporation at a rate of 2-3 Å/min. Silver paste was applied to the anode and cathode contact pads facilitating ohmic contact with the testing apparatus.

Bottom gate bottom contact geometry transistors were fabricated on doped Si wafers with 3000 Å of thermally grown oxide. Gold source-drain contacts, *ca.* 250 Å as measured by profilometry and quartz crystal microbalance, were deposited via electron beam evaporation (Temescal) of a 25 Å chromium adhesion layer and 225 Å of gold, and patterned via the lift-off technique. Substrates were cleaned with successive acetone, methanol, and isopropyl alcohol sonications followed by an $UV/O_3$ exposure. In a $N_2$ glove box, PTV active layers were spin-coated from 10 mg/ml 1,2-dichlorobenzene solutions at 2000 rpm, and baked on a hot plate at 105 °C for 10 minutes to drive off residual solvent.

PV current-voltage characteristics were collected using an Agilent 4155C Semiconductor Parameter Analyzer, under dark conditions and simulated solar illumination using a 150 W Xe-arc lamp (Oriel) with an AM 1.5 G filter, attenuated to 100 $mW/cm^2$. External quantum efficiency spectra were obtained using a monochromator (Cornerstone 130 1/8 m) equipped with gratings and filters (Newport Corp.) in

conjunction SRB 10 DSP lock-in amplifier (Stanford Research Systems) controlled by customized LabView code.

Transistors were tested in Desert Cryogenics vacuum probe station at room temperature housed within a $N_2$ glove box. Output and transfer curves were collected with Keithly 236, 237, and 6517A source meters controlled by customized LabView code.

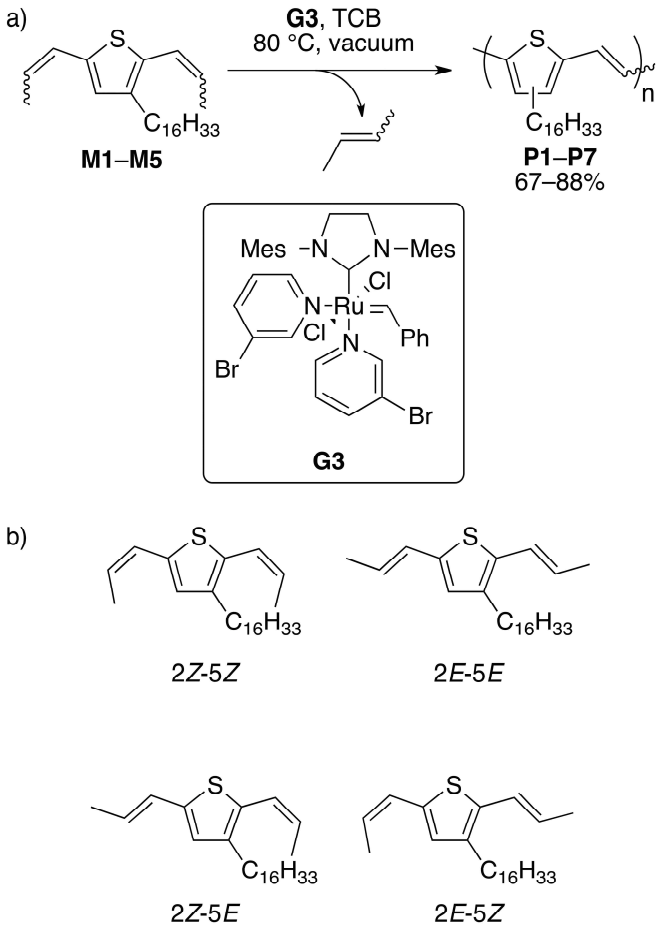


**Figure 7.1** Synthesis of (a) C16-PTVs and (b) the four isomers of M

## *7.4 Results and Discussions*

### *7.4.1 Synthesis and Characterization*

The C16-PTV monomer and corresponding polymer synthesis (Figure 7.1a) was accomplished following a previous literature report.[230] En route to optimizing the Wittig reaction for a high cis double bond content, five monomers (**M1**–**M5**) having varying distributions of the four potential isomers (Figure 7.1b) were generated. Isomer distributions were assessed by $^1$H NMR (see Figure S5 in Supporting Information), and the percentages of these isomers and overall cis:trans (*Z*:*E*) ratios are summarized in Table 1. **M1**–**M5** were prepared in three steps with overall yields as high as 67% and no detectable impurities as determined by $^1$H NMR and GC-MS. High yields coupled with synthetic simplicity make this monomer amenable to multi-gram preparation.

**Table 7.1** Monomer Isomer Ratios and Polymer Molecular Weight Values

| Polymer (Monomer) | Z:*E*[a] | A:B:C:D[b] | t (h) | $M_n$[c] (kg/mol) | PDI[c] | $X_n$[d] | $M_n$[d] (kg/mol) |
|---|---|---|---|---|---|---|---|
| P1 (M1) | 47:53 | 21:27:22:30 | 16 | 6 | 1.5 | 18 | 6 |
| P2 (M1) | 47:53 | 21:27:22:30 | 24 | 8 | 1.6 | 24 | 8 |
| P3 (M2) | 67:33 | 39:20:23:18 | 20 | 12 | 2.0 | 36 | 12 |
| P4 (M3) | 82:18 | 68:10:18:4 | 24 | 17 | 1.8 | 45 | 15 |
| P5 (M4) | 81:19 | 62:10:19:9 | 27 | 24 | 2.3 | 72 | 24 |
| P6 (M5) | 83:17 | 68:10:20:2 | 48 | 29 | 2.4 | 81 | 27 |
| P7 (M5) | 83:17 | 68:10:20:2 | 96[e] | 33 | 2.2 | 90 | 30 |

[a]Overall monomer cis:trans ratio calculated from the relative integration of *Z* and *E* protons in the $^1$H NMR spectrum. [b]A = 2*Z*-5*Z*, B = 2*Z*-5*E*, C = 2*E*-5*Z*, and D = 2*E*-5*E* as determined from integration of $^1$H NMR spectrum. [c]Determined by SEC in $CHCl_3$ with a refractive index detector and polystyrene standards. [d]Determined by $^1$H NMR analysis. [e]Reaction was determined to be complete after 48 h by SEC.

To effectively study the impact of molecular weight on device performance a series of C16-PTVs (**P1**–**P7**) was prepared by ADMET polymerization using the highly active ruthenium metathesis catalyst having an N-heterocyclic carbene and 3-

bromopyridine ligands (**G3**) developed by Grubbs.[231] **P1**–**P7** were prepared by treating **M1**–**M5** with 1 mol% **G3** in 1,2,4-trichlorobenzene (TCB). The equilibrium nature of ADMET was exploited by performing the reaction under reduced pressure to remove the 2-butene byproduct. This technique is necessary to achieve high conversion.[232,233] As stated, a small library of molecular weights was obtained by utilizing monomers having different overall *Z*:*E* ratios and by varying reaction times (Table 7.1). Given the asymmetric nature of the monomer, **P1**–**P7** are obtained as essentially regiorandom polymers. This is supported by $^{1}$H NMR analysis where the α-methylene protons on the alkyl chain appear as a broad singlet (2.6 ppm) rather than the triplet observed for regioregular thiophene polymers.[226] Additionally, Zhang et al. demonstrated the transition from four well-resolved to two broad olefinic resonances with decreasing PTV regioregularity.[234] These two broad peaks were observed in our C16-PTV samples (6.9 ppm) further supporting a regiorandom structure and thus the olefin *Z*:*E* ratio could not be accurately determined. PTV regiochemistry has been shown to have little affect on OPV performance.[234]

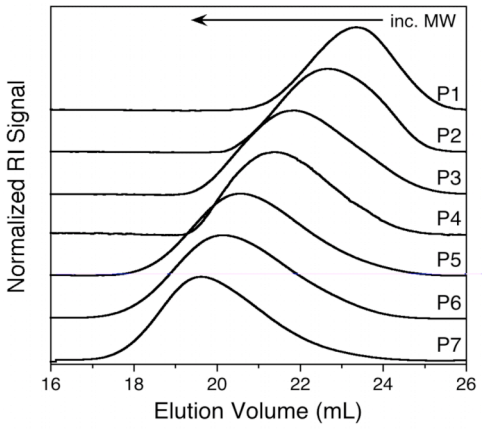


**Figure 7.2** SEC chromatograms of **P1**–**P7**.

The C16-PTV samples were slightly soluble in THF and toluene (ca. 5 mg/mL) and highly soluble in chloroform, *o*-dichlorobenzene, and TCB (> 15 mg/mL). Initial molecular weight estimates were determined using size-exclusion chromatography (SEC) in chloroform versus polystyrene standards (Figure 7.2). The polydispersity index (PDI) values trended toward 2 with increasing molecular weight as expected for ADMET polymerization. SEC overestimates molecular weight for rod-like conjugated polymers,[235,236] making alternative molecular weight characterization necessary.

Number-average molecular weight ($M_n$) values were also determined y $^1$H NMR analysis (Table 7.1). ADMET represents a step polymerization technique where appreciable molecular weights are only observed at high conversions. Using propenyl and aldehyde[40] end groups it was possible to estimate monomer conversion by comparing to polymer repeat unit resonances. Additionally, treating **G3** as a monofunctional impurity that limits polymer molecular weight, the number-average degree of polymerization ($X_n$) and $M_n$ can be determined. The molecular weights calculated using $^1$H-NMR are comparable to those from SEC but are almost certainly overestimates. Given the removal of 2-butene, some fraction of polymer chains was likely terminated on one or both ends with ruthenium. However, ruthenium ends were neither observed nor quantified leading to conversion and, ultimately, molecular weight overestimates. Also, polymer purification by Soxhlet extraction removes residual monomer and low molecular weight oligomers leading to artificially high estimates of monomer conversion.

Selected $^{1}$H NMR spectral regions of monomer and two representative C16-PTVs are shown in Figure 7.3. The absence of *Z* propenyl end groups in both polymers is indicative of their increased reactivity with **G3**. Conversely, *E* propenyl end groups persist even after 96 h of polymerization. We previously demonstrated that aldehydes residing on one or both of the polymer chain ends are the result of adventitious oxygen in the reaction solution.[230] Two aldehyde resonances, also highlighted in Figure 7.3b, occur due to monomer asymmetry. In this work, we demonstrate that a simple freeze-pump-thaw (FPT) cycle prior to catalyst loading effectively prevents aldehyde formation (Figure 7.3c). However, this additional manipulation did not lead to increased molecular weight for a given reaction time.

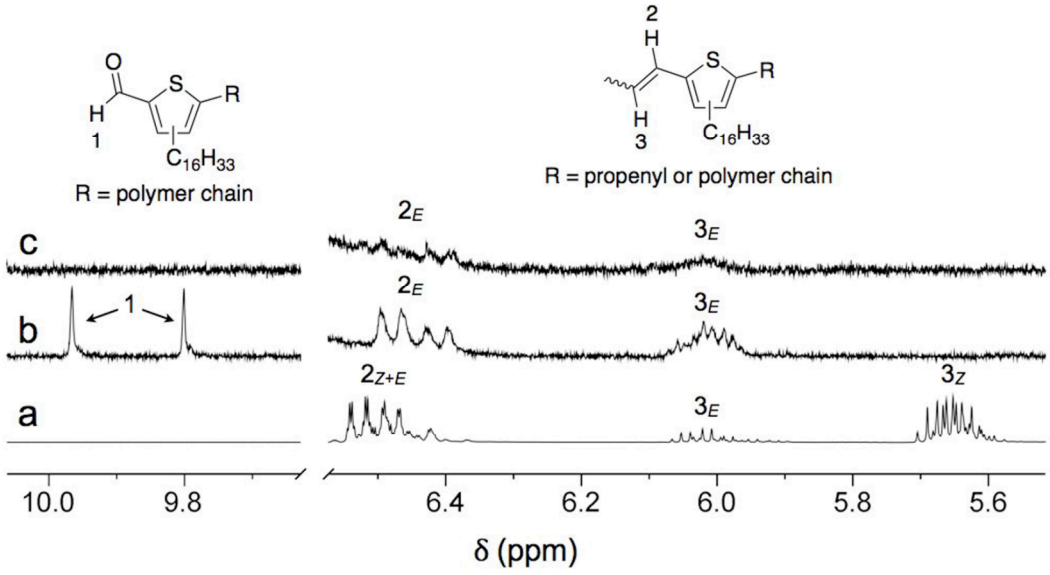


**Figure 7.3** $^{1}$H NMR spec tra of (a) monomer, (b) polymer without freeze-pump-thaw (FPT), and (c) polymer with FPT.

Biagini et al. demonstrated the deliberate end group conversion of ruthenium carbenes to aldehydes during metathesis polymerization.[237] Aldehyde end groups provide

a useful synthetic handle for further reaction and functionalization. To demonstrate this, a C16-PTV partially terminated with aldehydes was treated under McMurry coupling conditions with titanium tetrachloride and zinc in THF. Following workup, the polymer molecular weight was markedly increased (9→12 kg/mol). This is illustrated by the disappearance of aldehyde peaks in the product polymer $^{1}$H NMR spectrum and a shift to lower elution volume in the SEC chromatogram. Upon further investigation and optimization this method of chain extension could prove suitable for a variety of aldehyde-terminated conjugated polymers and make block polymerization or polymer functionalization strategies synthetically accessible.

### *7.4.2 Optical and Electrochemical Properties*

To understand the role that molecular weight plays on C16-PTV photophysical behavior, **P1**–**P7** were investigated by ultraviolet-visible (UV-Vis) absorption spectroscopy in dilute chloroform solutions and as thin films on glass substrates. Figure 7.4a summarizes the solution data for **P1**–**P7**. As molecular weight increased the absorption maximum ($\lambda_{max,1}$) red shifted (Table 7.2) indicative of an increased conjugation length. A second peak ($\lambda_{max,2}$) also appeared with increasing molecular weight. While the first peak is attributed to the $\pi$-$\pi^*$ transition, the second is indicative of vibronic structure that results from polymer aggregation. This phenomenon is well documented for conjugated polymers.[238,239] To confirm aggregation-induced absorption, solution spectra of **P5** were collected in chlorobenzene at room temperature, at ca. 130 °C, and upon returning to room temperature (Figure 7.4b). Owing to the general thermochromic nature of conjugated polymers,[240,241] there was a blue shift (14 nm) in **P5** absorption at elevated temperature. Also, the second absorption peak nearly disappeared

(i.e., reduced to shoulder) indicating the breakup of polymer aggregates. Upon cooling the original absorptive features returned suggesting the loss of aggregation induced absorption was not a product of polymer degradation at elevated temperatures.

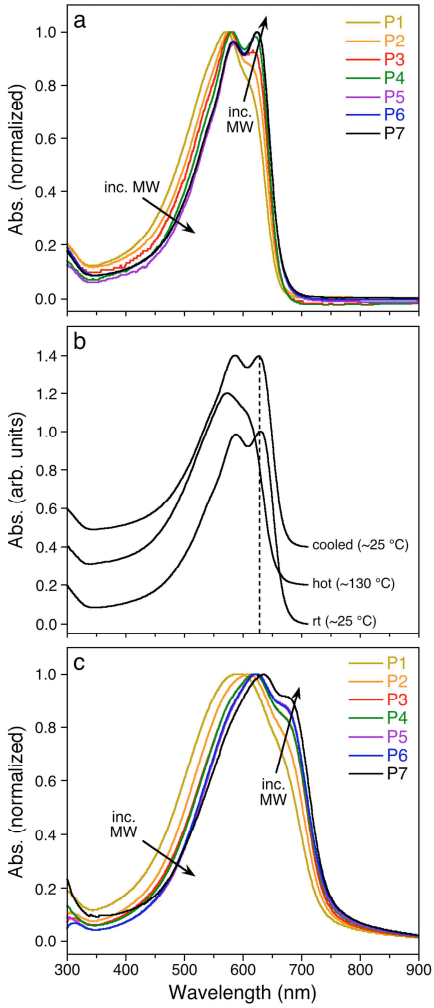


**Figure 7.4** UV-Vis spectra of (a) **P1**–**P7** in $CHCl_3$ (see Table 2 for concentrations), (b) **P5** in chlorobenzene ($1 \times 10^{-5}$ M per repeat unit), and (c) **P1**–**P7** as unannealed thin films on glass. Spectra are offset and a dashed vertical line is added in (b) to make the noted changes more evident.

**Table 7.2** UV-Vis Data for C16-PTVs.

| Entry | UV-Vis (Solution)[a] | | UV-Vis (Film)[b] | |
|---|---|---|---|---|
| | $\lambda_{max,1}$ (nm) | $\lambda_{max,2}$ (nm) | $\lambda_{max,1}$ (nm) | $E_g^{opt}$ (eV) |
| P1 | 571 | 616[c] | 592 | 1.68 |
| P2 | 576 | 617[c] | 609 | 1.66 |
| P3 | 579 | 617 | 619 (675[c]) | 1.66 |
| P4 | 581 | 621 | 619 (675[c]) | 1.66 |
| P5 | 584 | 624 | 623 (680[c]) | 1.66 |
| P6 | 584 | 624 | 623 (680[c]) | 1.66 |
| P7 | 584 | 624 | 635 (684[c]) | 1.65 |

[a]P1 = $2.5\times10^{-5}$ M (repeat unit basis) in $CHCl_3$ and P2–P7 = $1.0\times10^{-5}$ M (repeat unit basis) in $CHCl_3$. [b]Films prepared by spin-coating a 10 mg/mL polymer solution in $CHCl_3$ at 1500 rpm for 40 s. [c]Absorption shoulder.

Indicative of increased ordering in the solid state, a significant red shift (21–51 nm) was observed in going from solution to thin film spectra (Figure 7.4c). Vibronic structure was also apparent for **P1**–**P7**, and the associated absorption intensity increased with increasing molecular weight. The optical band gap ($E_g^{opt}$) of these materials was calculated by converting the onset absorption ($\lambda_{onset}$) to energy ($E_g^{opt} = 1240/\lambda_{onset}$) and ranged from 1.65–1.68 eV (Table 7.2).

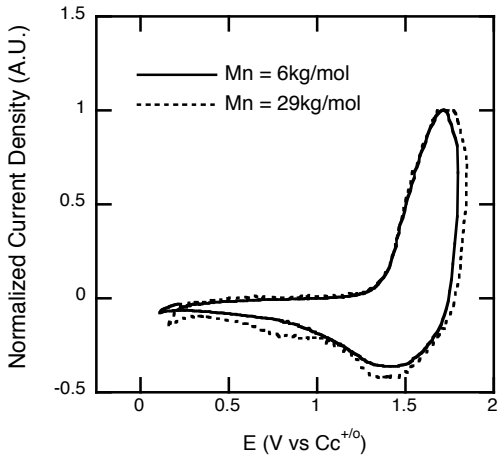


**Figure 7.5** Cyclic voltammograms of **P1** (6 kg/mol) and **P6** (29 kg/ mol) films in [P14][TFSA] ionic liquid electrolyte referenced to the cobaltocenium redox couple.

Cyclic voltammetry, Figure 7.5, of thin films of **P1** and **P6** in ionic liquid electrolyte was also used to calculate their respective HOMO levels from the oxidation onset. Despite the difference in molecular weight, 6 and 29 kg/mol, both samples displayed an identical onset of oxidation occurring at 1.35 V vs $Cc^{o/+}$. Additionally both displayed a single broad oxidation, peaking around 1.7 V. On the reverse scan both the high and low molecular weight samples shared a broad reduction centered about 1.4 V, but the 29 kg/mol sample displayed a smaller reduction feature around 0.8 V. Due to the high stability of the ionic liquid electrolyte the cyclic voltammograms of both samples displayed excellent sweep-to-sweep reproducibility. While the charging (oxidation) of the film seemed independent of the high degree of aggregation present in the **P6** film, the additional discharging (reduction) peak would suggest that charge is retained (trapped) in the ordered regions of the higher molecular weight sample.

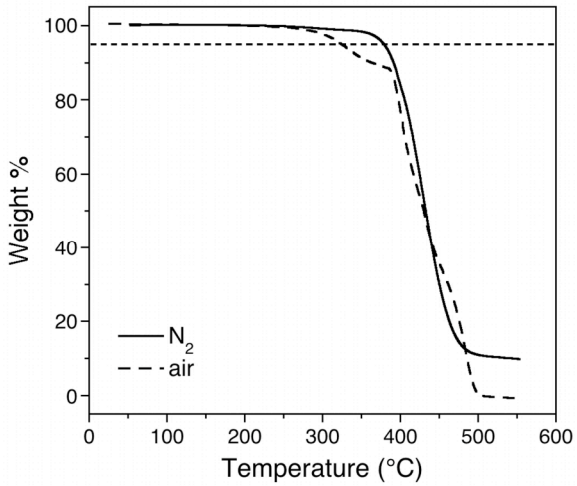


**Figure 7.6** Thermogravimetric analysis of **P7** in an $N_2$ and oxidizing (air) atmosphere. Decomposition temperature ($T_d$) was de termined as the temperature where 5% of the polymer weight (dashed line) was lost.

### *7.4.3 Thermal Behavior*

Thermogravimetric analysis (TGA) was employed to evaluate polymer thermal stability. Molecular weight was found to have no impact on decomposition temperature ($T_d$) as all polymers displayed 5% weight loss at 379 °C under a nitrogen atmosphere. **P7** was also analyzed in air (Figure 7.6). Although the presence of oxygen reduced the $T_d$ to 324 °C, these C16-PTVs exhibited good thermal stability regardless of molecular weight.

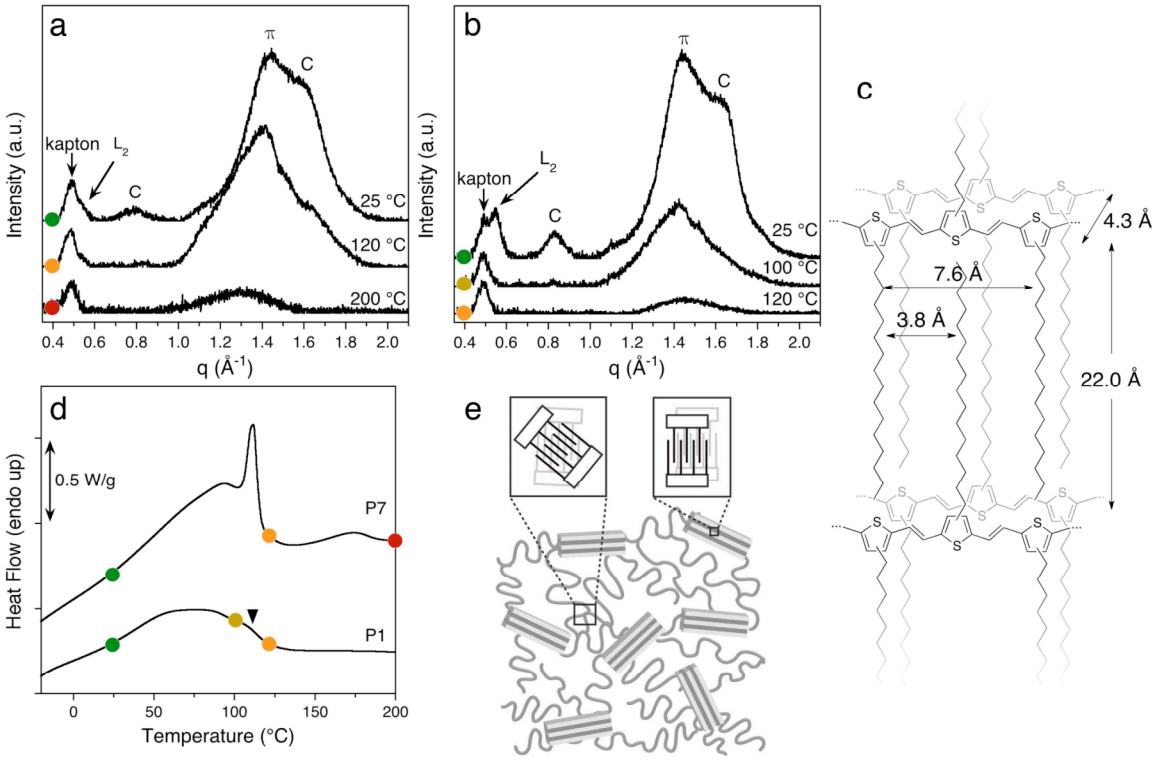


**Figure 7.7** TWAXS patterns at various temperatures for (a) **P7** and (b) **P1**. $L_2$ is the second order lamellar reflection, C is both intra- and intermolecular chain-to-chain spacing, and π is the π- spacing. (c) Schematic illustration of C16-PTV crystalline domain with lamellar (22.0 Å), chain-to-chain (7.6, 3.8 Å), and π-stack spacings (4.3 Å) determined from WAXS. (d) DSC thermograms (heating, 10 °C/min) of **P1** and **P7**. The arrowhead on **P1** marks the shoulder due to π-stack melting. The colored circles indicate the TWAXS temperatures shown in (a) and (b). (e) Schematic illustration of C16-PTV microstructure with insets highlighting interdigitation in non-π-stacked (left) and π-stacked domains (right).

Temperature-dependent wide-angle X-ray scattering (TWAXS) was employed in conjunction with differential scanning calorimetry (DSC) to elucidate the solid state behavior of C16-PTVs as a function of molecular weight (Figure 7.7). Peak assignments in the TWAXS data (Figure 7.7a & b) were made based on WAXS analysis of polymer thin films at 25 °C (Figure 7.8). The reflection at 0.58 $Å^{-1}$ was ascribed to the second order lamellar spacing ($L_2$) as a result of alkyl side chain interdigitation. Although the primary lamellar reflection ($L_1$) was outside the measurable q-range for the TWAXS instrument, it was observed by thin film analysis. The position of the $L_1$ reflection gave a spacing of 22.0 Å (Figure 7.7c) that was generally consistent with WAXS of PTVs[220,234] and crystalline hexadecane.[242] The reflections at 0.83 $Å^{-1}$ (7.6 Å) and 1.64 $Å^{-1}$ (3.8 Å) were attributed to the intra- and intermolecular side chain-to-side chain spacings (C), respectively. The somewhat broad nature of these reflections was expected given the regiorandom nature of the polymer backbone. Finally, the reflection at 1.47 $Å^{-1}$ (4.3 Å) was assigned to the π-stack spacing (π) consistent with PTV literature.[224]

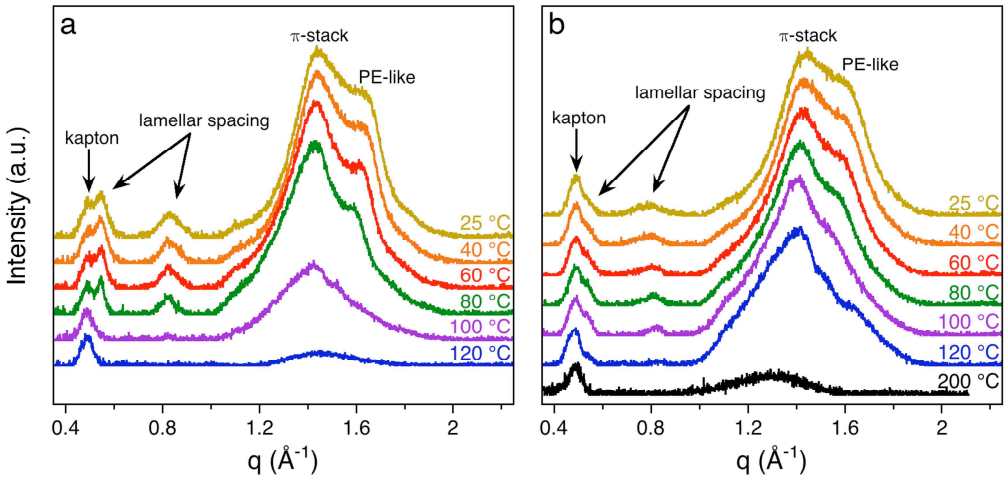


**Figure 7.8** Powder WAXS of (a) **P1** and (b) **P7** at various temperatures. PE refers to polyethylene.

On heating **P7** to 120 °C, the $L_2$ and C reflections were significantly suppressed (Figure 7.7a) and at 200 °C the π-stack reflections were very weak. Three thermal transitions were evident in the DSC thermogram of **P7** (Figure 7.7d). The first, a broad transition centered on ca. 90 °C, was ascribed to the melting of alkyl side chains in non-π-stacked (disordered) polymer regions. The breadth of this transition suggested a large distribution in the degree of chain order (interdigitation).[243] The second sharper transition at 110 °C was ascribed to side chain melting in π-stacked (ordered) polymer regions. The absence of $L_2$ and C reflections at 120 °C supports these DSC assignments. Figure 4e shows a schematic representation the two types of side chain environments. The transition at ca. 175 °C was assigned to the melting of polymer π-stacks, and is consistent with the diminished π-stack reflection at 200 °C. Based on literature precedent, we posit that the polymer is in a liquid crystalline state at temperatures above complete side chain melting (> 110 °C) and below melting of the π-stacks (ca. 175 °C).[244]

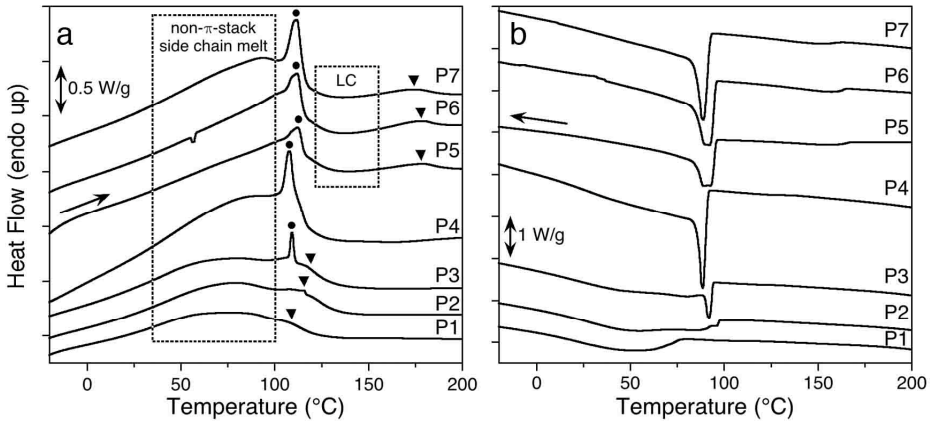


**Figure 7.9** DSC (a) second heating and (b) first cooling thermograms of **P1–P7**. All sweeps were per formed at 10 °C/min. LC denotes the liquid crystalline region. Sweep direction (arrows), π-stack side chain melt (circles), and π-stack melt (triangles).

TWAXS (Figure 7.7b) and DSC (Figure 7.7d) data for the low molecular weight **P1** were distinct from the corresponding data acquired for **P7**. $L_2$ and C reflections for **P1** were absent at 100 °C and near complete loss of the π-stack reflections was evident at 120 °C. From the DSC data, the broad transition attributed to side chain melting in more disordered regions of the polymer was centered at about 60 °C as compared to 90 °C for **P7**. Furthermore, in **P1** there was no sharp transition corresponding to side chain melting in well-organized regions as observed at 110 °C for **P7**. Finally, the π-stack melting was about 65 °C lower than the corresponding melting transition in **P7**. Taken together, the higher transition temperatures for the higher molecular weight **P7** suggest that increased molecular weight enhances the overall thermal stability of polymer crystallites (Figure 7.9). This enhancement in polymer ordering with molecular weight is consistent with observations from UV-Vis spectroscopy (Figure 7.4c).

### *7.4.4 Hole Transport Properties*

Field effect transistor measurements were employed to study the influence of molecular weight on the hole transport of neat polymer films. **P1**–**P6** exhibited transistor behavior with output curves (Figure 7.10a & b) displaying clear saturation behavior and very low hysteresis, and transfer curves (Figure 7.10c) showing ON/OFF ratios of $10^3$ or greater and modest hysteresis.

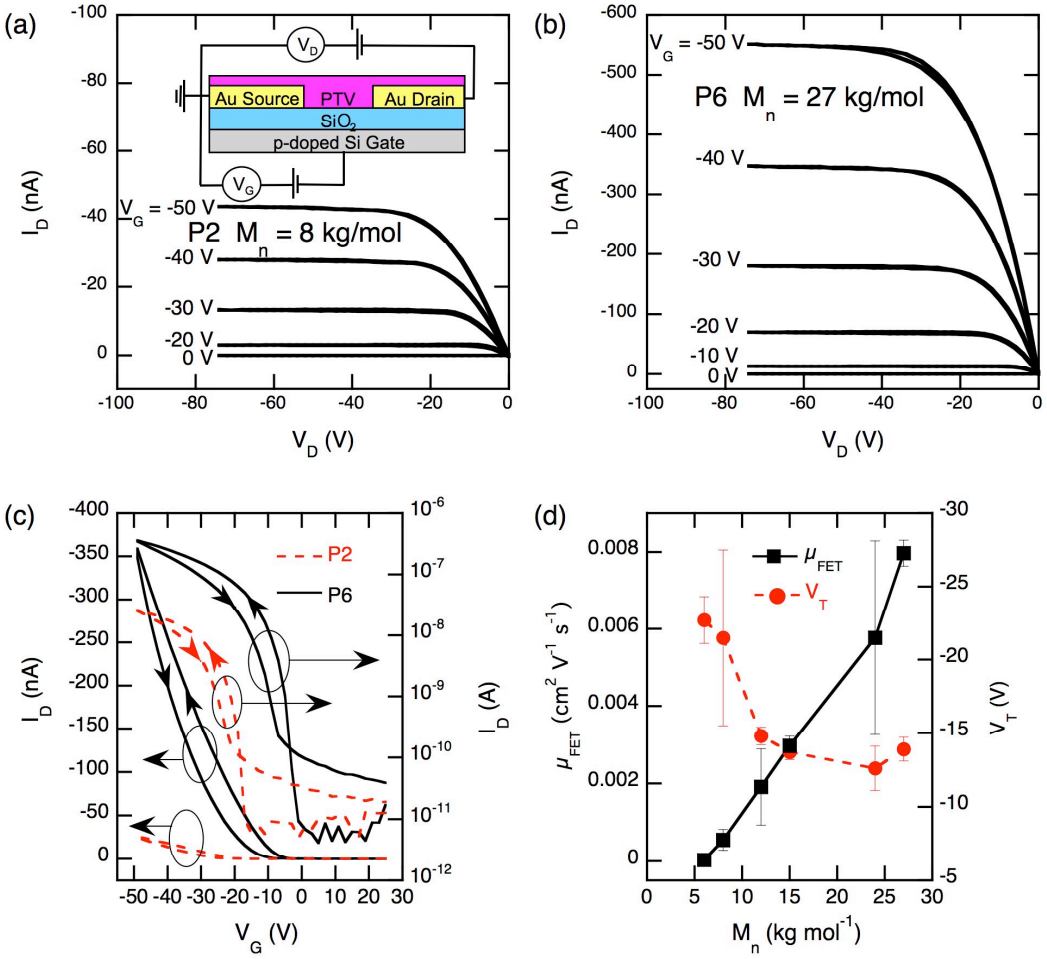


**Figure 7.10** Output curves of (a) **P2** and (b) **P6** FETs with $V_G$ varied from 0 to -50 V. Inset (a): device schematic. (c) Linear and semi-log transfer curves of **P2** and **P6** FETs with $V_D$ held at -10 V. (d) $M_n$ dependence of FET hole mobility and threshold voltage of **P1**–**P6** (error bars one standard deviation).

Hole mobility values were extracted from transfer curves of devices operated in the linear regime (i.e., transistor is "on" and gate bias exceeds the drain bias). In this regime the hole mobility may be calculated as follows:

$$\mu = \frac{L}{WC_{OX}V_D}\frac{\partial I_D}{\partial V_G}$$

Where $L$ and $W$ are the respective length and width of the conducting channel, $C_{OX}$ is the capacitance of the gate dielectric, $V_D$ is the applied drain bias, $V_G$ is the swept gate bias, and $I_D$ is the measured drain current.

Figure 7.10d plots FET hole mobilities against molecular weight, clearly showing that higher molecular weight allows for much more efficient hole transport. **P1** ($M_n$ = 6.0 kg/mol) exhibited a low FET mobility of only $3.1 \times 10^{-5}$ cm$^2$/V·s, while **P6** ($M_n$ = 27.0 kg/mol), having a number average molecular weight over four times that of **P1,** showed well over a two order of magnitude increase in FET mobility ($8.0 \times 10^{-3}$ cm$^2$/V·s). This improvement in carrier mobility and transistor performance with increasing polymer molecular weight has been previously established.[204,245,246] **P2** exhibited a hole mobility of $5.5 \times 10^{-4}$ cm$^2$/V·s, consistent with the report of Kim et al. for hexyl substituted PTVs with a similar number of repeat units.[220]

In addition to hole mobility dependence on molecular weight, FET measurements also revealed a molecular weight dependence on threshold voltage ($V_T$). Generally, increasing molecular weight leads to a less negative $V_T$, although this trend appeared to plateau for higher molecular weight (> 10 kg/mol). A large negative $V_T$ is commonly attributed to an increased trap density, implying that the low molecular weight samples have a higher trap density than the high molecular weight samples, which is also consistent with the mobility trend. Both the hole mobility and threshold voltage dependence on molecular weight are attributed to preferential ordering and increased electronic coupling, which is evident in the aggregation-induced vibronic structure in the solution and film UV-Vis spectra (Figure 7.4).

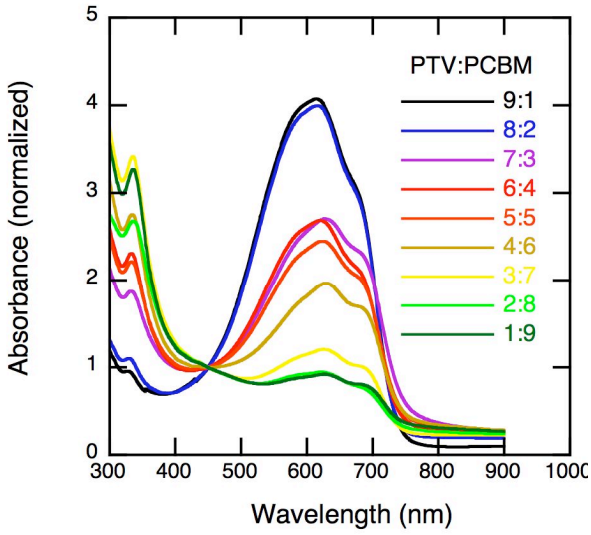


**Figure 7.11** UV-Vis spectra of **P7**:PCBM containing 10-90% PCBM.

### *7.4.5 Polymer Fullerene Blend Optical Properties*

Especially important for photovoltaic applications is the optical properties of the electron donating conjugated polymer blended with a fullerene acceptor. UV-Vis spectra, Figure 7.11, of films with varied **P7**:PCBM ratios were collected displaying absorption peaks and relative absorption strengths of both component. At all blend ratios, PCBM displayed peak absorption at 335 nm. The position of the both the main and vibronic polymer peak where consistent with that of the neat polymer, Figure 7.4, with both peaks persisting even at dilution in 90 wt% PCBM. At a 50:50 **P7**:PCBM ratio the absorbance maxima of both components revealing a equivalent peak absorption coefficient of the two materials.

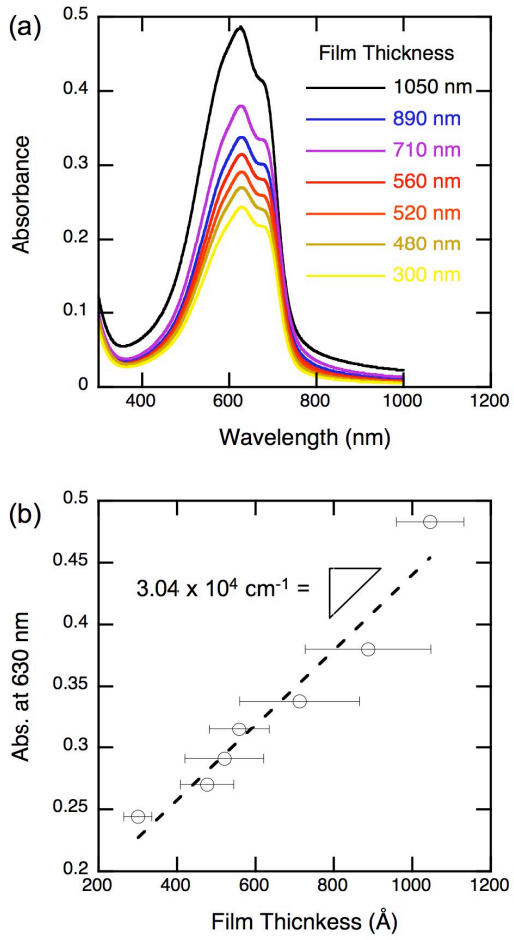


**Figure 7.12** (a) UV-Vis spectra of **P6** films with various thickness and (b) plot of absorbance vs. film thickness as $\lambda$ = 630 nm from which absorption coefficient was extracted.

The absolute absorption coefficient of **P7** at peak absorbance was determined by collecting UV-Vis spectra of thin films with varied thickness, Figure 7.12. The extracted absorption coefficient was found to be 3.04 x $10^4$ $cm^{-1}$ at 630 nm. Finally, UV-Vis spectra of the entire polymer series blended in a 1:4 ratio with PCBM were collected, Figure 7.13. As with the neat polymer, the blends showed the same suppression of the vibronic feature with decreasing molecular weight. Additionally, the loss of the vibronic absorption resulted in a moderate overall loss of absorption strength. The same structural

effects due to molecular weight that so drastically influenced charge transport, are still readily observed when blended with PCBM. Thus it is expected that molecular weight should have an equally strong effect on photovoltaic performance.

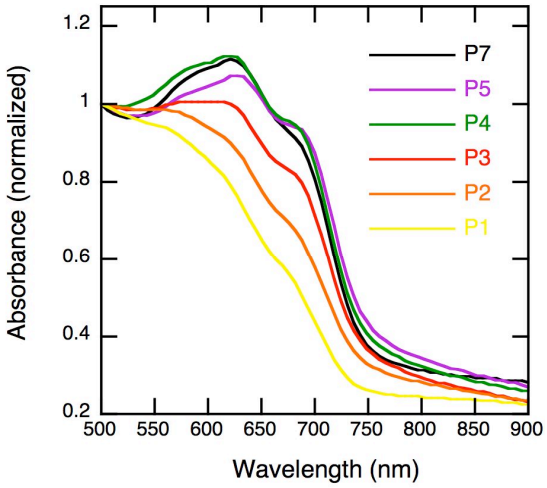


**Figure 7.13** UV-Vis spectra of 1:4 PTV:PCBM containing **P1–P5** & **P7**.

### *7.4.6. Solar Cell Performance*

**PX**:fullerene BHJ devices were fabricated in a basic ITO/PEDOT:PSS/**PX**:PCBM/Al structure (inset Figure 7.14a). Employing **P7**, the devices were optimized for maximum power conversion efficiencies (PCE) by varying thickness and active layer composition. Highest efficiencies were found for a **P7**:PCBM ratio of 1:4 and an active layer thickness of 100–150 nm. 17 devices incorporating ~150 nm thick 1:4 **P7**:PCBM blends gave a PCE of 0.80 ± 0.06 %, short-circuit current densities ($J_{sc}$) of 3.32 ± 0.28 mA/cm$^2$, and open-circuit voltages ($V_{oc}$) of 0.40 ± 0.05 V under 100 mW/cm$^2$ simulated AM 1.5 spectrum. A high fill factor (FF) of 0.60 ± 0.03 implies good diode-like behavior. A device schematic and representative *J-V* curve are shown in Figure 7.14a. Likewise, *J-V* measurements carried out in the dark revealed good

diode behavior with a rectification ratio of 1600 between +1 and -1 V shown in Figure 7.14b.

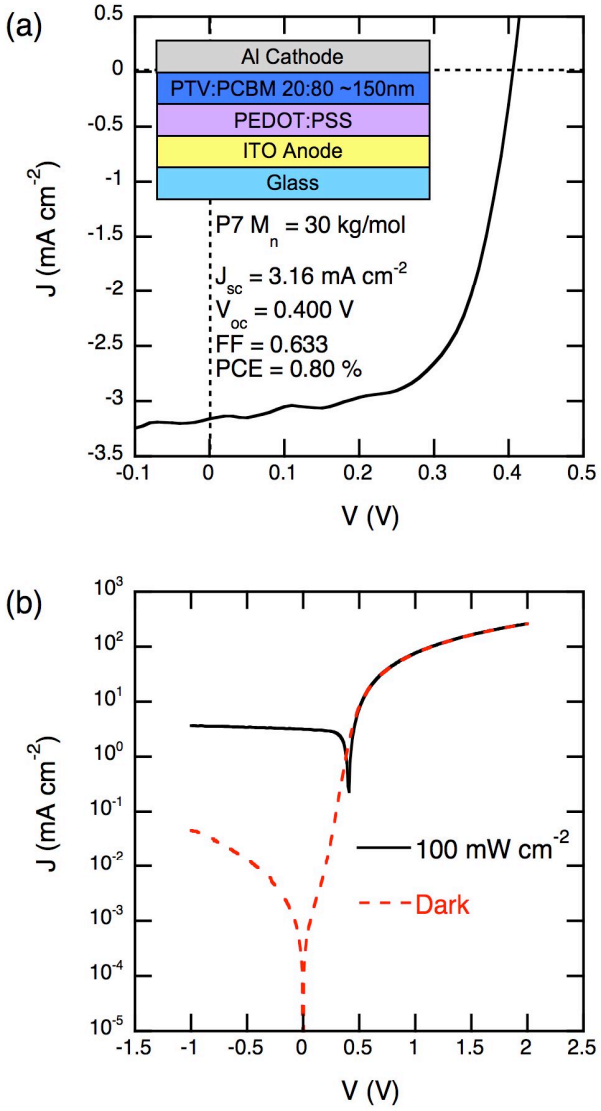


**Figure 7.14** Optimized **P7** PTV:PCBM 20:80 solar cell *J-V* characteristics under simulated AM 1.5 spectrum plotted on (a) a linear scale and (b) a semi-log scale with corresponding dark diode curve.

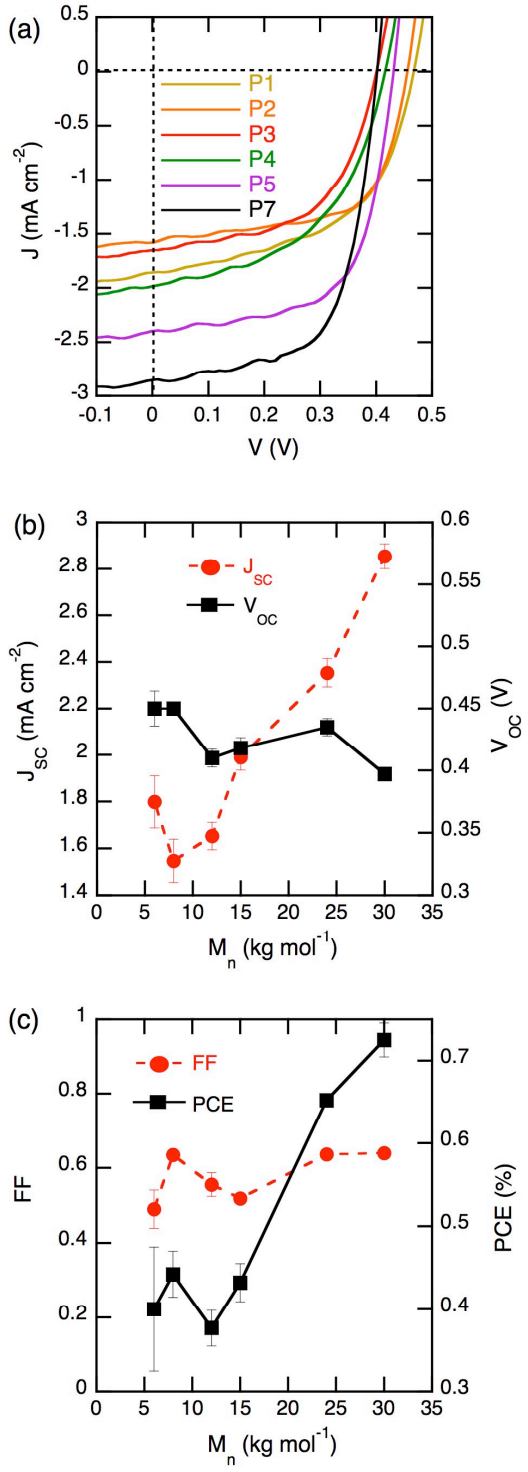


**Figure 7.15** $M_n$ dependence of ca. 100 nm thick PTV:PCBM 20:80 solar cells: (a) J-V characteristics, (b) $J_{sc}$, $V_{oc}$, (c) FF, and PCE of **P1–P7** under simulated AM 1.5 spectrum.

To investigate the polymer molecular weight effect on solar cell performance, a series of devices with ca. 100 nm thick 1:4 **PX**:PCBM active layers were tested. Figure 7.15a shows representative *J-V* curves for each of the polymers investigated, with the clearest feature being the increase in photocurrent densities when going from **P1** to **P7**. $V_{oc}$ and FF (Figures 7.15b & c) showed weak molecular weight dependence, with $V_{oc}$ decreasing slightly and FF increasing slightly with molecular weight. $J_{sc}$ was strongly dependent on molecular weight (Figure 7.15b), with highest molecular weight devices showing roughly twice the $J_{sc}$ of the lowest molecular weight devices. The strong $J_{sc}$ dependence on molecular weight dominates overall device performance, thus the PCE dependence on molecular weight mirrors the $J_{sc}$ dependence. The shunt and series resistance extracted from the dark diode curves did not display a clear dependence on PTV molecular weight.

The PCE variation with molecular weight correlated well with the hole mobility observations, suggesting that the transport of dissociated holes is a limiting factor in device performance. The PCE and mobility trends with molecular weight are also correlated with the thin film structure as assessed by UV-Vis. That is, even in composite films containing 80 wt% PCBM there is still systematic evidence of increased aggregation at high molecular weight that should favor enhanced hole mobility and thus higher $J_{sc}$.

One disadvantage of C16-PTV is its relatively weak light absorption, having an absorption coefficient of ca. $3.0 \times 10^4$ $cm^{-1}$ at peak absorption (630 nm). This value is considerably lower than that of the benchmark polymer regioregular P3HT,[247] which at

peak absorption exceeds $1 \times 10^5$ $cm^{-1}$.[248,249] This low absorption of C16-PTV results in most absorption and exciton formation occurring on the PCBM, at optimum device compositions, and undermines the benefits of employing a low band gap material. This is born out in low incident photon current efficiency at wavelengths of polymer absorption, (Figure 7.16) and illustrates the need for PTV derivatives that absorb more light to achieve higher PCE. For example, PTVs incorporating carboxylate groups have shown photoluminescent behavior resulting in higher PCE ascribed to increased excited state lifetime.[229] Our work would suggest that increasing the molecular weight of such substituted PTVs would lead to significant increases in device performance.

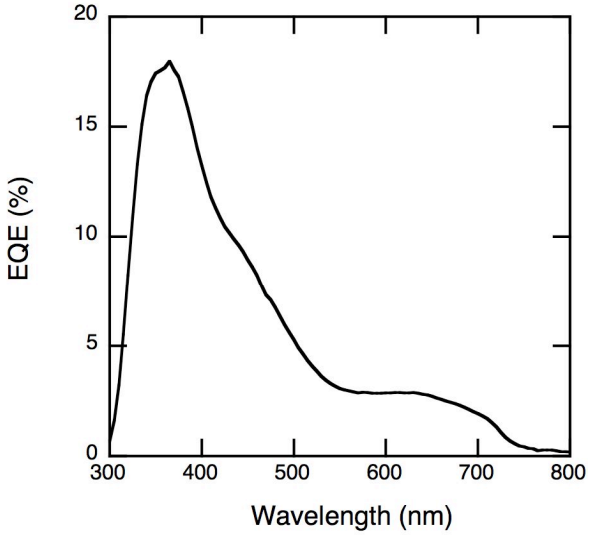


**Figure 7.16** External quantum efficiency of 1:4 **P6**:PCBM device.

### *7.4.7 Phase Behavior and Morphology*

In BHJ solar cells, the active layer phase behavior and morphology is of utmost importance, but only recently have polymer:PCBM temperature-composition phase diagrams been proposed.[250,251] Several groups have since investigated the phase behavior

of a variety of polymer:fullerene systems using various thermal, microscopy, and spectroscopy techniques.[252–256] While not strict equilibrium phase diagrams, these studies have provided practical morphology maps pertinent to the device fabrication and testing timescale. To assess the phase behavior of our active layer blends, DSC thermograms were collected for PTV:PCBM blends with varying composition and polymer molecular weight.

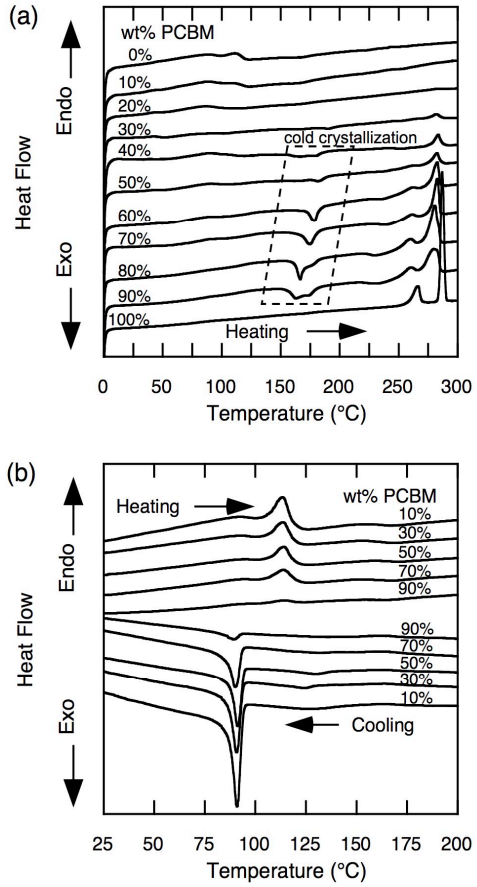


**Figure 7.17** DSC thermograms of **P7**:PCBM at a scan rate of 10 °C/min: (a) second heating of blends up to 300 °C (above PCBM melting transition); (b) first cooling and second heating of blends heated to 225 °C (below PCBM melting transition).

The effect of PCBM composition on thermal behavior was investigated using **P7**. Figure 7.17a shows second heating sweeps (0 to 300 °C) of **P7**:PCBM blends as a function of composition after initially heating the samples to 300 °C and cooling to 0 °C. At PCBM concentrations ≥ 30 wt% PCBM cold crystallization (150–200 °C) and melting transitions (250–290 °C) were observed. **P7**:PCBM blends displayed consistent PCBM melting transition temperatures independent of PTV concentration (Figure 8). These data indicate the presence of a pure crystalline PCBM phase in blends containing more than 30 wt% PCBM and dissolved PCBM in blends containing less than 30 wt% PCBM. The integrated area of the PCBM crystal melting peaks for each blend, relative to the peak areas of pure PCBM, gave the fraction of crystalline PCBM present. The fraction of a pure crystalline PCBM phase was determined at each composition by applying the lever rule.[248] By this analysis, the PCBM solubility limit was found to be 27.5 ± 3.8 wt% in **P7**.

When blends containing more than 30 wt% PCBM were heated to 300 °C no PCBM recrystallization was evident upon cooling at 10 °C/min. This lack of recrystallization was attributed to a quenching of the **P7**:PCBM blends in a glassy phase upon cooling. This is further supported by the suppression (in enthalpy) of all (i.e., recrystallization and melting) PTV transitions. Cold crystallization (150–200 °C) of PCBM was observed during the second heating from 0 °C at 10 °C/min. This PCBM cold crystallization has been observed previously.[251–253,255] To substantiate the kinetic trapping of the blends in a glassy state, **P7**:PCBM blends were first cycled from 0 °C to 300 °C to 0 °C at 10 °C/min. The blends were then heated to 225 °C at 10 °C/min, above the

temperature of PCBM cold crystallization. The following cooling to 0 °C and heating to 225 °C (both at 10 °C/min) demonstrated the recovery of PTV transitions.

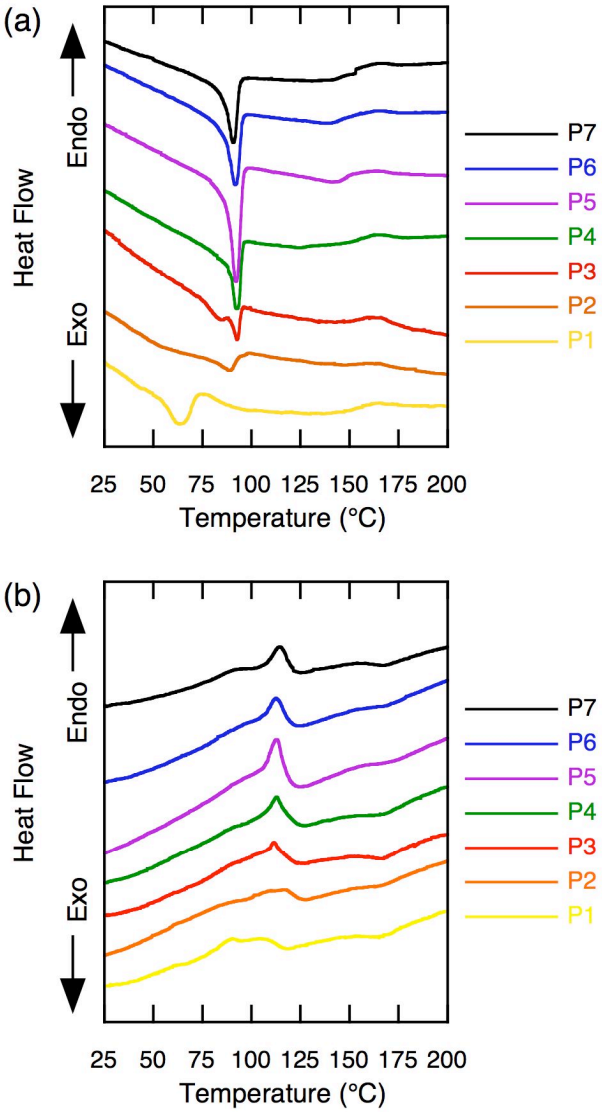


**Figure 7.18** DSC thermograms of **P1-P7** in 1:4 PTV:PCBM blends at a scan rate of 10 °C/min: (a) first cooling; (b) second heating.

To assess the polymer thermal behavior in the **P7**:PCBM blends, DSC thermograms were collected between 0 and 200 °C (Figure 7.17b), well below the PCBM melting transition. As shown, the polymer side chain melting (ca. 90 and 114 °C) and

crystallization (90 °C) transitions characteristic of neat **P7** were observed even at excessive polymer dilution. Similarly, all polymer molecular weights in 1:4 blends with PCBM displayed thermograms consistent with their respective neat polymer (Figure 7.18). The lack of **P7** melting point depression suggests the persistent presence of pure π-stacked domains regardless of PCBM composition, with any dissolved PCBM residing in non-π-stacked PTV domains. Due to the large overlap of the PCBM cold crystallization (ca. 150–200 °C) with the PTV π-stack melting (ca. 175 °C), the temperature of the π-stack transition in the **P7**:PCBM blends was not strictly assigned.

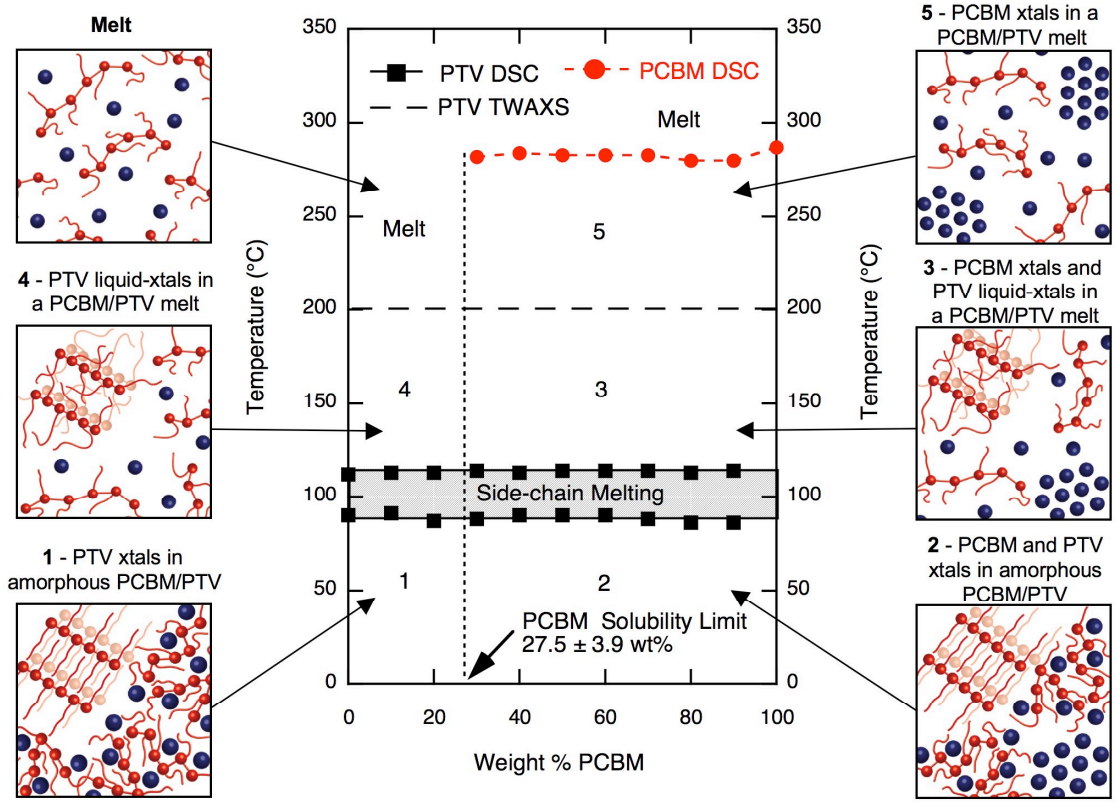


**Figure 7.19** Temperature-composition morphology map for the **P7**:PCBM system with illustrations of the various regions of phase coexistence.

The thermal and crystallographic data revealed the existence of several distinct regions of phase coexistence depending on temperature and composition (Figure 7.18 illustrations). Using the assigned polymer and PCBM melting transitions, in combination with neat PTV TWAXS and PCBM solubility calculations, a temperature-composition morphology map was generated (Figure 7.19). This morphology map represents the phase behavior that is stable over timescales related to fabrication and characterization of these BHJ devices. Below the polymer side chain melting transitions and the PCBM solubility limit, there exists two-phases: non-π-stacked polymer/PCBM and π-stacked polymer crystallites, denoted as region 1 in Figure 9. Above the PCBM solubility limit, excess PCBM crystallizes creating a third phase of crystalline PCBM in addition to non-π-stacked polymer/PCBM and π-stacked polymer crystals, region 2.

Above 114 °C and at PCBM compositions exceeding the solubility limit, the polymer side chains are completely melted resulting in liquid crystalline polymer, in equilibrium with a polymer/PCBM melt and crystalline PCBM, region 3. Above 114 °C and below the PCBM solubility limit there exists only liquid crystalline polymer and the polymer/PCBM melt, region 4. As evidenced by TWAXS, above 200 °C polymer π-stacking is disrupted resulting in a single melt for PCBM compositions below the solubility limit (labeled 'melt'). Above the PCBM solubility limit, PCBM crystallites are present in a polymer/PCBM melt, region 5. Finally, above ca. 280 °C, all components form a melt.

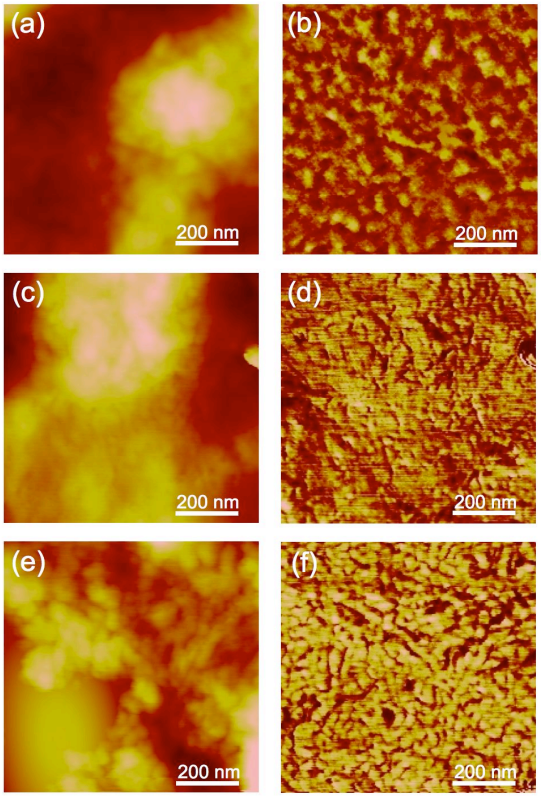


**Figure 7.20** AFM (height, phase) images of **P7**:PCBM 20:80 (a, b), 35:65 (c,d ), and 50:50 (e,f) blends.

Extrapolating from the **P7** morphology map, and taking into consideration the thermograms of the entire molecular weight series blended with PCBM (Figure 7.18), we would expect a very similar morphology map at each molecular weight. However, since **P1-4** lacked any liquid crystal transistions, liquid crystal phases (3 & 4 in Figure 7.19) would not be expected.

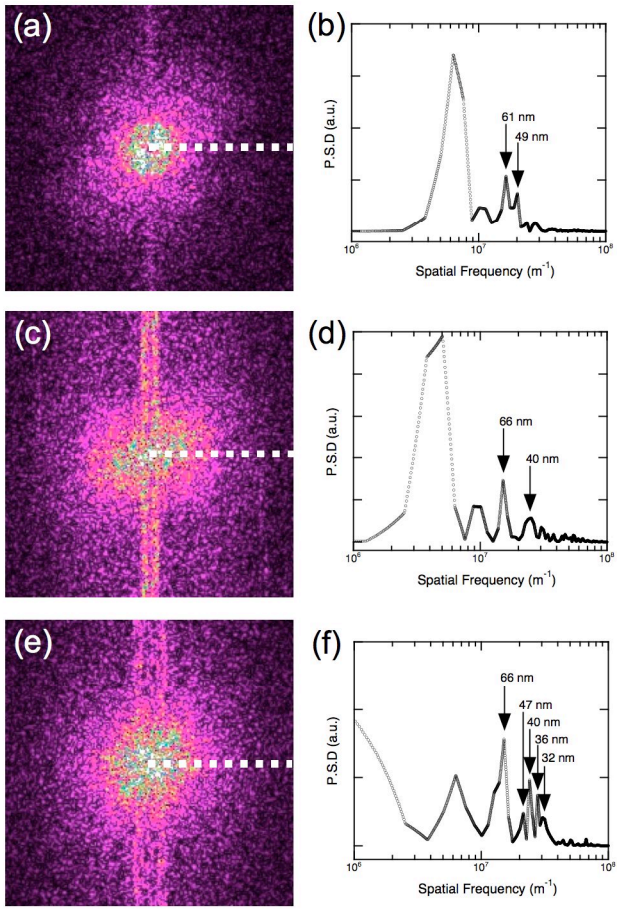


**Figure 7.21** Fourier transform of AFM phase image and P.S.D plot of 20:80 (a & b), 35:65 (c & d), and 50:50 (e & f) **P7**:PCBM samples.

To assess the length scale of the phase separation, the morphology of active layer blends was investigated using AFM. Height and phase images of 20:80, 35:65, and 50:50 **P7**:PCBM samples prior to Al deposition were collected (Figure 7.20), with the phase images revealing the nanoscale segregation. A fast Fourier transform (FFT) analysis of the phase images was employed to estimate the length scale of the PTV/PCBM phase separation (Figure 7.21).[257,258] The FFT analysis revealed characteristic domain spacings on the order of several tens of nanometers, with the minimum domain spacing of ~50 nm in the 20:80 **P7**:PCBM sample decreasing to ~40 nm in the 35:65 sample, and further

decreasing to ~30 nm in the 50:50 sample. Likewise, images were collected on a similar sample using low molecular weight **P1** (20:80) (Figure 7.22). The **P1** sample showed similar PCBM segregation with a minimum domain size of ~35 nm, estimated from FFT.

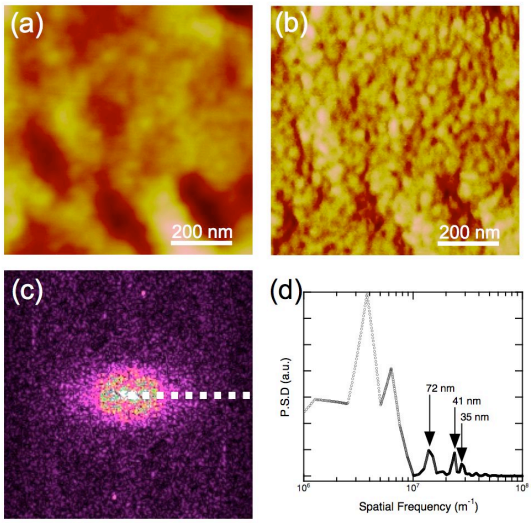


**Figure 7.22** AFM (a) height and (b) phase images of 1:4 **P 1**:PCBM. (a) Fourier transform of AFM phase image and (b) P.S.D plot.

The existence of nanoscale segregation of the donor and acceptor materials is key as exciton diffusion lengths are on the order of 10 nm. The coarsening of the phase segregation with increasing PCBM concentration might be expected to lead to decreased photocurrent density and diminished device performance; however, the opposite is observed to be true. The optimum device active layer composition of 80 wt% PCBM reflects the importance of light absorption and exciton formation, which occurs predominantly on PCBM. Employing a PTV derivative with increased light absorption or photoluminescence would likely shift the optimum PCBM composition closer to the PCBM solubility limit.

## *7.5 Conclusion*

A series of well-defined C16-PTVs was prepared using ADMET polymerization and integrated in BHJ OPVs for a systematic molecular weight investigation. By varying the monomer *Z*:*E* ratio, using a more active catalyst (**G3**), and optimizing polymerization conditions a broad range of molecular weights (6–30 kg/mol) was accessed. PCE increased with chain length, reaching a maximum efficiency of 0.80% with **P7**, which was predominantly the result of an enhanced $J_{sc}$. This observation was corroborated by FET results, which showed a molecular weight dependent increase in hole mobility brought on by enhanced polymer aggregation. A DSC-based temperature-composition morphology map was also constructed giving a PCBM solubility limit of ca. 28%. We consider this phase behavior to be paramount in assigning the long-term stability of C16-PTV:PCBM films.

ADMET has proven useful in the controlled synthesis of PTVs and has made fundamental molecular weight and phase behavior studies possible. We believe that studies of this nature will contribute to the basic understanding of conjugated polymer behavior and will lead to the development of improved devices and efficiencies. Additional systematic studies of conjugated polymers prepared by ADMET are currently underway.

# *8. Future Work*

There remains a great breadth of potential experimental directions related to the electrochemical characterization of charge transport behavior and electronic structure of π-conjugated polymers. However, there are some specific research directions that have been especially primed by this thesis research. These include extending the charge transport studies of Chapter 6 to include the investigation of field dependent charge transport behavior, and an expansion of the vinyl copolymer and poly(thienylene vinylene) based photovoltaic studies of Chapters 5 and 7.

## *8.1 Field Dependence of Electrical Conductivity in Ionic Liquid Gated Conjugated Polymers*

In electrochemically doped conjugated systems, the field dependence of conductivity at high charge carrier density has not been thoroughly studied. Yet, understanding the field dependent behavior, especially when coupled with temperature dependent studies, is a key in elucidating the over all process of charge transport. Such experimental data would be especially useful in confirming or refining theoretical models. However, these measurements have not been often carried out due to the practical limitations of working with electrochemical systems. Here we discuss experimental routes to overcome these limitations, the consequences of the experimental choices, and the effects that must be considered to interpret the results.

### *8.1.1 Experimental Considerations*

The main limitation of electrochemical systems is the limited voltage that can be

applied. Due to the occurrence of electrolyte break down, the maximum applied voltages tend to be limited to ±3 V.[259] To adequately model the field dependence, the electrical field driving charge transport must be varied over several orders of magnitude. Thus, to obtain the necessary high fields without exceeding the stability of the electrolyte, the channel length of the conjugated polymer must be very small.

Using the relatively simple shadow mask or liftoff processes, channel lengths of 10 μm are possible. This would limit electric fields to ~3 kV/cm, which is insufficiently high to have the range of fields necessary to draw a strong conclusion. Further, while an ionic liquid electrolyte may be stable under the application of 3 V across the channel necessary to obtain high fields, this would result in drastic variation in the degree of oxidation (doping) of the polymer across the channel. In order to minimize this effect, the electrolyte may be cooled while under gate bias, freezing in a constant doping and charge density profile in the conjugated polymer. This has already been demonstrated in solid polymer electrolyte gated systems in order to collect wide temperature window conductivity data.[260]

Additionally, since the kinetics of the electrolyte breakdown reactions are exponentially dependent on temperature, decrease the temperature would slow breakdown reaction rates and broaden the electrochemical window. This has been clearly demonstrated in ionic liquid gated molecular crystals, where cooling the ionic liquid to just above the freezing/glass transition temperature yields an increase in the electrochemical stability window by over a factor of two.[261] Presumably, since the breakdown reactions require mass transport, below the freezing/glass transition

temperature the electrolyte would be limited by the dielectric breakdown of the frozen ionic liquid, which is expected to occur only at voltages much higher than the limit of the electrochemical window. Thus, in a frozen electrochemical system, it is reasonable to expect an accessible range of fields exceeding 10 kV/cm.

### *8.1.2 Theoretical Considerations*

Due to the necessity of shrinking the channel dimension to obtain higher fields, it is necessary to account for resistance occurring at the interface of the conjugated polymer and the source/drain electrodes, commonly referred to as contact effects.[262,263] Fortunately, Braga *et al* have thoroughly characterized the contact effects in (gelled) ionic liquid gated P3HT devices.[264] Differing drastically from traditional FET devices, the contact resistance of ionic liquid gated conjugated polymers is very low, especially at high charge carrier density. This is thought to occur since the ionic liquid ions are mobile within the conjugated polymers, they naturally distribute themselves such to minimize electric field inhomogeneities, including those at the electrode interfaces which give rise to a potential barrier to charge injection. With proper choice of gate bias, and thus charge density, the ionic liquid gated conjugated polymer system may be frozen in a state of low contact resistance.

As noted above, at temperatures above the electrolyte freezing/glass transition temperature, the ions, and thus the doping profile, are free to move within in the conjugated polymer channel. Due to this fact, many conductivity studies have opted to apply a low source-drain bias, <100mV, such that the doping profile is generally constant. In a frozen electrolyte, the ions can no longer redistribute themselves in response to a source-drain bias, thus a direct comparison at high fields between frozen

systems, and previous results collected about room temperature is ill advised. Additionally, in regions of very high bias, care must be taken to not misinterpret hopping and field emission for more exotic transport processes.[265,266,267,268,269]

### *8.1.3 Initial Charge Transport Analyses*

Successfully measuring charge transport under a variable electric field would allow for the more rigorous assessment of charge transport models, and the clarification of charge transport processes. For instance, consider the Poole-Frenkel[270] model of charge transport:

$$J = q\mu F n_d \exp\left(\frac{-E_A + \beta F^{1/2}}{k_B T}\right)$$

Where $q$ is the electron charge, $\mu$ is the carrier mobility, $F$ is the electric field, $n_d$ is the dopant density, $E_A$ is the activation energy, $k_B$ is Boltzmann's constant, and $T$ is the absolute temperature. The parameter $\beta$ is given as:

$$\beta = \left(\frac{q^3}{\pi\varepsilon_0\varepsilon}\right)^{1/2}$$

Where ε is the dielectric constant and $\varepsilon_0$ is the permittivity of free space. Using Poole-Frenkel, the density of charge carriers that are free to contribute to charge transport, $n_f$, is given as:

$$n_f = n_d \exp\left(\frac{-E_A + \beta F^{1/2}}{k_B T}\right)$$

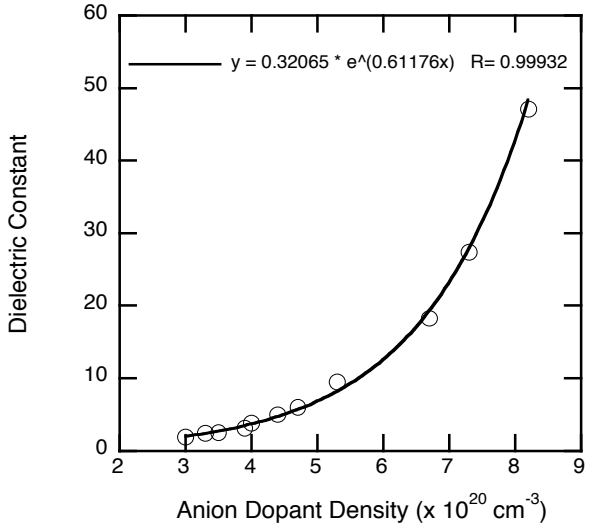


**Figure 8.1** Ionic liquid doped P3HT dielectric constant with an empirical fit, adapted from [271].

The experimental charge transport data of the P3HT gated with the ionic liquid [EMI][FAP], presented in Chapter 6, may be rudimentarily interpreted with this model. First, $\beta$ was determined using the charge density dependent dielectric constant of ionic liquid gated P3HT measured by Wang *et al*.[271] For simplicity the experimental dielectric constant data were empirically fit, Figure 8.1. Since the conductivity of [EMI][FAP] gate P3HT was measured at a low field condition, the magnitude of $\beta F^{1/2}$ was small, and remained below 1% of the measured activation energy.

Thus according to Poole-Frenkel model, the "real" carrier density contributing to charge transport was much smaller than the induced ionic liquid anion dopant density, Figure 8.2. This results in the average carrier mobility calculated using Ohm's law significantly underestimating the "real" mobility of the carriers free to contribute to conduction, Figure 8.3. The fraction of dopants that actually produce a mobile charge carrier is not a quantity commonly reported, but is valuable for it's tangible significance.

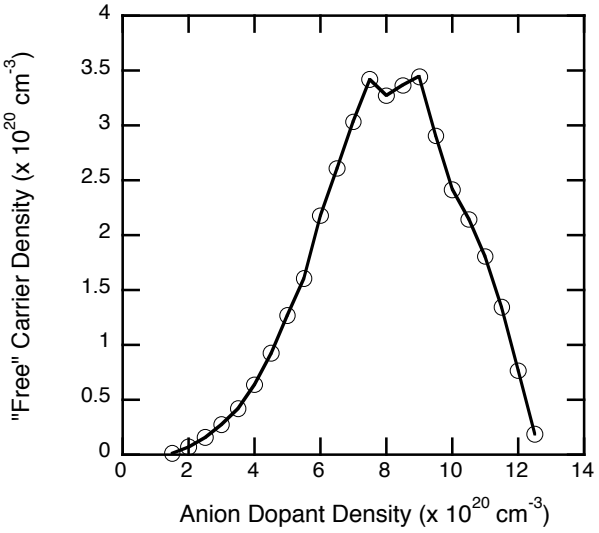


**Figure 8.2** Calculated "free" carrier density and anion dopant density in ionic liquid doped P3HT.

While decoupling the excitation of free carriers from the motion of carriers, for key reasons the Poole-Frenkel model is falls short of fully describing charge transport in doped disordered conjugated polymer systems. Namely, there is an assumption of temperature independent mobility, which is not supported by the experimental literature.[272] In essence, a Poole-Frenkel analyses of transport in the P3HT/[EMI][FAP] presented in Chapter 6 is simply a reinterpretation of the Arhennius behavior. The mobility prefactor becomes the "real" mobility, and product of the charge density and the exponential temperature term become the "free" carrier density, but overall the temperature-conductivity relationship is unchanged.

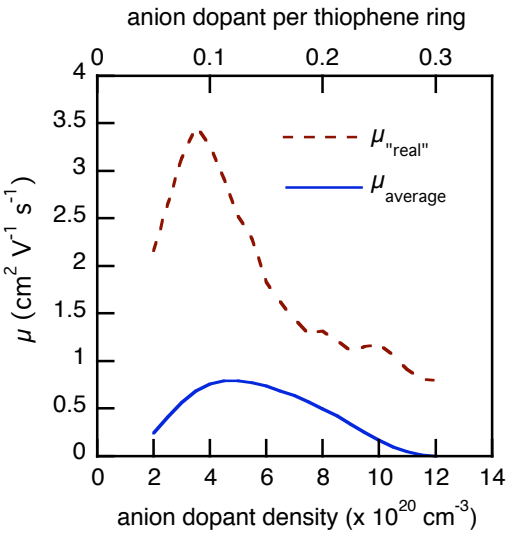


**Figure 8.3** Calculated "real" and average carrier mobility versus anion dopant density in ionic liquid doped P3HT.

Intuitively, a field dependent lowering of the activation energy of conduction is expected. Additionally, the excitation of carriers out of Coulombic traps (dopants), and their subsequent motion are both reasonably expected to be thermally activated, with a field dependent lowering of the activation energy. Gregg *et al* have in fact proposed a expanded Poole-Frenkel model to account for just such behavior.[273]

$$J = q\mu_f n_f F$$

$$J = q\mu_o n_d \exp\left(\frac{-(E_{A,\mu} + E_{A,n}) + \beta F^{1/2}}{k_B T}\right) F$$

The free carrier density and mobility, $n_f$ and $\mu_f$ respectively, should both demonstrate Arhennius behavior, with the experimentally extracted activation energy being a summation of the activation energies of the individual charge generation and hopping processes. Thus, the free carrier density and mobility should both increase with increasing temperature or electric field. By mapping the temperature, dopant density, and

electric field parameter space of conductivity, and deconvoluting the charge generation from the charge hopping, the density and mobility of "free" or untrapped charge carriers can be assessed. In a system such as P3HT/[EMI][FAP], where absolute energy levels can be determined, this represents the local density of states near the Fermi level which actually contribute to charge transport, and the ease of hopping between those states.[274]

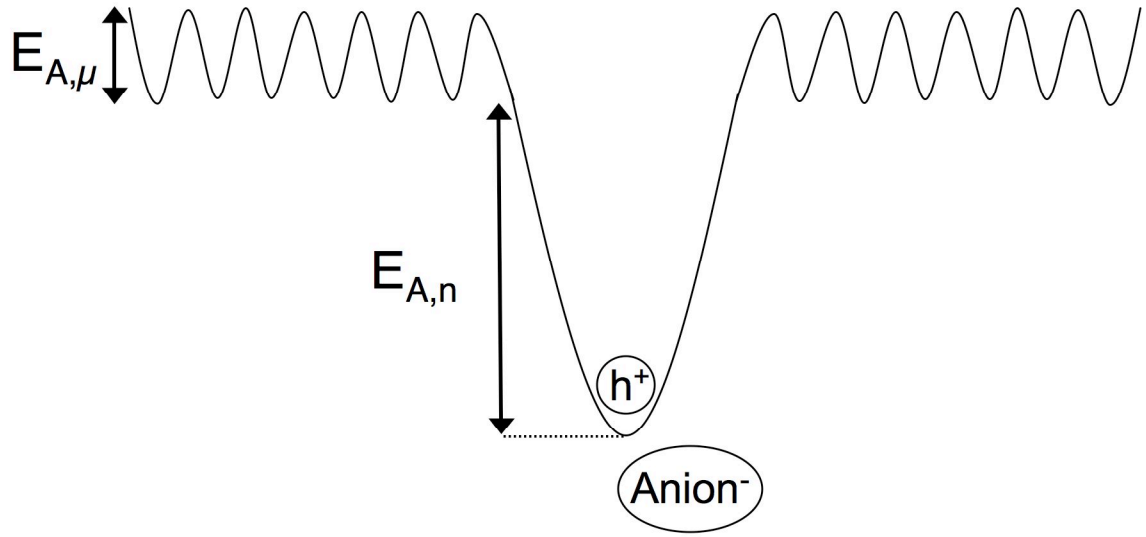


**Figure 8.4** Schematic of energy disorder representing the activation energy to generate a free carrier ($E_{A,n}$) and the successive energy of charge carrier motion ($E_{A,\mu}$) in a n electrochemically doped disordered system.

However, at this point, such analysis is conjecture without a thorough investigation of field dependence. The field dependence of charge transport in ionic liquid gated conjugated polymers is an accessible measurement, which if carried out, provides another route to investigate the complex nature of charge transport at very high carrier densities.

## *8.2 Vinyl Incorporating Donor-Acceptor Copolymer Solar Cells*

As discussed in chapter 7, acyclic diene metathasis polymerization is a unique synthetic route to high molecular weight vinyl incorporating conjugated polymer.[275] Especially intriguing is the ability to readily produce statistical donor-acceptor type copolymers with completely tunable donor-acceptor ratio, due to the shared monomer end functionality. This has been shown, in chapter 5, to enable tunability of both the energetic position of the highest occupied molecular orbital and the magnitude of the optical band gap.[276] Clearly, it is desirable to study the effects of these two tunable properties on performance in functioning bulk heterojunction polymer fullerene solar cells.

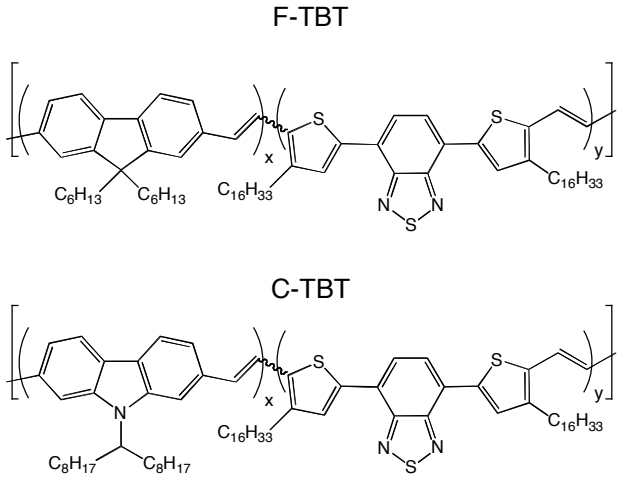


**Figure 8.5** Chemical structures of fluorene containing F-TBT and carbazole containing C-TBT statistical copolymers, both of which are statistical vinyl incorporating analogues of high performance donor-acceptor polymers for photovoltaic applications.

### *8.1.1 Fluorenyl Vinyl Donor Solar Cells*

Extended from the work in chapter 5, solar cells have been fabricated and tested incorporating copolymers synthesized from 2,7-divinyl-9,9-dihexyl-9H-fluorene (F) and 4,7-Bis(5-propenyl-4-hexadecyl-2-thienyl)-2,1,3-benzothiadiazole (TBT) in a 1:1 ratio, Figure 8.5. Solar cells with an active layer of the F-TBT copolymer and PCBM is a 1:4 ratio were tested under simulated solar illumination, AM 1.5, Figure 8.6. The solar cells showed a high open circuit voltage of 0.75 V, and reasonable short circuit current density of 4.3 mA $cm^{-2}$. However, a low fill factor of 0.36 limited the overall power conversion efficiency to 1.2%. The observed low fill factor may be the result of recombination within the device, which can be qualitatively investigated by collecting variable light intensity *J-V* curves.

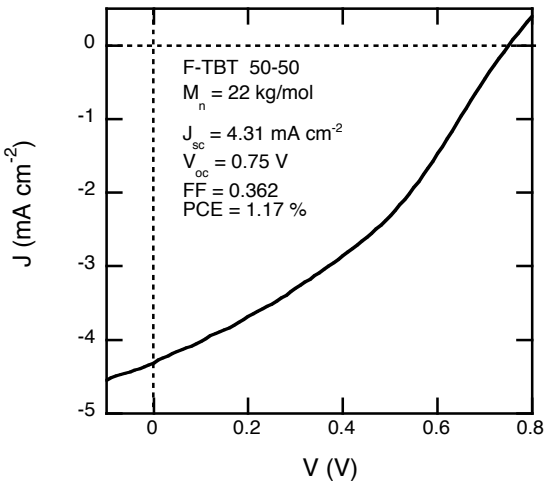


**Figure 8.6** *J-V* characteristics of 50-50 F-TBT copolymer solar cell with a 1:4 copolymer:PCBM active layer, under simulated AM 1.5 spectrum.

This performance is consistent with other flourene and benzothiadiazole incorporating perfectly alternating donor-acceptor copolymers, with non-vinyl analogues consistently reporting ~2% efficiency,[277,278,279] and vinyl analogues reporting 1.5%

efficiency (albeit with the much broader absorbing PC71BM fullerene acceptor, which improves performance).[280] As with our results, in both cases, optimized compositions were 1:4 polymer-to-fullerene, and fill factors were low, thus demonstrating that vinyl incorporating random statistical copolymers perform roughly as well as there alternating and non-vinyl equivalents. This is especially encouraging, as previous vinyl analogues performed underperformed by a factor of four compared to their non-vinyl equivalents.[281,282,283,275]

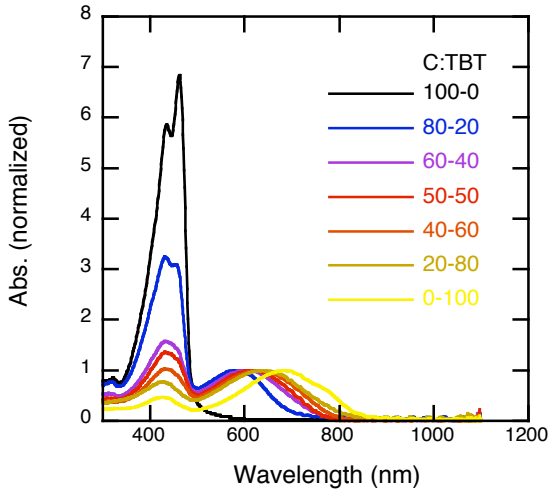


**Figure 8.7** UV-Vis spectra of the C-TBT series copolymer thin films.

Yet to be carried out is the investigation of fluorene and benzothiadiazole rich copolymers in photovoltaic devices. As discussed in Chapter 5, the open circuit voltage is expected to vary directly with HOMO level position, and considering the non-monotonic variation of hole mobility with copolymer composition, increased device performance is expected at copolymer compositions other than 50:50. Additionally, variable light intensity measurements should be carried out to assess the role of recombination in these devices, and study the effect of copolymer composition on

recombination.

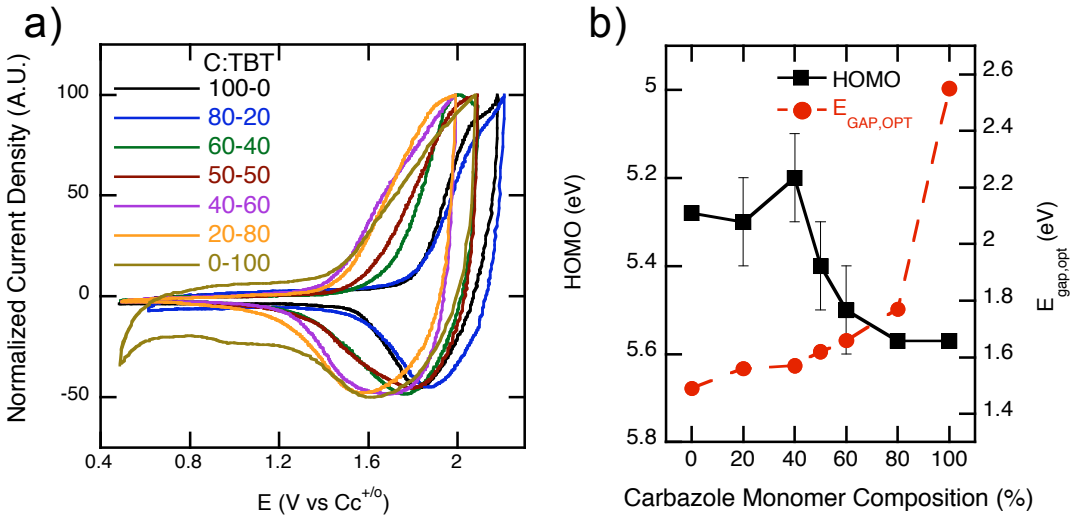


**Figure 8.8** (a) Cyclic voltammograms of the C-TBT series copolymer thin films collected in [P14][TFSA] ionic liquid electrolyte at 50 mV/s. (b) HOMO level position and optical band gap of the C-TBT series copolymer thin films.

### *8.2.2 Carbazole Vinyl Donor Optical and Electrochemical Characterization*

Since the above vinyl incorporating random copolymer approaches the performance of non-vinyl alternating analogues, a natural next step is to investigate a vinyl incorporating random donor-acceptor copolymer series whose non-vinyl alternating analogue readily produces high performance photovoltaic devices. Therefore carbazole and benzothiadiazole based copolymers, Figure 8.5, have been synthesized by Josh Speros, as they have been reported to in solar cells with efficiencies exceeding 5%.[284]

Initial optical and electrochemical characterization, Figures 8.7 and 8.8a, reveal band gap and HOMO level behavior very similar to the fluorene based series in Chapter 5. Copolymers display broad absorption from ~350 to ~ 750 nm. The band gap displays a hockey stick behavior with initial incorporation of benzothiadiazole resulting in a

drastic decrease in band gap, followed by shallow linear decrease in band gap with increasing benzothiadiazole composition, Figure 8.8b. The cyclic voltammograms revealed a general deepening of the HOMO level position with increasing carbazole content. However, in several of the copolymers in the series, the reduction of the copolymer and the reduction of the calibrant overlapped, limiting the accuracy of the HOMO level determination, and precluding in depth discussion beyond the general HOMO level trend. This may potentially be rectifiable by using ferrocene as an internal calibrant, however, the ferrocene oxidation/reduction process will very likely overlap with the copolymer oxidation. Still, the initial data demostrate that the band gap can be varied over 1 eV, from 1.49 to 2.55 eV, and the HOMO level position can be varied 0.3 eV, from 5.28 to 5.57 eV, by varying copolymer composition, Table 8.1.

**Table 8.1** UV–vis and cyclic voltammetry data for homo- and copolymers

| sample ID[a] | $\lambda^1_{max,film}$ (nm)[a] | $\lambda^2_{max,film}$ (nm) | $E_g^{opt}$ (eV)[b] | $E_{ox,onset}$ (V vs $Cc^{o/+}$)[c] | HOMO (eV) |
|---|---|---|---|---|---|
| PCV | 436(463) | – | 2.55 | 1.82 | 5.57 |
| TBTV | 430 | 682 | 1.49 | 1.53 | 5.28 |
| C-TBT | | | | | |
| **1a** (80:20) | 435(457) | 577 | 1.77 | 1.5* | 5.3* |
| **1b** (60:40) | 431 | 601 | 1.66 | 1.4* | 5.2* |
| **1c** (50:50) | 431 | 617 | 1.62 | 1.6* | 5.4* |
| **1d** (40:60) | 431 | 629 | 1.57 | 1.7* | 5.5* |
| **1e** (20:80) | 430 | 630 | 1.56 | 1.82 | 5.57 |

[a]Polymer film spin coated from $CHCl_3$ onto glass substrates; values in parentheses are secondary peaks/shoulders. [b]Determined from onset absorption of thin film ($E_g^{opt}$ = 1240 (nm eV)/ $\lambda_{onset}$ (nm)). [c]Determined by cyclic voltammetry. [d]Determined by conversion from calibrated cobaltocenium potential ($E_{red,Cc}$ = 3.75 eV). *Cobaltocenium reduction convoluted with polymer reduction, referenced oxidation onsets and HOMO levels estimated within ±100 mV and meV respectively.

The fabrication, testing, and optimization of transistor and photovoltaic devices remain to be carried out. These experiments are promising as carbazole and benzothiadiazole donor-acceptor polymers have been demonstrated as exceptional candidates for light harvesting applications.[284] Additionally, this will expand the understanding of the random donor-acceptor copolymer structure-properties-performance relationship in photovoltaic applications, which until now has not been studied.

## *8.3 Vinyl Dilution and Alkyl Chain Position in Thienyl Vinyl Polymers: Charge Transport and Photovoltaic Properties*

Excluding poly(phenylene vinylene) derivatives, in photovoltaic applications, it has been generally observed that vinyl incorporating conjugated polymers perform more poorly than their non vinyl incorporating equivalents.[275,280,283] This has been attributed to weaker light absorption[275] and decreased exciton lifetime[285] in vinyl incorporating polymers. However, there has yet to be a systematic variation of the vinyl composition of a conjugated polymer and investigation of the resulting optoelectronic properties. An ideal series is one based on poly(3-akyl thiophene), considering that regioregular poly(3-hexyl thiophene), P3HT, is a benchmark polymer in both conjugated polymer based solar cell and transistor devices. Thus we propose the study of P3HT in conjunction with alkyl substituted poly(thienylene vinylene), poly(bithienylene vinylene)s, and poly(terthienylene vinylene).

### *8.3.1 Vinyl Dilution*

Poly(3-alkyl thienylene vinylene) is a non degenerate ground state (benzoidal and quinodal states) conjugated polymer that is unique in lacking photoluminescent properties. It has been proposed that photo-generated excitons rapidly decay into long

lived trapped dark states, which likely cannot dissociate and contribute to photocurrent.[285] Additionally, these dark states have been shown to dramatically alter the absorptive properties of the polymer when occupied, which is likely the cause of the overall low strength of absorption. Still, poly(thienylene vinylene) displays a relatively narrow band gap (~1.65 eV compared to 1.9 eV for P3HT), and high hole mobility.[275,286] Thus it is desirable to maintain a narrow band gap while modifying the polymer structure to overcome the unique optical properties of poly(thienylene vinylene).

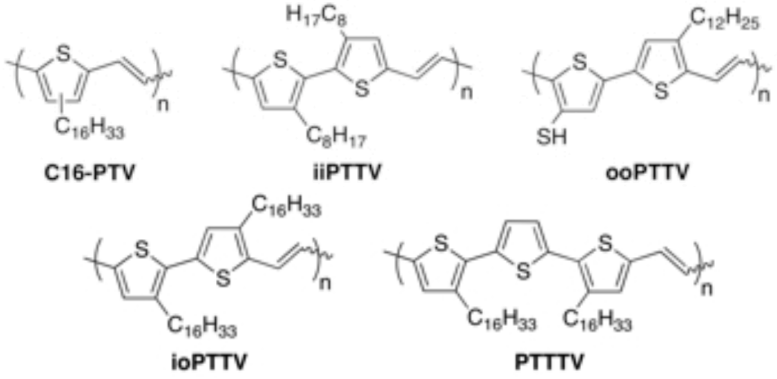


**Figure 8.9** Chemical structures of the thienyl vinyl, bithienyl vinyl, terthienyl vinyl polymers to be investigated.

To accomplish this Josh Speros has prepared a series of alky substituted poly(thienylene vinylene)s from monomers with thiophene to vinyl ratios varied from 1:1 to 3:1, Firgure 8.9. The 1:1, C16-PTV in Figure 8.9, polymer has been extensively investigated previously (Chapter 7). Initial characterization of the 3:1 polymer, PTTTV in Figure 8.9, reveals optical and electrochemical properties very similar to those of P3HT. As measured by thin film UV-Vis absorption, the band gap of PTTV (1.78 eV) is slightly narrowed by the incorporated vinyl, with a peak in absorption occurring at 563 nm with a shoulder around 600 nm, Figure 8.10a. Cyclic voltammograms of PTTTV thin

films display, Figure 8.10b, an oxidation onset of 1.4 V vs $Cc^{+/o}$, which translates to a HOMO depth of 5.15 eV, roughly 0.1 eV deeper than P3HT.[276]

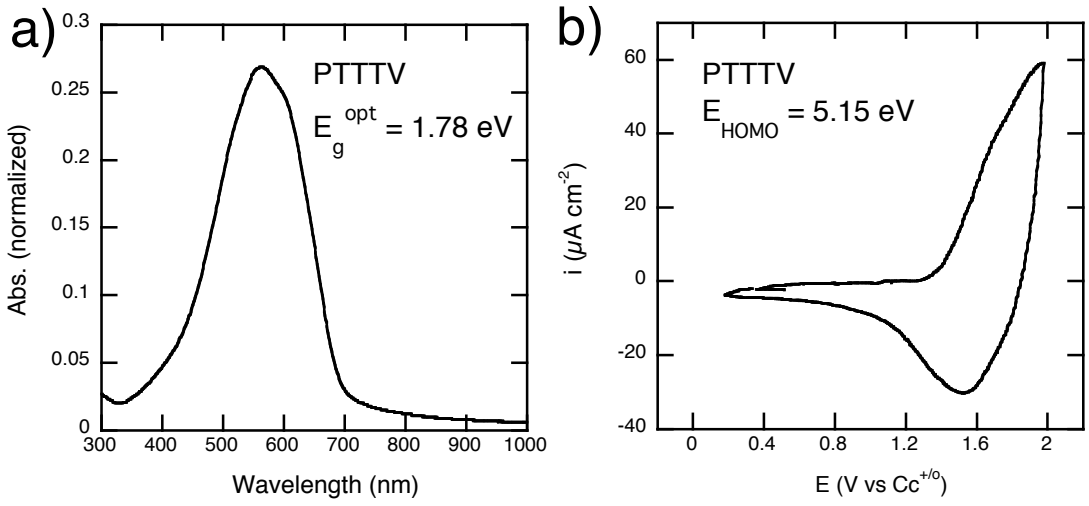


**Figure 8.10** PTTTV thin film (a) UV-Vis absorbance spectra, and (b) cyclic voltammogram in the ionic liquid electrolyte [P14][TFSA] collected at 50 mV $s^{-1}$.

Yet to be carried out is the fabrication and characterization of transistors and bulk heterojunction solar cells with PTTTV as the donating polymer. The same optical, electrochemical, charge transport, and photovoltaic studies shall be carried out with the other PTTV polymers, in order to quantify the effect of vinyl incorporation on photovoltaic properties.

### *8.3.2 Alkyl Chain Position*

In addition to elucidating the effects of vinyl dilution, this series allows the study of alkyl chain position beyond just regiorandomness and regioregularity. Regio regular and regiorandom poly(alkyl thienylene vinylene) displays much more similar optical and electronic properties compared the to the drastically different properties of regio egular

and regiorandom P3HT.[287,288] In fact poly(dodecylthienylenevinylene) shows similar band gap, HOMO level position, crystallinity, and photovoltaic device performance regardless of the degree of regioregularity. This may be due to the separation of thiophene units by vinyl units, resulting in in creased alkyl chain separation and less alkyl chain interaction in the head-to-head configuration present in regiorandom polymers.

In the case of poly(bithienylene vinylene), each thiophene has a vinyl and a thiophene neighbor, thus two similar length alkyl chains can exist in a outside-outside (ooPTTV), inside-inside (iiPTTV), or inside-outside structure (ioPTTV), Figure 8.9. Intuitively, the inside-inside coniguration should produce a twisted polymer back bone due to steric hindrance of the two closely spaced alkyl chains. This should produce an amorphous polymer, with a wider band gap and poorer charge transport properties, analogous to the case of regiorandom P3HT. Conversely, the outside-outside and inside-outside configurations should result in more planarized polymers that should exhibit more ordered packing (crystallinity), narrower band gap, and better charge transport characteristics. While regioregularity and alkyl chain length have been areas of extensive study,[289,290] these poly(bithienylene vinylene)s provide a unique system, through which the effects of alkyl chain interactions may be studied, beyond the scope of pure regioregularity.

## *8.4 Variable Temperature Charge Transport in High Performance Polymer Fullerene Bulk Heterojunctions*

Whereas temperature dependent charge transport studies of conjugated polymers is transistor structures is commonplace, such studies of conjugated polymers in photovoltaic devices remains rare. Variable temperature measurements are key to understanding the

mechanisms of charge transport, which is of key importance in polymer fullerene bulk heterojunction solar cells.

Unfortunately, variable temperature measurements are often only carried out on single, possibly optimized, device structures, in order to compare different donor or acceptor materials. Therefore, proposed here is not a variable temperature comparison of different material systems, but instead a systematic variable temperature study of the device parameter space (active layer composition, active layer thickness, deposition solvent, cathode materials, interlayers, etc.) of one high performance material set. The goal proposed is the thorough quantification of *J-V* behavior in order to achieve and understand optimized device performance.

### *8.4.1 Illuminated Variable Temperature Measurements*

Both the illuminated and dark *J-V* characteristics, when measured across a range of temperatures, provide meaningful insight into the physics of solar cell device operation. In the case of variable temperature measurements carried out under illumination, the behavior of the short circuit current density can reveal the nature and relative rates of recombination,[291,292,293] identify the limiting steps in charge transport,[291,294] and even estimate the donor HOMO and acceptor LUMO DOS widths.[292] Likewise, variable temperature behavior of the open circuit voltage can provide insight into the nature of the recombination process.[295] Additionally it allows an estimation of the interfacial band gap, the difference between the donor HOMO and acceptor LUMO, and the degree to which the quasi Fermi levels of both the donor and acceptor have shifted into the gap.[295,296,297]

The interfacial band gap represents an upper limit of the open circuit voltage, and

thus a practical limit device performance. Generally, the open circuit voltage of a polymer-fullerene bulk heterojunction device decreases with increasing temperature. The interfacial band gap is readily extracted by plotting the variation of open circuit voltage versus temperature, and linearly extrapolating to zero temperature. This can be confirmed by repeating the measurement at several different illumination intensities. Under increased illumination intensity, the open circuit voltage decreases more slowly with increasing temperature, yet displays an illumination intensity independent zero temperature intercept. Previously, the interfacial band gap has been considered solely dependent on the material set chosen, with the magnitude representing the difference between the donor HOMO and acceptor LUMO.

Due to limited study, whether or not the interfacial band gap varies with device structure/composition has not been assessed. Presumably, previous studies have been on optimized structures. It is unknown if, within a single material set, the extracted interfacial band gap, $E_{g,int.}$, varies with device design. It is reasonable to expect the interfacial band gap to be suppressed in sub-optimized devices. In fact the convergence $E_{g,int.}$, and the difference between the donor HOMO and acceptor LUMO, $\Delta E_{DA}$, could be an external assessment of device optimization for a materials set, *i.e.* $E_{g,int.} = \Delta E_{DA}$ optimum, $E_{g,int.} < \Delta E_{DA}$ sub-optimum. Alternatively, the interfacial band gap may be a fundamental parameter, extractable from any variable temperature data set, with the slope of the variation open circuit voltage with temperature represent the degree of device optimization, in the same way illumination modifies the variation of open circuit voltage with temperature. Regardless, these relationships have yet to be investigated and could

potentially yield useful information for maximizing device performance.

### *8.4.2 Dark Variable Temperature Measurements.*

From solar cell *J-V* curves collected in the dark, variable temperature measurements become a powerful tool to probe the energetics of the interaction of the donor and acceptor materials. This is achieved by modeling the diode current, and extracting key parameters. Applying the generalized Shockley equation,[298] the *J-V* behavior of a solar cell can be described as the following:

$$J = \frac{1}{1 + R_s/R_p}\left\{J_0\left[\exp\left(\frac{q(V - JR_sA)}{nk_BT}\right) - 1\right] + \frac{V}{R_PA} - J_{ph}\right\}$$

Where $J$ is the current density passing through the devices, $V$ is applied voltage, $A$ is the device cross-sectional area, $R_s$ is the series resistance, $R_p$ is the shunt resistance, $n$ is the diode ideality factor, $k_B$ is Boltzmann's constant, $T$ is the absolute temperature, $J_0$ is the reverse saturation current, and $J_{ph}$ is the photo generated current.

In the case of $R_p >> R_s$, the equation simplifies to the following:

$$J = J_0\left[\exp\left(\frac{q(V - JR_sA)}{nk_BT}\right) - 1\right] - J_{ph}$$

Additionally, the exponential prefactor, $J_0$, itself has an exponential dependence on temperature described with the following Arrhenius relationship:

$$J_0 = J_{00}\exp\left(\frac{\phi}{nk_BT}\right)$$

Where $J_{00}$ is the interfacial electronic coupling factor for reverse bias current generation, and $\phi$ is the activation energy of the reverse saturation current and is related to the energy difference between the donor HOMO and accepter LUMO, $\Delta E_{DA}$.[299]

Using the Shockley model, $J_{oo}$ becomes an exceedingly valuable parameter for device analysis due to its ability to relate short circuit current density, $J_{SC}$, and open circuit voltage, $V_{OC}$. At the open circuit condition, where $J = 0$, by assuming the photo generated and short circuit current density to be equal, $J_{SC} = J_{ph}$, the simplified Shockley equation above can be rearranged as the following:

$$V_{OC} = \frac{nk_BT}{q}\ln\left(\frac{J_{SC}}{J_0}\right)$$

Substituting for $J_0$ yields:

$$V_{OC} = \frac{\phi}{q} + \frac{nk_BT}{q}\ln\left(\frac{J_{SC}}{J_{00}}\right)$$

Thus producing a relationship between the key device performance parameters, $J_{SC}$ and $V_{OC}$, based on the energetics ($\phi$) of the donor and acceptor, and the summation of parasitic current components (leak, recombination, etc.), which diminish device performance, represented by $J_{00}$.[299,300]

Both $J_{00}$ and $\phi$ are extractable from experimental variable temperature dark *J-V* curves by plotting the product $n\ ln(J_0)$ vs. $1/T$. Rearrangment of Arrhenius dependence of $J_0$ yields:

$$n\ln J_o = n\ln J_{00} - \left(\frac{\phi}{k_B}\right)\frac{1}{T}$$

Thus the from the plot of $n\ ln(J_0)$ vs. $1/T$, the slope contains $\phi$ and the intercept contains $J_{00}$. The choice of plotting the product $n\ ln(J_0)$, as opposed to $ln(J_0)$, is due to the fact that the ideality factor, $n$, is experimentally shown to be temperature dependent. Plainly, $J_{00}$ and $\phi$ are parameters which are desired to be minimized and maximized, respectively,

and provide a quantitative device assessment which is theoretically relatable to the concrete parameters which dictate device performance, $J_{SC}$ and $V_{OC}$.

### *8.4.3 Proposed Variable Temperature Measurements*

Both the illuminated and dark variable temperature *J-V* characteristics provide meaningful insight into the physics of solar cell device operation. Illuminated measurements provide insight into the practical limits of device performance, and can assess how well a device structure approaches these limits.[295] From dark measurements, $J_{00}$ and $\phi$ have demonstrated their utility in quantifying experimentally the donor-acceptor interaction, as related to molecular orbital positions and alkyl side architecture.[299,300] Due to the insight available from variable temperature measurements, we propose the investigation of the variable temperature *J-V* behavior of both optimized and non-optimized devices structures of the high performance system poly{2,6′-4,8-di(5-ethylhexylthienyl) benzo [1,2-b;3,4-b]dithiophene-alt-5-dibutyloctyl-3,6-bis(5-bromothiophen-2-yl) pyrrolo [3,4-c]pyrrole-1,4-dione} (PBPTT-DPP) and [6,6]-phenyl C71 butyric acid methyl ester ($PC_{71}BM$), illuminated and in the dark. Recently, PBPTT-DPP: $PC_{71}BM$ 1:2 solar cells spun from chlorobenzene solvent containing 3 vol% 1-8-diiodooctane (DIO) have been reported with power conversion efficiencies exceeding 6%. The cells displayed high short circuit current densities, 13.5 mA $cm^{-2}$, open circuit voltages, 0.74 V, and fill factors, 0.65, in both traditional and inverted structures.[301] Thus the PBPTT-DPP/$PC_{71}BM$ system provides a high performance test bed to quantify the effects of device composition (polymer:fullerene ratio, additive content) and device structure (active layer thickness), through illuminated and dark variable temperature

current voltage measurements.

## *8.5 Polymer Solar Cell Optimization via "Design of Experiments"*

There currently exists a dearth of studies that provide a systematic experimental picture of a material system in polymer-fullerene photovoltaics. Often, reports will only include the performance of a reportedly optimized device, and most intensive characterization is only carried out on optimized devices and structures. This severely hampers the advancement within the field of polymer fullerene bulk heterojunctions, as there are numerous parameters defining any given solar cell device. Here we propose the application of a well-established method of experimental design and data analysis, to improve device optimization and create comprehensive data sets.

### *8.5.1 Complexity in Polymer-Fullerene Bulk Heterojunction Solar Cells*

Generally speaking, the common variables of device fabrication fall under device architecture, anode and cathode choice, active layer materials and composition, active layer processing choices, interlayer choice, additive choice, and post processing. Device architecture covers the thickness of the various device layers, and whether the structure is in a standard configuration, with light entering through a transparent anode, or an inverted configuration, with light entering through a transparent cathode. The development of high efficiency inverted structures has greatly increased the choice of anode and cathode materials.[302] While many studies focus on a single donor material, the relative composition of the donor and acceptor has become, and the development of indene and $C_{71}$ adducts has greatly complicated the choice and composition of active layer materials.[303] The solvent and concentration of the solution from which the active

layer is spin coated, the rate at which the spin coating is carried out, and the rate at which the film is allowed to dry all have significant effect on the thickness and morphology of the active layer. Numerous additives and interlayers have been developed to further improve device performance.[304,305] Finally there exists all manner of thermal and solvent annealing steps to promote preferential morphology in the active layer.

There exist no end to the possible combination parameters that can be tuned when fabricating bulk heterojunction photovoltaic devices. Even for relatively simple device structures, the experimentalist must work in 5+ dimensional space. Clearly, the term "optimized device" is relative. There do exist robust studies that systematically vary device variables, however these reported experiments often only produced single slices of the given systems parameter space, left large regions untouched, and thus potentially failed to establish a true optimized device.

### *8.5.2 Polymer Solar Cell DOE Methodology Overview*

In current polymer solar cell research, the classic technique of varying one parameter, while all else are held constant is prohibitively cumbersome. It is necessary to look to numerical methods to assist in the designing of experiments carried out such that the parameter space is thoroughly and efficiently mapped. Appropriately, these numerical methods are referred to as Design of Experiments (DOE) methodology,[306] and there exist several commercial DOE software packages. Surprisingly, a literature search produces only one scholarly article,[307] and one master's thesis on applying DOE to polymer solar cells.[308]

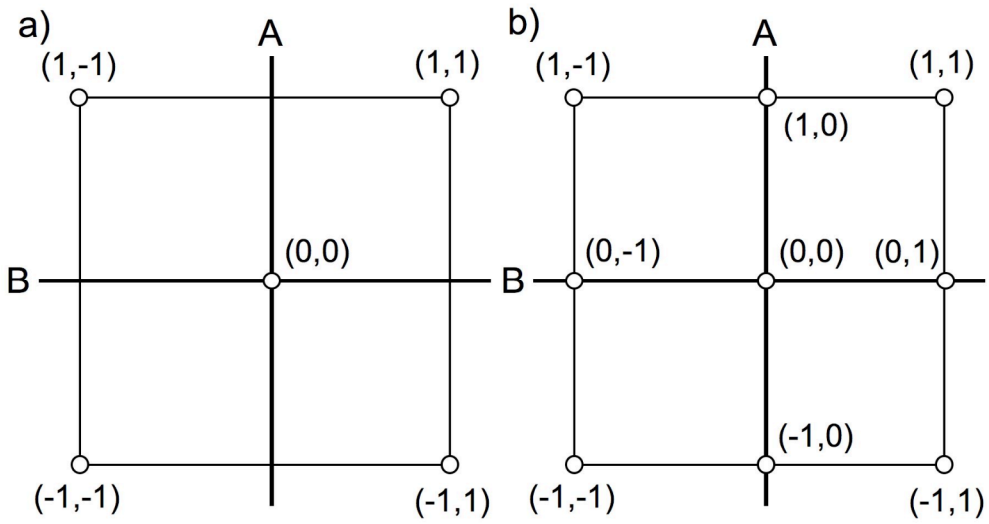


**Figure 8.11** Examples of a two parameter space mapped with (a) $2^2$ design and (b) $2^3$ design, both with centerpoint.

In the simplest of terms a DOE methodology produces an array of proposed experiments to cover the parameter space being investigated (*e.g.* spin speed, solution concentration, solution composition, anode/cathode choice, interlayer choice, additive concentration, etc.). Often this follows the form of $2^2$ or $2^3$ factorial design, which are displayed in two dimensions in Figure 8.11. The location of the proposed experiments in parameter space can be modified to take advantage of previous experimentally observed relationships. The experiments are carried out, and a response variable is measured (*e.g.* efficiency, open circuit voltage, short circuit current density, fill factor, dark current, etc.).

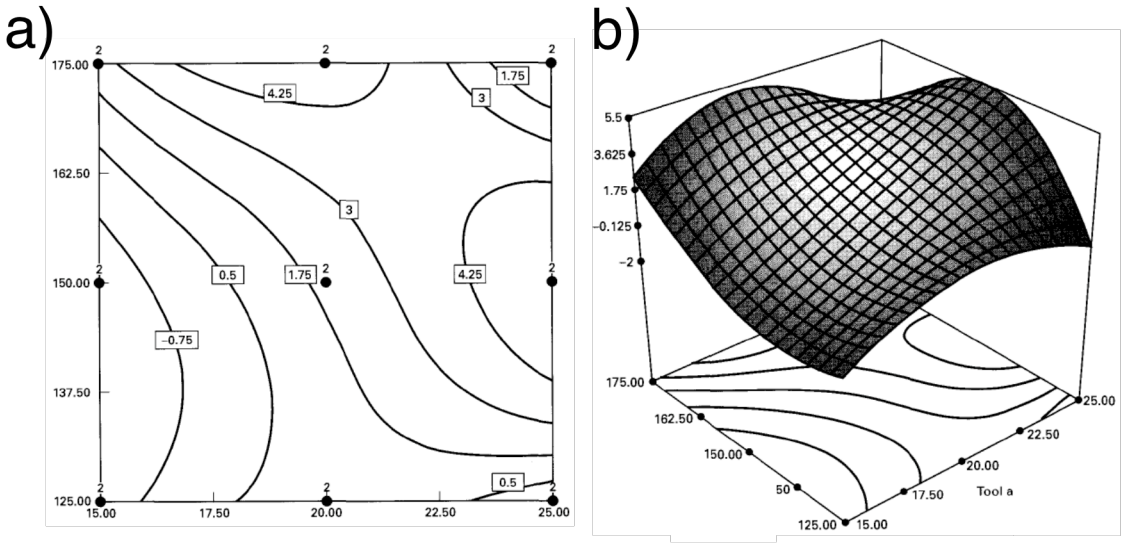


**Figure 8.12** Examples of empirically fit response surface as a (a) two dimension and (b) three dimensional contour plot adapted from [306].

The response variables are statistically analyzed to ascertain whether or not their variation with the varied parameters is significant. Here specifically, since polymer solar cells are fabricated on substrates generally with 6 or more cells per substrate, the inherent experimental reproduction increases the statistical significance of any parameter combination. The response variable is then mapped versus the experimental parameters, response surface, Figure 8.12. This surface is empirically fit to interpolate between data points. Predicted maxima in the response variable direct collection of additional experimental data points. These additional experiments are used to confirm the predicted response variable optima. This provides a statistically supported optimization of the experimental parameters.

### *8.5.3 Comprehensive Data Sets*

By employing the DOE methodology, the experimentalist has compiled a complete view of the parameter space that can be used to evaluate or develop theoretical models of polymer solar cell operation, which currently are less than adequate. Since the response surfaces have been empirically fitted, a theoretician is not bound by a single two-dimensional slice of experimental data, but can slice the investigated parameter space in any manner necessary. Especially if coupled with additional characterization (AFM, DSC, variable temperature *J-V*, etc), this DOE methodology would produce a level of comprehensive data not currently available in the polymer fullerene bulk heterojunction solar cell literature.

In short, following a DOE methodology will increase the efficiency of polymer-fullerene bulk heterojunction photovoltaic device parameter optimization, provide a quantitative assessment of the confidence in the optimized device parameters, and result in a comprehensive multidimensional data set for theoretical consideration. We propose to apply this methodology to the optimization of devices employed to study the effects of statistical copolymer composition and vinyl dilution, proposed in Sections 8.2 and 8.3 respectively. Additionally, we propose to apply this methodology to the thoroughly map the parameter space of high performance PBPTT-DPP/$PC_{71}BM$ incorporating devices investigated with variable temperature dark and illuminated *J-V* measurements, described in Section 8.4, in order to provide a comprehensive view of the charge transport energetics and their relation to solar cell performance.

## *Bibliography*

(1) Skotheim, T. A.; Reynolds, J. R. Eds. *Conjugated polymers: processing and applications.* CRC Press: New York, 2006.

(2) Hagen, K. Ed. *Organic Electronics: Materials, Manufacturing, and Applications.* Wiley-VCH: Weinheim, 2006.

(3) Cho, J. H.; Lee, J.; Xia, Y.; Kim, B.; He, Y.; Renn, M. J.; Lodge, T. P.; Frisbie, C. D. *Nature Mater.* **2008**, *7*, 900-906.

(4) Xia, Y.; Zhang, W.; Ha, M.; Cho, J. H.; Renn, M. J.; Kim, C. H.; Frisbie, C. D. *Adv. Funct. Mater.* **2010**, *20*, 587-594.

(5) Zhang, W.; Ha, M.; Braga, D.; Renn, M. J.; Frisbie, C. D.; Kim, C. H. *A 1V printed organic DRAM cell based on ion-gel gated transistors with a sub-10nW-per-cell Refresh Power.* Solid-State Circuits Conference Digest of Technical Papers (ISSCC), Feb. 20-24 2011.

(6) Braga, D.; Erickson, N. C.; Renn, M. J.; Holmes, R. J.; Frisbie, C. D. *Adv. Funct. Mater.* **2012**, *22*, 1623-1631.

(7) NREL Best Research Cell Effeciencies. http://www.nrel.gov/ncpv/images/efficiency_chart.jpg (accessed November 24, 2012).

(8) Dou, L.; You, J.; Yang, J.; Chen, C. C.; He, Y.; Murase, S.; Moriarty, T; Emery, K.; Li, G.; Yang, Y. *Nature Photon.* **2012**, *6*, 180-185.

(9) Kromhout, W. W. UCLA engineers create tandem polymer solar cells that set record for energy-conversion. http://newsroom.ucla.edu/portal/ucla/ucla-engineers-create-tandem-polymer-228468.aspx (accessed November 24, 2012).

(10) Giebink, N. C.; Wiederrecht, G. P.; Wasielewski, M. R.; Forrest, S. R. *Phys. Rev. B* **2012**, *82*, 155305.

(11) Servaites, J. D.; Ratner, M. A.; & Marks, T. J. *Energy Environ. Sci.* **2011**, *4*, 4410-4422.

(12) Bolto, B. A.; McNeill, R.; Weiss, D. E. *Aust. J. Chem.* **1963**, *16*, 1090-1103.

(13) Shirakawa, H.; Louis, E. J.; MacDiarmid, A. G.; Chiang, C. K.; Heeger, A. J. *J. Chem. Soc., Chem. Commun.* **1977**, *16*, 578-580.

(14) Chang, J.-F.; Clark, J.; Zhao, N.; Sirringhaus, H.; Breiby, D. W.; Andreasen, J. W.; Nielsen, M. M.; Giles, M.; Heeney, M.; McCulloch, I. *Phys. Rev. B* **2006**, *74*, 115318.

(15) Clark, J.; Silva, C.; Friend, R. H.; Spano, F. C. *Phys. Rev. Lett.* **2007**, *98*, 206406.

(16) Atkins, P.; de Paula, J. *Physical Chemistry*, 7th ed.; Oxford University Press: New York, 2002.

(17) Kittel, C. *Introduction to Solid State Physics*, 8th ed.; John Wiley & Sons: Hoboken, NJ, 2005.

(18) *Conducting Organic Materials and Devices*; Jain, S. C., Willander, M., Kumar, V., Eds.; Semiconductors and Semimetals 81; Academic Press: Burlington, MA, 2007.

(19) Fincher, C. R.; Ozaki, M.; Tanaka, M.; Peebles, D.; Lauchlan, L.; Heeger, A. J.; MacDiarmid, A. G. *Phys. Rev. B* **1979**, *20*, 1589.

(20) Jain, S. C. ; Geens, W.; Mehra, A.; Kumar, V.; Aernouts, T.; Poortmans, J.; Mertens, R.; Willander, M. *J. Appl. Phys.* **2001**, *89*, 3804.

(21) Dicker, G.; de Haas, M. P.; Warman, J. M.; de Leeuw, D. M.; Siebbeles, L. D. A *J. Phys. Chem. B* **2004**, *108*, 17818-17824.

(22) Mozer, A. J.; Sariciftci, N. S.; Pivrikas, A.; Österbacka, R.; Juška, G.; Brassat, L.; Bässler, H. *Phys. Rev. B* **2005**, *71*, 035214.

(23) Wang, D.; Kopidakis, N.; Reese, M. O.; Gregg, B. A. *Chem. Mater.* **2008**, *20*, 6307-6309.

(24) Saeki, A.; Koizumi, Y.; Aida, T.; Seki, S. *Acc. Chem. Res.* **2012**, *45*, 1193-1202.

(25) Sze, S. M., Ng, K. K. *Physics of Semiconductor Devices*, 3rd ed.; John Wiley & Sons: Hoboken, NJ, 2007.

(26) Bredas, J. L.; Street, G. B. *Acc. Chem. Res.* **1985**, *18*, 309-315.

(27) White, H. S.; Kittlesen, G. P.; Wrighton, M. S. *J. Am. Chem. Soc.* **1984**, *106*, 5375-5377.

(28) Alvarado, S. F.; Seidler, P. F.; Lidzey, D. G.; Bradley, D. D. C. *Phys. Rev. Lett.* **1998**, *81*, 1082-1085.

(29) Brédas, J. L.; Cornil, J.; Heeger, A. J. *Adv. Mater.* **2004**, *8*, 447-452.

(30) Kippelen, B.; Brédas, J. L. *Energy & Environ. Sci.* **2009**, *2*, 251-261.

(31) Kersting, R.; Lemmer, U.; Mahrt, R. F.; Leo, K.; Kurz, H.; Bässler, H.; Göbel, E. O. *Phys. Rev. Lett.* **1993**, *70*, 3820-3823.

(32) Dhoot, A. S.; Ginger, D. S.; Beljonne, D.; Shuai, Z.; Greenham, N. C *Chem. Phys. Lett.* **2002**, *360*, 195-201.

(33) NREL Bird Simple Spectral Model. http://rredc.nrel.gov/solar/models/spectral/SPCTRAL2/SPCTRAL2.xls (accessed November 25, 2012).

(34) Kim, Y.; Cook, S.; Choulis, S. A.; Nelson, J.; Durrant, J. R.; Bradley, D. D. C. *Chem. Mater.* **2004**, *16*, 4812–4818.

(35) Kim, Y.; Cook, S.; Tuladhar, S. M.; Choulis, S. A.; Nelson, J.; Durrant, J. R.; Bradley, D. D. C.; Giles, M. McCulloch, I.; Ha, C.-S.; Ree, M. *Nat. Mater.* **2006**, *5*, 197–203.

(36) Shaw, P. E.; Ruseckas, A.; Samuel, I. D. *Advanced Materials* **2008**, *20*, 3516-3520.

(37) Tessler, N.; Preezant, Y.; Rappaport, N.; Roichman, Y. *Adv. Mater.* **2009**, *21*, 2741-2761.

(38) Gregg, B. A. *J. Phys. Chem. C* **2009**, *113*, 5899–5901.

(39) Shklovskii, B. I.; Efros, A. L. *Electronic Properties of Doped Semiconductors*; Wiley, 1979.

(40) Ghosh, M.; Barman, A.; De, S. K.; Chatterjee, S. *Synth. Met.* **1998**, *97*, 23-29.

(41) Bässler, H. *Phys. Status Solidi B* **1993**, *175*, 15-56.

(42) Friend, R. H.; Gymer, R. W.; Holmes, A. B.; Burroughes, J. H.; Marks, R. N.; Taliani, C. D. D. C.; Bradley, C. D. D.; Dos Santos, D. A.; Bredas, J. L.; Lögdlun, M. *Nature* **1999**, *397*, 121-128.

(43) Li, G.; Shrotriya, V.; Huang, J.; Yao, Y.; Moriarty, T.; Emery, K.; Yang, Y. *Nature Mater.* **2005**, *4*, 864-868.

(44) Gong, X.; Tong, M.; Xia, Y.; Cai, W.; Moon, J. S.; Cao, Y.; Yu, G.; Shieh, C. L.; Nilsson, B.; Heeger, A. J. *Science* **2009**, *325*, 1665-1667.

(45) Chen, L.; McBranch, D. W.; Wang, H. L.; Helgeson, R.; Wudl, F.; Whitten, D. G. *Proc. Nat. Acad. Sci. USA* **1999**, *96*, 12287-12292.

(46) Lu, W.; Fadeev, A. G.; Qi, B.; Smela, E.; Mattes, B. R.; Ding, J.; Spinks, G. M.; Mazurkeiwicz, J.; Zhou, D.; Wallace, G. G.; MacFarlane, D. R.; Forsyth, S. A.; Forsyth, M. *Science* **2002**, *297*, 983-987.

(47) Moller, S.; Perlov, C.; Jackson, W.; Taussig, C.; Forrest, S. R *Nature* **2003**, *426*, 166-169.

(48) Sirringhaus, H.; Kawase, T.; Friend, R. H.; Shimoda, T.; Inbasekaran, M.; Wu, W.; Woo, E. P. *Science* **2000**, *290*, 2123-2126.

(49) Carlberg, J. C.; Inganäs, O. *J. Electrochem. Soc.* **1997**, *144*, L61-L64.

(50) Tsumura, A.; Koezuka, H.; Ando, T. *Appl. Phys. Lett.* **1986**, *49*, 1210-1212.

(51) Park, J.; Park, S. Y.; Shim, S. O.; Kang, H.; Lee, H. H. *Appl. Phys. Lett.* **2004**, *85*, 3283-3285.

(52) Xia, Y.; Cho, J. H.; Lee, J.; Ruden, P. P.; Frisbie, C. D. *Adv. Mater.* **2009**, *21*, 2174-2179.

(53) Newman, C. R.; Frisbie, C. D.; da Silva Filho, D. A.; Brédas, J. L.; Ewbank, P. C.; Mann, K. R. *Chem. Mater*. **2004**, *16*, 4436-4451.

(54) Ofer, D.; Crooks, R. M.; Wrighton, M. S. *J. Am. Chem. Soc.* **1990**, *112*, 7869-7879.

(55) Ohno, H., Ed.; In *Electrochemical aspects of ionic liquids;* John Wiley & Sons: Hoboken, **2011**.

(56) Cho, J. H.; Lee, J.; Xia, Y.; Kim, B.; He, Y.; Renn, M. J.; Lodge, T. P.; Frisbie, C. D. *Nature Mater*. **2008**, *7*, 900-906.

(57) Xia, Y.; Zhang, W.; Ha, M.; Cho, J. H.; Renn, M. J.; Kim, C. H.; Frisbie, C. D. *Adv. Funct. Mater.* **2010**, *20*, 587-594.

(58) Zhang, W.; Ha, M.; Braga, D.; Renn, M. J.; Frisbie, C. D.; Kim, C. H. *A 1V printed organic DRAM cell based on ion-gel gated transistors with a sub-10nW-per-cell Refresh Power.* Solid-State Circuits Conference Digest of Technical Papers (ISSCC), Feb. 20-24 2011.

(59) Braga, D.; Erickson, N. C.; Renn, M. J.; Holmes, R. J.; Frisbie, C. D. *Adv. Funct. Mater*. **2012**, *22*, 1623-1631.

(60) Gray, F. M. *Solid Polymer Electrolytes: Fundamental and Technological Applications*; VCH: New York, 1991.

(61) Panzer, M. J.; Frisbie, C. D. *J. Am. Chem. Soc.* **2007**, *129*, 6599-6607.

(62) Herlogsson, L.; Crispin, X.; Robinson, N. D.; Sandberg, M.; Hagel, O. J.; Gustafsson, G.; Berggren, M. *Adv. Mater.* **2007**, *19*, 97-101.

(63) Kaake, L. G.; Paulsen, B. D.; Frisbie, C. D.; Zhu, X. Y. *J. Phys. Chem. Lett.* **2010**, *1*, 862-867.

(64) Lu, A.; Sun, J.; Jiang, J.; Wan, Q *Appl. Phys. Lett.* **2009**, *95*, 222905.

(65) Bernards, D. A.; Malliaras, G. G. *Adv. Funct. Mater.* **2007**, *17*, 3538-3544.

(66) Xia, Y.; Cho, J. H.; Paulsen, B.; Frisbie, C. D.; Renn, M. J. *Appl. Phys. Lett.* **2009**, *94*, 013304.

(67) Cardona, C. M.; Li, W.; Kaifer, A. E.; Stockdale, D.; Bazan, G. C. *Adv. Mater.* **2011**, *23*, 2367–2371.

(68) Sariciftci, N. S.; Braun, D.; Zhang, C.; Srdanov, V. I.; Heeger, A. J.; Stucky, G.; Wudl, F. *Appl. Phys. Lett.* **1993**, *62*, 585-587.

(69) Dou, L.; You, J.; Yang, J.; Chen, C. C.; He, Y.; Murase, S.; Moriarty, T; Emery, K.; Li, G.; Yang, Y. *Nature Photon.* **2012**, *6*, 180-185.

(70) Denis, E.; Amsterdam, E.; Blom, P. W.; Sieval, A. B.; Hummelen, J. C *J. Phys. Chem. A* **2005**, *109*, 5266-5274.

(71) Kippelen, B.; Brédas, J. L. *Energy & Environ. Sci.* **2009**, *2*, 251-261.

(72) Stevens, D. M. Examination of Stucture-Performance Correlations in Low Band Gap Polymer Solar Cells. Ph.D. Dissertation, University of Minnesota, Minneapolis, MN, 2010.

(73) Xia, Y. Fabrication and Characterization of Organic Single Crystal and Printed Polymer Transistors. Ph.D. Dissertation, University of Minnesota, Minneapolis, MN, 2009.

(74) McQuade, D. T.; Pullen, A. E.; Swager, T. M. *Chem. Rev.* **2000**, *100*, 2537–2574.

(75) Friend, R. H.; Gymer, R. W.; Holmes, A. B.; Burroughes, J. H.; Marks, R. N.; Taliani, C.; Bradley, D. D. C.; Dos Santos, D. A.; Bredas, J. L.; Logdlund, M.; Salaneck, W. R. *Nature* **1999**, *397*, 121–128.

(76) Katz, H. E.; Bao, Z. N.; Gilat, S. L. *Acc. Chem. Res.* **2001**, *34*, 359–369.

(77) Günes, S.; Neugebauer, H.; Sariciftci, N. S. *Chem. Rev.* **2007**, *107*, 1324–1338.

(78) Zhou, H.; Yang, L.; Stuart, A. C.; Price, S. C.; Liu, S.; You, W. *Angew. Chem. Int. Ed.* **2011**, *50*, 2995–2998.

(79) Chu, T.-Y.; Lu, J.; Beaupré, I, S.; Zhang, Y.; Pouliot, J. -R.; Wakim, S.; Zhou, J.; Leclerc, M.; Li, Z.; Ding, J.; Tao, Y. *J. Am. Chem. Soc.* **2011**, *133*, 4250–4253.

(80) He, Z.; Zhong, C.; Huang, X.; Wong, W.-Y.; Wu, H.; Chen, L.; Su, S.; Cao, Y. *Adv. Mater.* **2011**, *23*, 4636–4643.

(81) Service, R. F. *Science* **2011**, *332*, 293.

(82) Chen, J.; Cao, Y. *Acc. Chem. Res.* **2009**, *42*, 1709–1718.

(83) Cheng, Y. J.; Yang, S. H.; Hsu, C. S. *Chem. Rev.* **2009**, *109*, 5868–5923.

(84) Kreyenschmidt, M.; Klaerner, G.; Fuhrer, T.; Ashenhurst, J.; Karg, S.; Chen, W. D.; Lee, V. Y.; Scott, J. C.; Miller, R. D. *Macromolecules* **1998**, *31*, 1099–1103.

(85) Lee, J.-I.; Klaerner, G.; Davey, M. H.; Miller, R. D. *Synth. Met.* **1999**, *102*, 1087–1088.

(86) Chen, X.; Schulz, G. L.; Han, X.; Zhou, Z.; Holdcroft, S. *J. Phys. Chem. C* **2009**, *113*, 8505–8512.

(87) Chen, C.-H.; Hsieh, C.-H.; Dubosc, M.; Cheng, Y.-J.; Hsu, C.-S. *Macromolecules* **2010**, *43*, 697–708.

(88) Burkhart, B.; Khlyabich, P. P.; Canak, T. C.; LaJoie, T. W.; Thompson, B. C. *Macromolecules* **2011**, *44*, 1242–1246.

(89) Khlyabich, P. P.; Burkhart, B.; Ng, C. F.; Thompson, B. C. *Macromolecules* **2011**, *44*, 5079–5084.

(90) Burkhart, B.; Khlyabich, P. P.; Thompson, B. C. *Macromolecules* **2012**, *45*, 3740–3748.

(91) Burkhart, B.; Khlyabich, P. P.; Thompson, B. C. *ACS Macro. Lett.* **2012**, *1*, 660–666.

(92) Lehman Jr., S. E.; Wagener, K. B. In *Handbook of Metathesis*; Grubbs, R. H.; Ed.; Wiley- VCH Verlag GmbH & Co.; KGaA, Weinheim, 2003; Vol. 3.

(93) Baughman, T. W.; Wagener, K. B. *Adv. Polym. Sci.* **2005**, *176*, 1–42.

(94) Tao, D.; Wagener, K. B. *Macromolecules* **1994**, *27*, 1281–1283.

(95) Nomura, K.; Miyamoto, Y.; Morimoto, H.; Geerts, Y. *J. Polym. Sci. Pol. Chem.* **2005**, *43*, 6166–6167.

(96) Nomura, K.; Morimoto, H.; Imanishi, Y.; Ramhani, Z.; Geerts, Y. *J. Polym. Sci. Pol. Chem.* **2001**, *39*, 2463–2470.

(97) Yamamoto, N.; Ito, R.; Geerts, Y.; Nomura, K. *Macromolecules* **2009**, *42*, 5104–5111.

(98) Qin, Y.; Hillmyer, M. A. *Macromolecules* **2009**, *42*, 6429–6432.

(99) Speros, J. C.; Paulsen, B. D.; White, S. P.; Wu, Y.; Jackson, E. A.; Slowinski, B. S.; Frisbie, C. D.; Hillmyer, M. A. *Macromolecules* **2012**, *45*, 2190–2199.

(100) Wagener, K. B.; Brzezinska, K.; Anderson, J. D.; Dilocker, S. *J. Polym. Sci. Pol. Chem.* **1997**, *35*, 3441–3449.

(101) Sworen, J. C.; Smith, J. A.; Wagener, K. B.; Baugh, L. S.; Rucker, S. P. *J. Am. Chem. Soc.* **2003**, *125*, 2228–2240.

(102) Love, J. A.; Morgan, J. P.; Trnka, T. M.; Grubbs, R. H. *Angew. Chem. Int. Ed.* **2002**, *41*, 4035–4037.

(103) Wen, S.; Pei, J.; Li, P.; Zhou, Y.; Cheng, W.; Dong, Q.; Li, Z.; Tian, W. *J. Polym. Sci. Pol. Chem.* **2011**, *49*, 2715–2724.

(104) He, Y.; Zhao, G.; Min, J.; Zhang, M.; Li, Y. *Polymer* **2009**, *50*, 5055–5058.

(105) Jestin, I.; Frère, P.; Mercier, N.; Levillain, E.; Stievenard, D.; Roncali, J. *J. Am. Chem. Soc.* **1998**, *120*, 8150–8158.

(106) Jenekhe, S. A.; Lu, L.; Alam, M. M. *Macromolecules* **2001**, *34*, 7315–7324.

(107) Paulsen, B. D.; Frisbie, C. D. *J. Phys. Chem. C* **2012**, *116*, 3132–3141.

(108) Hultgren, V. M.; Mariotti, A. W. A.; Bond, A. M.; Wedd, A. G. *Anal. Chem.* **2002**, *74*, 3151–3156.

(109) Shiddiky, M. J. A.; Torriero, A. A. J.; Zhao, C.; Burgar, I.; Kennedy, G.; Bond, A. M. *J. Am. Chem. Soc.* **2009**, *131*, 7976–7989.

(110) Cardona, C. M.; Li, W.; Kaifer, A. E.; Stockdale, D.; Bazan, G. C. *Adv. Mater.* **2011**, *23*, 2367–2371.

(111) Kim, J.Y.; Qin, Y.; Stevens, D. M.; Ugurlu, O.; Kalihari, V.; Hillmyer, M. A.; Frisbie. C. D. *J. Phys. Chem. C* **2009**, *113*, 10790-10797

(112) Scharber, M. C.; Mühlbacher, D.; Koppe, M.; Denk, P.; Waldauf, C.; Heeger, A. J.; Brabec, C. J. *Adv. Mater.* **2006**, *18*, 1521-4095

(113) Yamamoto, N.; Ito, R.; Geerts, Y.; Nomura, K. *Macromolecules* **2009**, *42*, 5104-5111

(114) de Freitas, J. N.; Pivrikas, A.; Nowacki, B. F.; Akcelrud, L. C.; Sariciftci, N. S.; Nogueira, A. F. *Synth. Met.* **2010**, *160*, 1654-1661

(115) Basescu, N.; Liu, Z. X.; Moses, D.; Heeger, A. J.; Naarmann, H.; Theophilou, N. *Nature* **1987**, *327*, 403-405.

(116) Park, Y. W.; Park, C.; Lee, Y. S.; Yoon, C. O.; Shirakawa, H.; Suezaki, Y.; Akagi, K. *Solid State Commun.* **1988**, *65*, 147-150.

(117) Pasveer, W. F.; Cottaar, J.; Tanase, C.; Coehoorn, R.; Bobbert, P. A.; Blom, P. W. M.; De Leeuw, D. M.; Michels, M. A. J. *Phys. Rev. Lett.* **2005**, *94*, 206601.

(118) Xia, Y.; Cho, J. H.; Lee, J.; Ruden, P. P.; Frisbie, C. D. *Adv. Mater.* **2009**, *21*, 2174-2179.

(119) White, H. S.; Kittlesen, G. P.; Wrighton, M. S. *J. Am. Chem. Soc.* **1984**, *106*, 5375-5377.

(120) Paul, E. W.; Ricco, A. J.; Wrighton, M. S. *J. Phys. Chem.* **1985**, *89*, 1441-1447.

(121) Ofer, D.; Crooks, R. M.; Wrighton, M. S. *J. Am. Chem. Soc.* **1990**, *112*, 7869-7879.

(122) Hanna, R.; Leclerc, M. *Chem. Mater.* **1996**, *8*, 1512-1518.

(123) Ahonen, H. J.; Lukkari, J.; Kankare, J. *Macromolecules* **2000**, *33*, 6787-6793.

(124) Zotti, G.; Zecchin, S.; Schiavon, G.; Vercelli, B.; Berlin, A.; Dalcanale, E.; Groenendaal, L. *Chem. Mater.* **2003**, *15*, 4642-4650.

(125) Panzer, M. J.; Frisbie, C. D. *J. Am. Chem. Soc.* **2007**, *129*, 6599-6607.

(126) Wanekaya, A. K.; Mangesh, A.; Yun, M.; Chen, W.; Myung, N. V.; Mulchandani, A. *J. Phys. Chem. C* **2007**, *111*, 5218-5221.

(127) Pomerantz, Z.; Zaban, A.; Ghosh, S.; Lellouche, J. P.; Garcia-Belmonte, G.; Bisquert, J. *J. Electroanal. Chem.* **2008**, *614*, 49-60.

(128) Xia, Y.; Cho, J. H.; Paulsen, B.; Frisbie, C. D.; Renn, M. J. *Appl. Phys. Lett.* **2009**, *94*, 013304.

(129) Panzer, M. J.; Frisbie, C. D. *J. Am. Chem. Soc.* **2005**, *127*, 6960-6961.

(130) Street, R. A.; Salleo, A.; Chabinyc, M. L. *Phys. Rev. B* **2003**, *68*, 085316.

(131) Lu, W.; Fadeev, A. G.; Qi, B.; Smela, E.; Mattes, B. R.; Ding, J.; Spinks, G. M.; Mazurkiewicz, J.; Zhou, D.; Wallace, G. G.; MacFarlane, D. R.; Forsyth, S. A.; Forsyth, M. *Science* **2002**, *297*, 983.

(132) Kim, J. Y.; Qin, Y.; Stevens, D. M.; Ugurlu, O.; Kalihari, V.; Hillmyer, M. A.; Frisbie, C. D. *J. Phys. Chem. C* **2009**, *113*, 10790-10797.

(133) Jiang, X.; Harima, Y.; Yamashita, K.; Tada, Y.; Ohshita, J.; Kunai, A. *Chem. Phys. Lett.* **2002**, *364*, 616-620.

(134) Bernards, D. A.; Malliaras, G. G. *Adv. Funct. Mater.* **2007**, *17*, 3538-3544.

(135) Newman, C. R.; Frisbie, C. D.; da Silva Filho, D. A.; Brédas, J.; Ewbank, P. C.; Mann, K. R. *Chem. Mater.* **2004**, *16*, 4436-4451.

(136) Lee, J.; Kaake, L. G.; Cho, J. H.; Zhu, X. Y.; Lodge, T. P.; Frisbie, C. D. *J. Phys. Chem. C* **2009**, *113*, 8972-8981.

(137) Conway, B. E.; Birss, V.; Wojtowicz, J. *J. Power Sources* **1997**, *66*, 1-14.

(138) Ogawa, S.; Kimura, Y.; Ishii, H.; Niwano, M. *Jpn. J. Appl. Phys.* **2003**, *42*, 1275.

(139) Liang, Y.; Frisbie, C. D.; Chang, H. C.; Ruden, P. P. *J. Appl. Phys.* **2009**, *105*, 024514.

(140) Tashiro, K.; Ono, K.; Minagawa, Y.; Kobayashi, M.; Kawai, T.; Yoshino, K. *J. Polym. Sci. , Part B: Polym. Phys.* **1991**, *29*, 1223-1233.

(141) Ehrenstein, G. W. In *Polymeric materials: structure, properties, applications;* Hanser/Gardner Publications, Inc.: Cicinnati, **2001**.

(142) Prosa, T. J.; Winokur, M. J.; Moulton, J.; Smith, P.; Heeger, A. J. *Macromolecules* **1992**, *25*, 4364-4372.

(143) Guay, J.; Diaz, A. F.; Bergeron, J. Y.; Leclerc, M. *J. Electroanal. Chem.* **1993**, *361*, 85-91.

(144) Bard, A. J.; Faulkner, L. R. In *Electrochemical Methods: Fundamentals and Applications;* Wiley: New York, **2001**.

(145) Zhao, Y. H.; Abraham, M. H.; Zissimos, A. M. *J. Org. Chem.* **2003**, *68*, 7368-7373.

(146) Ue, M.; Murakami, A.; Nakamura, S. *J. Electrochem. Soc.* **2002**, *149*, A1385-A1388.

(147) Kawai, T.; Nakazono, M.; Yoshino, K. *J. Mater. Chem.* **1992**, *2*, 903-906.

(148) Prosa, T. J.; Winokur, M. J.; Moulton, J.; Smith, P.; Heeger, A. J. *Phys. Rev. B* **1995**, *51*, 159-168.

(149) Tashiro, K.; Kobayashi, M.; Kawai, T.; Yoshino, K. *Polymer* **1997**, *38*, 2867-2879.

(150) Vardeny, Z.; Ehrenfreund, E.; Brafman, O.; Nowak, M.; Schaffer, H.; Heeger, A. J.; Wudl, F. *Phys. Rev. Lett.* **1986**, *56*, 671-674.

(151) Kim, Y. H.; Spiegel, D.; Hotta, S.; Heeger, A. J. *Phys. Rev. B* **1988**, *38*, 5490-5495.

(152) Jiang, X.; Patil, R.; Harima, Y.; Ohshita, J.; Kunai, A. *J. Phys. Chem. B* **2005**, *109*, 221-229.

(153) Yoon, C. O.; Reghu, M.; Moses, D.; Heeger, A. J.; Cao, Y.; Chen, T. A.; Wu, X.; Rieke, R. D. *Synth. Met.* **1995**, *75*, 229-239.

(154) Ukai, S.; Ito, H.; Marumoto, K.; Kuroda, S. *J. Phys. Soc. Jpn.* **2005**, *74*, 3314-3319.

(155) Harima, Y.; Eguchi, T.; Yamashita, K. *Synth. Met.* **1998**, *95*, 69-74.

(156) Harima, Y.; Kunugi, Y.; Yamashita, K.; Shiotani, M. *Chem. Phys. Lett.* **2000**, *317*, 310-314.

(157) Kunugi, Y.; Harima, Y.; Yamashita, K.; Ohta, N.; Ito, S. *J. Mater. Chem.* **2000**, *10*, 2673-2677.

(158) Arkhipov, V. I.; Heremans, P.; Emelianova, E. V.; Adriaenssens, G. J.; Bässler, H. *Appl. Phys. Lett.* **2003**, *82*, 3245.

(159) Martens, H. C. F.; Hulea, I. N.; Romijn, I.; Brom, H. B.; Pasveer, W. F.; Michels, M. A. J. *Phys. Rev. B* **2003**, *67*, 121203.

(160) Arkhipov, V. I.; Emelianova, E. V.; Heremans, P.; Bässler, H. *Phys. Rev. B* **2005**, *72*, 235202.

(161) Shimotani, H.; Diguet, G.; Iwasa, Y. *Appl. Phys. Lett.* **2005**, *86*, 022104.

(162) Coehoorn, R.; Pasveer, W. F.; Bobbert, P. A.; Michels, M. A. J. *Phys. Rev. B* **2005**, *72*, 155206.

(163) Fishchuk, I. I.; Arkhipov, V. I.; Kadashchuk, A.; Heremans, P.; Bässler, H. *Phys. Rev. B* **2007**, *76*, 045210.

(164) Kuroda, S.; Marumoto, K.; Sakanaka, T.; Takeuchi, N.; Shimoi, Y.; Abe, S.; Kokubo, H.; Yamamoto, T. *Chem. Phys. Lett.* **2007**, *435*, 273-277.

(165) Kaake, L. G.; Zhu, X. Y. *J. Phys. Chem. C* **2008**, *112*, 16174-16177.

(166) Hulea, I. N.; Brom, H. B.; Houtepen, A. J.; Vanmaekelbergh, D.; Kelly, J. J.; Meulenkamp, E. A. *Phys. Rev. Lett.* **2004**, *93*, 166601.

(167) Hulea, I. N.; Brom, H. B.; Mukherjee, A. K.; Menon, R. *Phys. Rev. B* **2005**, *72*, 54208.

(168) Trasatti, S. *Pure Appl. Chem.* **1986**, *58*, 955-966.

(169) Sukardi, S. K.; Zhang, J.; Burgar, I.; Horne, M. D.; Hollenkamp, A. F.; MacFarlane, D. R.; Bond, A. M. *Electrochem. Commun.* **2008**, *10*, 250-254.

(170) Stevens, D. M.; Qin, Y.; Hillmyer, M. A.; Frisbie, C. D. *J. Phys. Chem. C* **2009**, *113*, 11408-11415.

(171) Tanase, C.; Meijer, E. J.; Blom, P. W. M.; De Leeuw, D. M. *Phys. Rev. Lett.* **2003**, *91*, 216601.

(172) Torricelli, F.; Kovács-Vajna, Z. M.; Colalongo, L. *Org. Electron.* **2009**, *10*, 1037-1040.

(173) Garcia-Belmonte, G.; Vakarin, E. V.; Bisquert, J.; Badiali, J. P. *Electrochim. Acta* **2010**, *55*, 6123-6127.

(174) Brondijk, J. J.; Maddalena, F.; Asadi, K.; van Leijen, H. J.; Heeney, M.; Blom, P. W. M.; de Leeuw, D. M. *Phys. Status Solidi B* **2011**, *1*, 138-141 .

(175) Kaake, L. G.; Barbara, P. F.; Zhu, X. Y. *J. Phys. Chem. Lett.* **2010**, *1*, 628-635.

(176) Cheung, D. L.; McMahon, D. P.; Troisi, A. *J. Am. Chem. Soc.* **2009**, *131*, 11179-11186.

(177) Ohno, H., Ed.; In *Electrochemical aspects of ionic liquids;* John Wiley & Sons: Hoboken, **2011**.

(178) Zhang, S.; Sun, N.; He, X.; Lu, X.; Zhang, X. *J. Phys. Chem. Ref. Data* **2006**, *35*, 1475.

(179) Ono, S.; Miwa, K.; Seki, S.; Takeya, J. *Appl. Phys. Lett.* **2009**, *94*, 063301.

(180) Xie, W.; Frisbie, C. D. *J. Phys. Chem. C* **2011**, *115*, 14360-14368.

(181) O'Mahony, A. M.; Silvester, D. S.; Aldous, L.; Hardacre, C.; Compton, R. G. *J. Chem. Eng. Data* **2008**, *53*, 2884-2891.

(182) In Search of Tomorrow's Innovations? Ionic Liquids for Electrochemical Applications. http://www.merck-chemicals.com/showBrochure/200905.060.ProNet.pdf (accessed July, 2011).

(183) Noda, A.; Hayamizu, K.; Watanabe, M. *J. Phys. Chem. B* **2001**, *105*, 4603-4610.

(184) Ispas, A.; Peipmann, R.; Bund, A.; Efimov, I. *Electrochim. Acta* **2009**, *54*, 4668-4675.

(185) Campbell, I. H.; Hagler, T. W.; Smith, D. L.; Ferraris, J. P. *Phys. Rev. Lett.* **1996**, *76*, 1900-1903.

(186) Campbell, A. J.; Bradley, D. D. C.; Antoniadis, H. *J. Appl. Phys.* **2001**, *89*, 3343.

(187) Fuchigami, H.; Tsumura, A.; Koezuka, H. *Appl. Phys. Lett.* **1993**, *63*, 1372-1374.

(188) Liu, J.; Shi, Y.; Ma, L.; Yang, Y. *J. Appl. Phys.* **2000**, *88*, 605.

(189) Shaked, S.; Tal, S.; Roichman, Y.; Razin, A.; Xiao, S.; Eichen, Y.; Tessler, N. *Adv. Mater.* **2003**, *15*, 913-916.

(190) Donley, C. L.; Zaumseil, J.; Andreasen, J. W.; Nielsen, M. M.; Sirringhaus, H.; Friend, R. H.; Kim, J. S. *J. Am. Chem. Soc.* **2005**, *127*, 12890-12899.

(191) Günes, S.; Neugebauer, H.; Sariciftci, N. S. *Chem. Rev* **2007**, *107*, 1324–1338.

(192) Thompson, B. C.; Fréchet, J. M. J. *Angew. Chem. Int. Ed.* **2008**, *47*, 58–77.

(193) Heeger, A. J. *Chem. Soc. Rev.* **2010**, *39*, 2354–2371.

(194) Service, R. F. *Science* **2011**, *332*, 293.

(195) Shaheen, S. E.; Brabec, C. J.; Sariciftci, N. S. *Appl. Phys. Lett.* **2001**, *78*, 841–843.

(196) Chen, H. Y.; Hou, J.; Zhang, S.; Liang, Y.; Yang, G.; Yang, Y.; Yu, L.; Wu, Y.; Li, G. *Nat. Phot.* **2009**, *3*, 649–653.

(197) Liang, Y.; Xu, Z.; Xia, J.; Tsai, S. -T. T.; Wu, Y.; Li, G.; Ray, C.; Yu, L. *Adv. Mat.* **2010**, *22*, E135–E138.

(198) Price, S. C.; Stuart, A. C.; Yang, L.; Zhou, H.; You, W. *J. Am. Chem. Soc.* **2011**, *133*, 4625–4631.

(199) Zhou, H.; Yang, L.; Stuart, A. C.; Price, S. C.; Liu, S.; You, W. *Angew. Chem. Int. Ed.* **2011**, *50*, 2995–2998.

(200) Chu, T.-Y.; Lu, J.; Beaupré, I, S.; Zhang, Y.; Pouliot, J. -R.; Wakim, S.; Zhou, J.; Leclerc, M.; Li, Z.; Ding, J.; Tao, Y. *J. Am. Chem. Soc.* **2011**, *133*, 4250–4253.

(201) Veldman, D.; Meskers, S. C. J.; Janssen, R. A. J. *Adv. Funct. Mater.* **2009**, *19*, 1939–1948.

(202) Zen, A.; Pflaum, J.; Hirschmann, S.; Zhuang, W.; Jaiser, F.; Asawapirom, U.; Rabe, J. P.; Scherf, U.; Neher, D. *Adv. Funct. Mater.* **2004**, *14*, 757–764.

(203) Schilinsky, P.; Asawapirom, U.; Scherf, U.; Biele, M.; Brabec, C. J. *Chem. Mater* **2005**, *17*, 2175–2180.

(204) Kline, R. J.; McGehee, M. D.; Kadnikova, E. N.; Liu, J.; Fréchet, J. M. J.; Toney, M. F. *Macromolecules* **2005**, *38*, 3312–3319.

(205) Hiorns, R. C.; de Bettignies, R.; Leroy, J.; Bailly, S.; Firon, M.; Sentein, C.; Khoukh, A.; Preud'homme, H.; Dagron-Lartigau, C. *Adv. Funct. Mater.* **2006**, *16*, 2263–2273.

(206) Chang, J. F.; Clark, J.; Zhao, N.; Sirringhaus, H.; Breiby, D. W.; Andreasen, J. W.; Nielsen, M. M.; Giles, M.; Heeney, M.; McCulloch, I. *Phys. Rev. B* **2006**, *74*, 115318.

(207) Müller, C.; Wang, E.; Andersson, L. M.; Tvingstedt, K.; Zhou, Y.; Andersson, M. R.; Inganäs, O. *Adv. Funct. Mater.* **2010**, *20*, 2124–2131.

(208) Coffin, R. C.; Peet, J.; Rogers, J.; Bazan, G. C. *Nat. Chem.* **2009**, *1*, 657–661.

(209) Huang, J.-H.; Chen, F.-C.; Chen, C.-L.; Huang, A. T.; Hsiao, Y.-S.; Teng, C.-M.; Yen, F.-W.; Chen, P.; Chu, C.-W. *Org. Electron.* **2011**, *12*, 1755–1762.

(210) Baughman, T. W.; Wagener, K. B. *Adv. Polym. Sci.* **2005**, *176*, 1–42.

(211) Tao, D.; Wagener, K. B. *Macromolecules* **1994**, *27*, 1281–1283.

(212) Fox, H. H.; Schrock, R. R.; O'Dell, R. *Organometallics* **1994**, *13*, 635–639.

(213) Miao, Y. J.; Bazan, G. C. *Macromolecules* **1997**, *30*, 7414–7418.

(214) Tsuie, B.; Wagener, K. B. *Polym. Prepr.* **1999**, *40*, 709.

(215) Nomura, K.; Morimoto, H.; Imanishi, Y.; Ramhani, Z.; Geerts, Y. *J. Polym. Sci. Pol. Chem.* **2001**, *39*, 2463–2470.

(216) Delgado, P. A.; Liu, D. Y.; Kean, Z.; Wagener, K. B. *Macromolecules*, **2011**, *44*, 9529–9532.

(217) Smith, A. P.; Smith, R. R.; Taylor, B. E.; Durstock, M. F. *Chem. Mater.* **2004**, *16*, 4687–4692.

(218) Huong Nguyen, L.; Guenes, S.; Neugebauer, H.; Serdar Sariciftci, N.; Banishoeib, F.; Henckens, A.; Cleij, T.; Lutsen, L.; Vanderzande, D. *Sol. Ener. Mater. Sol. Cells* **2006**, *90*, 2815–2828.

(219) Girotto, C.; Cheyns, D.; Aernouts, T.; Banishoeib, F.; Lutsen, L.; Cleij, T. J.; Vanderzande, D.; Genoe, J.; Poortmans, J.; Heremans, P. *Org. Elec.* **2008**, *9*, 740–746.

(220) Kim, J. Y.; Qin, Y.; Stevens, D. M.; Ugurlu, O.; Kalihari, V.; Hillmyer, M. A.; Frisbie, C. D. *J. Phys. Chem. C* **2009**, *113*, 10790–10797.

(221) Kossmehl, V. G.; Härtel, M.; Manecke, G. *Makromol. Chem.* **1970**, *131*, 15–54.

(222) Yamada, S.; Tokito, S.; Tsutsui, T.; Saito, S. *J. Chem. Soc., Chem. Commun.* **1987**, 1448–1449.

(223) Jen, K. -Y.; Maxfield, M.; Shacklette, L. W.; Elsenbaumer, R. L. *J. Chem. Soc., Chem. Commun.* **1987**, 309–311.

(224) Banishoeib, F.; Henckens, A.; Fourier, S.; Vanhooyland, G.; Breselge, M.; Manca, J.; Cleij, T. J.; Lutsen, L.; Vanderzande, D.; Nguyen, L. H.; Neugebauer, H.; Sariciftci, N. S. *Thin Solid Films* **2008**, *516*, 3978–3988.

(225) Cornelissen, J.; Peeters, E.; Janssen, R. A. J.; Meijer, E. W. *Acta Polym.* **1998**, *49*, 471–476.

(226) Lim, J. -; Suzuki, M.; Saegusa, T. *Polym. Bull.* **1993**, *31*, 651–658.

(227) Loewe, R. S.; McCullough, R. D. *Chem. Mater.* **2000**, *12*, 3214–3221.

(228) Zhou, E.; Yang, Y.; Huo, L.; Zou, Y.; Yang, C.; Li, Y. *Macromolecules* **2007**, *40*, 1831–1837.

(229) Huo, L.; Chen, T. L.; Zhou, Y.; Hou, J.; Chen, H. Y.; Yang, Y.; Li, Y. *Macromolecules* **2009**, *42*, 4377–4380.

(230) Qin, Y.; Hillmyer, M. A. *Macromolecules* **2009**, *42*, 6429–6432.

(231) Love, J. A.; Morgan, J. P.; Trnka, T. M.; Grubbs, R. H. *Angew. Chem. Int. Ed.* **2002**, *41*, 4035–4037.

(232) Wagener, K. B.; Boncella, J. M.; Nel, J. G. *Macromolecules* **1991**, *24*, 2649–2657.

(233) Lehman, S. E.; Wagener, K. B. *Macromolecules* **2002**, *35*, 48–53.

(234) Zhang, C.; Sun, J.; Li, R.; Sun, S. -S.; Lafalce, E.; Jiang, X. *Macromolecules* **2011**, *44*, 6389–6396.

(235) Liu, J.; Loewe, R. S.; McCullough, R. D. *Macromolecules* **1999**, *32*, 5777–5785.

(236) Holdcroft, S. *J. Polym. Sci. Pol. Phys.* **1991**, *29*, 1585–1588.

(237) Biagini, S. C. G.; Davies, R. G.; Gibson, V. C.; Giles, M. R.; Marshall, E. L.; North, M. *Polymer* **2001**, *42*, 6669-6671.

(238) Chang, J.-F.; Clark, J.; Zhao, N.; Sirringhaus, H.; Breiby, D. W.; Andreasen, J. W.; Nielsen, M. M.; Giles, M.; Heeney, M.; McCulloch, I. *Phys. Rev. B* **2006**, *74*, 115318.

(239) Clark, J.; Silva, C.; Friend, R. H.; Spano, F. C. *Phys. Rev. Lett.* **2007**, *98*, 206406.

(240) Inganas, O.; Salaneck, W. R.; Osterholm, J. E.; Laakso, J. *Synth. Met.* **1988**, *22*, 395–406.

(241) Salaneck, W. R.; Inganäs, O.; Themans, B.; Nilsson, J. O.; Sjögren, B.; Österholm, J. E.; Brédas, J. L.; Svensson, S. *J. Chem. Phys.* **1988**, *89*, 4613–4619.

(242) Métivaud, V.; Lefèvre, A.; Ventolà, L.; Négrier, P.; Moreno, E.; Calvet, T.; Mondieig, D.; Cuevas-Diarte, M. A. *Chem. Mater.* **2005**, *17*, 3302–3310.

(243) Park, K. C.; Levon, K. *Macromolecules* **1997**, *30*, 3175–3183.

(244) Hamilton, R.; Bailey, C.; Duffy, W.; Heeney, M.; Shkunov, M.; Sparrowe, D.; Tierney, S.; McCulloch, I.; Kline, R. J.; DeLongchamp, D. M.; Chabinyc, M. *Proc. SPIE* **2006**, *6336*, 633611.

(245) Kline, R. J.; McGehee, M. D.; Kadnikova, E. N.; Liu, J.; Fréchet, J. M. J. *Adv. Mater.* **2003**, *15*, 1519–1522.

(246) Goh, C.; Kline, R. J.; McGehee, M. D.; Kadnikova, E. N.; Fréchet, J. M. J. *Appl. Phys. Lett.* **2005**, *86*, 122110

(247) Diliën, H.; Palmaerts, A.; Lenes, M.; de Boer, B.; Blom, P.; Cleij, T. J.; Lutsen, L., Vanderzande, D. *Macromolecules* **2010**, *43*, 10231–10240.

(248) Kim, Y.; Cook, S.; Choulis, S. A.; Nelson, J.; Durrant, J. R.; Bradley, D. D. C. *Chem. Mater.* **2004**, *16*, 4812–4818.

(249) Kim, Y.; Cook, S.; Tuladhar, S. M.; Choulis, S. A.; Nelson, J.; Durrant, J. R.; Bradley, D. D. C.; Giles, M. McCulloch, I.; Ha, C.-S.; Ree, M. *Nat. Mater.* **2006**, *5*, 197–203.

(250) Kim, J. Y.; Frisbie, C. D. *J. Phys. Chem. C* **2008**, *112*, 17726–17736.

(251) Müller, C.; Ferenczi, T. A. M.; Campoy-Quiles, M.; Frost, J. M.; Bradley, D. D. C.; Smith, P.; Stingelin-Stutzmann, N.; Nelson, J. *Adv. Mater.* **2008**, *20*, 3510–3515.

(252) Zhao, J.; Swinnen, A.; Van Assche, G.; Manca, J.; Vanderzande, D.; Mele, B. V. *J. Phys. Chem. B* **2009**, *113*, 1587–1591.

(253) Hopkinson, P. E.; Staniec, P. A.; Pearson, A. J.; Dunbar, A. D. F.; Wang, T.; Ryan, A. J.; Jones, R. A. L.; Lidzey, D. G.; Donald, A. M. *Macromolecules* **2011**, *44*, 2908–2917.

(254) Miller, N. C.; Gysel, R.; Miller, C. E.; Verploegen, E.; Beiley, Z.; Heeney, M.; McCulloch, I.; Bao, Z.; Toney, M. F.; McGehee, M. D. *J. Polym. Sci. Pol. Phys.* **2011**, *49*, 499–503.

(255) Müller, C.; Bergqvist, J.; Vandewal, K.; Tvingstedt, K.; Anselmo, A. S.; Magnusson, R.; Alonso, M. I.; Moons, E.; Arwin, H.; Campoy-Quiles, M.; Inganäs, O. *J. Mater. Chem.* **2011**, *21*, 10676–10684.

(256) Zhao, J.; Bertho, S.; Vandenbergh, J.; Van Assche, G.; Manca, J.; Vanderzande, D.; Yin, X.; Shi, J.; Cleij, T.; Lutsen, L.; Van Mele, B. *Phys. Chem. Chem. Phys.* **2011**, *13*, 12285–12292.

(257) Kim, J. Y.; Qin, Y.; Stevens, D. M.; Kalihari, V.; Hillmyer, M. A.; Frisbie, C. D. *J. Phys. Chem. C* **2009**, *113*, 21928–21936.

(258) Ma, W.; Yang, C.; Heeger, A. J. *Adv. Mater.* **2007**, *19*, 1387–1390.

(259) *Electrochemical aspects of ionic liquids;* Ohno, H. ed.; Wiley: Hoboken, 2005.

(260) Panzer, M. J.; Frisbie, C. D. *Adv. Funct. Mater.* **2006**, *16*, 1051-1056.

(261) Xie, W.; Frisbie, C. D. *manuscript in preparation.*

(262) Puntambekar, K. P.; Pesavento, P. V.; Frisbie, C. D. *Appl. Phys. Lett.* **2003**, *83*, 5539.

(263) Pesavento, P. V.; Chesterfield, R. J.; Newman, C. R.; Frisbie, C. D. *J. Appl. Phys.* **2004** *96*, 7312.

(264) Braga, D.; Ha, M; Xie, W.; Frisbie, C. D. *Appl. Phys. Lett.* **2010** *97*, 193311.

(265) Dhoot, A. S.; Wang, G. M.; Moses, D.; Heeger. A. J. *Phys. Rev. Lett.* **2006,** *96*, 246403.

(266) Prigodin, V. N.; Epstein, A. J. *Phys. Rev. Lett.* **2007**, *98*, 259703.

(267) Yuen, J. D.; Menon, R.; Coates, N. E.; Namdas, E. B.; Cho, S.; Hannahs, S. T.; Moses, D.; Heeger, A. J. *Nature Mater.* **2009**, *8*, 572-575.

(268) Kronemeijer, A. J.; Huisman, E. H.; Katsouras, I.; van Hal, P. A.; Geuns, T. C. T.; Blom, P. W. M.; van der Molen, S. J.; de Leeuw, D. M. *Phys. Rev. Lett.* **2010**, *105*, 156604

(269) Worne, J. H., Anthony, J. E.; Natelson, D. *Appl. Phys. Lett.* **2010**, *96*, 053308.

(270) Gregg, B. A. *J. Phys. Chem. C* **2009**, *113*, 5899–5901.

(271) Wang, S.; Ha, M.; Manno, M.; Frisbie, C. D.; Leighton, C. *Nature Comm.* **2012**, *in press.*

(272) Blom, P. W. M.; de Jong, M. J. M.; van Munster,M. G. *Phys. Rev. B* **1997**, *55*, 656-659

(273) Chen, S. G.; Stradins, P.; Gregg, B. A. *J. Phys. Chem. B* **2005**, *109* 13451-13460

(274) Paulsen, B. D.; Frisbie, C. D. *J. Phys. Chem. C* **2012**, *116*, 3132–3141.

(275) Speros, J. C.; Paulsen, B. D.; White, S. P.; Wu, Y.; Jackson, E. A.; Slowinski, B. S.; Frisbie, C. D.; Hillmyer, M. A. *Macromolecules* **2012**, *45*, 2190–2199.

(276) Speros, J. C.; Paulsen, B. D.; Slowinski, B. S.; Frisbie, C. D.; Hillmyer, M. A. *ACS Macro Lett.* **2012**, *1*, 986–990.

(277) Svensson, M.; Zhang, F.; Veenstra, S. C.; Verhees, W. J. H.; Hummelen, J. C.; Kroon, J. M.; Inganäs, O.; Andersson, M. R. Adv. Mater. **2003**, *15*, 988-991.

(278) Zhou, Q.; Hou, Q.; Zheng, L.; Deng, X.; Yu, G.; Cao, Y. *Appl. Phys. Lett.* **2004**, *84*, 1653

(279) Müller1, C.; Wang, E.; Andersson, L. M.; Tvingstedt, K.; Zhou, Y.; Andersson, M. R.; Inganäs, O. *Adv. Funct. Mater.* **20101**, *20*, 2124-2131

(280) Ko, S.; Mondal, R.; Risko, C.; Lee, J. K.; Hong, S.; McGehee, M. D.; Brédas, J. L.; Bao, Z. *Macromolecules* **2010**, *43*, 6685-6698

(281) Ma, W.; Yang, C.; Gong, X.; Lee, K.; Heeger, A. J. *Adv. Funct. Mater.* **2005**, *15*,1617-1622.

(282) Li, G.; Shrotriya, V.; Huang, J.; Yao, Y.; Moriarty, T.; Emery, K.; Yang, Y. Nature Mater. **2005**, *4*, 864-868.

(283) Kim, J. Y.; Qin, Y.; Stevens, D. M.; Ugurlu, O.; Kalihari, V.; Hillmyer, M. A.; Frisbie C. D.; *J. Phys. Chem. C* **2009**, *113*, 10790-10797

(284) Park, S. H.; Roy, A.; Beaupré, S.; Cho, S.; Coates, N.; Moon, J. S.; Moses, D.; Leclerc, M.; Lee, K.; Heeger, A. J. *Nature Photon.* **2009**, *3*, 297-302.

(285) Olejnik, E.; Pandit, B.; Basel, T.; Lafalce, E. ; Sheng, C. X.; Zhang, C. ; Jiang, X.; Vardeny, Z. V. *Phys. Rev. B* **2012**, *85*, 235201.

(286) Fuchigami, H.; Tsumura, A.; Koezuka, H. *Appl. Phys. Lett.* **1993**, *6*3, 1372-1374.

(287) Kim, Y.; Cook, S.; Tuladhar, S. M.; Choulis, S. A.; Nelson, J.; Durrant, J. R.; Bradley, D. D. C.; Giles, M.; McCulloch, I.; Ha, C. S.; Ree, M. *Nature Mater.* **2006**, *5*, 197-203.

(288) Zhang, C.; Sun, J.; Li, R.; Sun, S. S.; Lafalce, E.; Jiang X. *Macromolecules* **2011,** *44*, 6389-6396.

(289) Li, Y. *Accounts of Chemical Research* **2012**, *45*, 723-733.

(290) Facchetti, A. *Chemistry of Materials* **2011**, *23*, 733-758.

(291) Riedel, I.; Parisi, J.; Dyakonov, V.; Lutsen, L.; Vanderzande, D.; Hummelen. J. C.; *Adv. Funct. Mater.* **2004**, *14*, 38-44.

(292) Gommans, H. H. P.; Kemerink, M.; Kramer, J. M.; Janssen, R. A. J. *Appl. Phys. Lett.* **2005**, *87*, 122104.

(293) Street, R. A.; Schoendorf, M.; Roy, A.; Lee, J. H. *Phys. Rev. B* **2010**, *81*, 205307.

(294) Liang, Z.; Nardes, A. M.; van de Lagemaat, J.; Gregg, B. A. *Adv. Funct. Mater.* **2012**, *22*, 1087-1091.

(295) Cowan, S. R.; Roy, A.; Heeger, A. J. *Phys. Rev. B* **2010**, *82*, 245207.

(296) Katz, E. A.; Faiman, D.; Tuladhar, S. M.; Kroon, J. M.; Wienk, M. M.; Fromherz, T.; Padinger, F.; Brabec, C. J.; Sariciftci, N. S. *J. Appl. Phys.* **2001**, *90*, 5343.

(297) Chirvase, D.; Chiguvare, Z.; Knipper, M.; Parisi, J.; Dyakonov, V.; Hummelen, J. C. *J. Appl. Phys.* **2003**, *93*, 3376.

(298) Kippelen, B.; Brédas, J. L. *Energy & Environ. Sci.* **2009**, *2*, 251-261.

(299) Perez, M. D.; Borek, C.; Forrest, S. R.; Thompson, M. E. *Journal of the American Chemical Society* **2009**, *131*, 9281-9286.

(300) Stevens, D. M.; Speros, J. C.; Hillmyer, M. A.; Frisbie, C. D. *The Journal of Physical Chemistry C* **2011**, *115*, 20806-20816.

(301) Dou, L.; You, J.; Yang, J.; Chen, C. C.; He, Y.; Murase, S.; Moriarty, T.; Emery, K.; Li, G.; and Yang, Y. *Nature Photo.* **2012**, *6*, 180-185.

(302) Chen, L. M.; Hong, Z.; Li, G.; Yang, Y. *Adv. Mater.* **2009**, *21*, 1434-1449.

(303) Troshin, P. A.; Hoppe, H.; Renz, J.; Egginger, M.; Mayorova, J. Y.; Goryachev, A. E.; Peregudov, A. S.; Lyubovskaya1, R. N.; Gobsch, G.; Sariciftci, N. S.; Razumov, V. F *Adv. Funct. Mater.* **2009**, *19*, 779-788.

(304) Ahlswede, E.; Hanisch, J.; Powalla, M. *Appl. Phys. Lett.* **2007**, *90*, 163504-163504.

(305) Hoven, C. V.; Dang, X. D.; Coffin, R. C.; Peet, J.; Nguyen, T. Q.; Bazan, G. C. *Adv. Mater.* **2010**, *22*, E63-E66.

(306) Montgomery, D. C. *Design and analysis of experiments;* Wiley, 2008.

(307) Petzold, S.; Wang, C.; Khazaal, A.; Osswald. T.; *Plastics Eng.* **2010**, 26-32.

(308) Pantelidou, A. E. *Optimizing the Efficiency of Organic Bulk Heterojunction Photovoltaics using the Design of Experiments Methodology.* Master's Dissertation, Tufts University, 2011.

# *Appendix*

## *A. Copy Write Permission*

### American Chemical Society's Policy on Theses and Dissertations

If your university requires you to obtain permission, you must use the RightsLink permission system. See RightsLink instructions at http://pubs.acs.org/page/copyright/permissions.html.

This is regarding request for permission to include your paper(s) or portions of text from your paper(s) in your thesis. Permission is now automatically granted; please pay special attention to the implications paragraph below. The Copyright Subcommittee of the Joint Board/Council Committees on Publications approved the following:

Copyright permission for published and submitted material from theses and dissertations

ACS extends blanket permission to students to include in their theses and dissertations their own articles, or portions thereof, that have been published in ACS journals or submitted to ACS journals for publication, provided that the ACS copyright credit line is noted on the appropriate page(s).

Publishing implications of electronic publication of theses and dissertation material

Students and their mentors should be aware that posting of theses and dissertation material on the Web prior to submission of material from that thesis or dissertation to an ACS journal may affect publication in that journal. Whether Web posting is considered prior publication may be evaluated on a case-by-case basis by the journal's editor. If an ACS journal editor considers Web posting to be "prior publication", the paper will not be accepted for publication in that journal. If you intend to submit your unpublished paper to ACS for publication, check with the appropriate editor prior to posting your manuscript electronically.

Reuse/Republication of the Entire Work in Theses or Collections: Authors may reuse all or part of the Submitted, Accepted or Published Work in a thesis or dissertation that the author writes and is required to submit to satisfy the criteria of degree-granting institutions. Such reuse is permitted subject to the ACS' "Ethical Guidelines to Publication of Chemical Research" (http://pubs.acs.org/page/policy/ethics/index.html); the author should secure written confirmation (via letter or email) from the respective ACS journal editor(s) to avoid potential conflicts with journal prior publication*/embargo policies. Appropriate citation of the Published Work must be made. If the thesis or dissertation to be published is in electronic format, a direct link to the Published Work

must also be included using the ACS Articles on Request author-directed link − see http://pubs.acs.org/page/policy/articlesonrequest/index.html

* Prior publication policies of ACS journals are posted on the ACS website at http://pubs.acs.org/page/policy/prior/index.html

Title:
Band Gap and HOMO Level Control in Poly(thienylene vinylene)s Prepared by ADMET Polymerization

Author:
Joshua C. Speros, Bryan D. Paulsen, Bradley S. Slowinski, C. Daniel Frisbie, and Marc A. Hillmyer

Publication:
ACS Macro Letters

Publisher:
American Chemical Society

Date:
Aug 1, 2012



Title:
Dependence of Conductivity on Charge Density and Electrochemical Potential in Polymer Semiconductors Gated with Ionic Liquids

Author:
Bryan D. Paulsen and C. Daniel Frisbie

Publication:
The Journal of Physical Chemistry C

Publisher:
American Chemical Society

Date:
Feb 1, 2012



Title:

An ADMET Route to Low-Band-Gap Poly(3-hexadecylthienylene vinylene): A Systematic Study of Molecular Weight on Photovoltaic Performance

Author:
Joshua C. Speros, Bryan D. Paulsen, Scott P. White, Yanfei Wu, Elizabeth A. Jackson, Bradley S. Slowinski, C. Daniel Frisbie, and Marc A. Hillmyer

Publication:
Macromolecules

Publisher:
American Chemical Society

Date:
Mar 1, 2012